

AD-A120 613

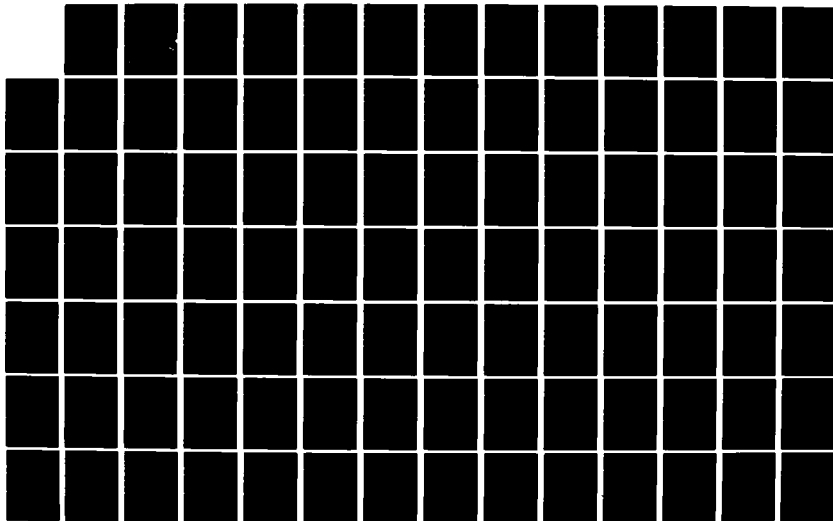
DEVELOPING TURBULENT FLOW IN A 180 DEGREE BEND AND  
DOWNSTREAM TANGENT OF.. (U) CALIFORNIA UNIV BERKELEY  
LAWRENCE BERKELEY LAB J A HUMPHREY ET AL. SEP 82  
LBL-14844NN00014-80-C-0031

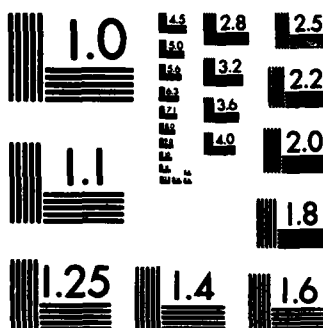
1/2

UNCLASSIFIED

F/G 20/4

NL

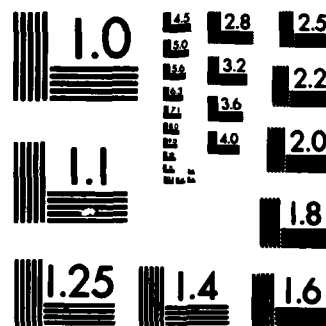




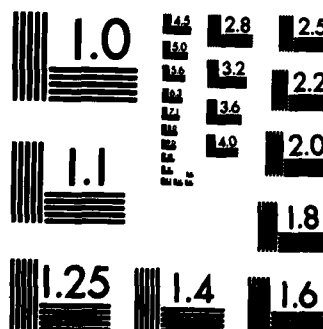
MICROCOPY RESOLUTION TEST CHART  
NATIONAL BUREAU OF STANDARDS-1963-A



MICROCOPY RESOLUTION TEST CHART  
NATIONAL BUREAU OF STANDARDS-1963-A



MICROCOPY RESOLUTION TEST CHART  
NATIONAL BUREAU OF STANDARDS-1963-A



MICROCOPY RESOLUTION TEST CHART  
NATIONAL BUREAU OF STANDARDS-1963-A



MICROCOPY RESOLUTION TEST CHART  
NATIONAL BUREAU OF STANDARDS-1963-A

ADA 120613

DTIC FILE COPY

DEVELOPING TURBULENT FLOW IN A 180° BEND  
AND DOWNSTREAM TANGENT OF SQUARE CROSS-SECTIONS

by

J.A.C. Humphrey, S.M. Chang and A. Modavi

(LBL Report No. 14844)

Department of Mechanical Engineering  
University of California  
Berkeley, California 94720

September 1982

Third Annual Technical Report  
corresponding to period  
October 1, 1981 - September 30, 1982

for Project entitled

TURBULENT FLOW AND HEAT TRANSFER IN PASSAGE AROUND  
180° BEND - AN EXPERIMENTAL AND NUMERICAL STUDY


Prepared for  
M.K. Ellingsworth, Program Monitor  
The Office of Naval Research  
Arlington, Virginia 22217

Under Contract No. N00014-80-C-0031, work unit NR 097-440

Approved for public release; distribution unlimited  
reproduction in whole or in part permitted  
for any purpose of the United States government

82 10 21 077

DTIC  
ELECTED  
OCT 21 1982

REPORT DOCUMENTATION PAGE		READ INSTRUCTIONS BEFORE COMPLETING FORM												
1. REPORT NUMBER N00014-80-C-0031A	2. GOVT ACCESSION NO. AD-A120 613	3. RECIPIENT'S CATALOG NUMBER												
4. TITLE (and Subtitle) Developing Turbulent Flow in a 180° Bend and Downstream Tangent of Square Cross-Sections		5. TYPE OF REPORT & PERIOD COVERED Yearly (Detailed) Oct. 1, 1981-Sept. 30, 1982												
		6. PERFORMING ORG. REPORT NUMBER												
7. AUTHOR(s) J.A.C. Humphrey <sup>1</sup> , S.M. Chang <sup>2</sup> and A. Modavi <sup>2</sup> 1. Principal Investigator 2. Research Assistant		8. CONTRACT OR GRANT NUMBER(s) N00014-80-C-0031												
9. PERFORMING ORGANIZATION NAME AND ADDRESS Department of Mechanical Engineering University of California Berkeley, California 94720		10. PROGRAM ELEMENT, PROJECT, TASK AREA & WORK UNIT NUMBERS												
11. CONTROLLING OFFICE NAME AND ADDRESS Office of Naval Research 800 N. Quincy Street Arlington, VA. 22217		12. REPORT DATE September 1982												
		13. NUMBER OF PAGES 151												
14. MONITORING AGENCY NAME & ADDRESS (if different from Controlling Office)		15. SECURITY CLASS. (of this report) Unclassified												
		15a. DECLASSIFICATION, DOWNGRADING SCHEDULE												
16. DISTRIBUTION STATEMENT (of this Report): Approved for Public Release; Distribution Unlimited														
<table border="1"> <tr> <td colspan="2">Accession For</td> </tr> <tr> <td>NTIS GRA&amp;I</td> <td><input checked="" type="checkbox"/></td> </tr> <tr> <td>DTIC TAB</td> <td><input type="checkbox"/></td> </tr> <tr> <td>Unannounced</td> <td><input type="checkbox"/></td> </tr> <tr> <td colspan="2">Justification</td> </tr> </table>			Accession For		NTIS GRA&I	<input checked="" type="checkbox"/>	DTIC TAB	<input type="checkbox"/>	Unannounced	<input type="checkbox"/>	Justification			
Accession For														
NTIS GRA&I	<input checked="" type="checkbox"/>													
DTIC TAB	<input type="checkbox"/>													
Unannounced	<input type="checkbox"/>													
Justification														
17. DISTRIBUTION STATEMENT (of the abstract entered in Block 20, if different from Report): Same as Block 16														
<table border="1"> <tr> <td colspan="2">By</td> </tr> <tr> <td colspan="2">Distribution/</td> </tr> <tr> <td colspan="2">Availability Codes</td> </tr> <tr> <td colspan="2">Avail and/or</td> </tr> <tr> <td>Dist</td> <td>Special</td> </tr> <tr> <td>A</td> <td></td> </tr> </table>			By		Distribution/		Availability Codes		Avail and/or		Dist	Special	A	
By														
Distribution/														
Availability Codes														
Avail and/or														
Dist	Special													
A														
18. SUPPLEMENTARY NOTES														
<div style="text-align: center;">  </div>														
19. KEY WORDS (Continue on reverse side if necessary and identify by block number) Turbulence Modeling, Curved Duct, Bend, Laser-Doppler Velocimetry, Numerical Computation, Numerical Diffusion, Secondary Motion  k - epsilon  150 DEG														
20. ABSTRACT (Continue on reverse side if necessary and identify by block number) A detailed account is given of the experimental and numerical modeling activities for the research period, relating to turbulent flow in a 180° curved duct. The measurements show variations in the flow field which, while understood, are not predictable by a k-epsilon model of turbulence. Numerical diffusion and exaggerated physical diffusion in the turbulence model are believed to be the major causes for the discrepancies observed. The new experimental data offered here should be of value for extending the theoretical base for the improved understanding and modeling of 3-D turbulent flows. Recommendations are made for continuing work.														

DEVELOPING TURBULENT FLOW IN A 180° BEND  
AND DOWNSTREAM TANGENT OF SQUARE CROSS-SECTIONS

by

J.A.C. Humphrey, S.M. Chang and A. Modavi

Department of Mechanical Engineering  
University of California, Berkeley  
Berkeley, California 94720

LBL Report No. 14844

September 1982

## ABSTRACT

Flows in ducts with curvature manifest secondary motions driven by lateral curvature of the main flow. In addition, cross-stream motions can arise in non-circular ducts due to gradients of the Reynolds stresses in the plane perpendicular to the main flow. Observations from this study suggest that in a strongly curved  $180^\circ$  bend of square cross-section, the latter mechanism contributes negligibly to the secondary motion. New, non-intrusive measurements of the mean flow in this configuration are in qualitative agreement with earlier results from inviscid flow analysis. Also, measurements of the turbulent stresses display previously undocumented anisotropic characteristics arising from shearing motions induced in the core of the flow.

Laminar and turbulent flow predictions have been made for the experimental configuration. Unlike earlier work, turbulence model deficiencies are more clearly revealed by the higher order accuracy of the finite differencing scheme used and the implementation of a partially-parabolic calculation algorithm. It is found that, with the problem of numerical diffusion relieved, false physical diffusion in the turbulence model is the main cause for the differences observed between measurements and computations. Solutions of the turbulent flow field in the bend and downstream tangent show an insensitivity to variations in the specification of the inlet plane boundary condition for streamwise vorticity. An explanation for this finding is given in terms of an approximate equation for the evolution of streamwise vorticity.

Knowledge of the type of flow investigated here is essential for testing and advancing new turbulence modeling concepts. As examples, in addition to the main secondary flow, laminar flow predictions reveal a Dean-type vortex structure at the concave wall in the bend; a second vortex on the convex wall;

and a third corner vortex on the convex wall-side of the bend. The third vortex is associated with the phenomenon of wall stall in cascade flows. In the downstream tangent, turbulent flow measurements show drastic reductions of the cross-stream motion taking place in less than 5 hydraulic diameters, but the main flow recovers only slowly from the effects of the bend. Emphasis should be placed on the development of higher order model closures for predicting the type of highly anisotropic three-dimensional turbulent flow examined here.

Abstract	i
Contents	iii
Nomenclature	iv
1. Introduction	1
1.1 Secondary Motions in Ducted Flows	1
1.2 The Problem of Interest	5
1.3 Objective of this Study	5
1.4 Outline of the Paper	6
2. The Experiment	7
2.1 Flow System and Instrumentation	7
2.2 Experimental Methodology and Measurement Error	10
3. The Numerical Procedure	15
3.1 Governing Equations and Boundary Conditions	15
3.2 Finite Differencing and Numerical Algorithm	16
3.3 Testing	17
4. Results and Discussion	20
4.1 Turbulent Flow Measurements and Calculations	20
4.2 Laminar Flow Calculations	33
5. Conclusions and Recommendations	38
Acknowledgements	43
References	44
Tables	
Figures	
Appendix I: QUICK Scheme Formulation for Transport Variables	
Appendix II: Full Scale Plots of Measured Turbulent Flow Data	
Appendix III: Plots of Laminar Flow Calculations	



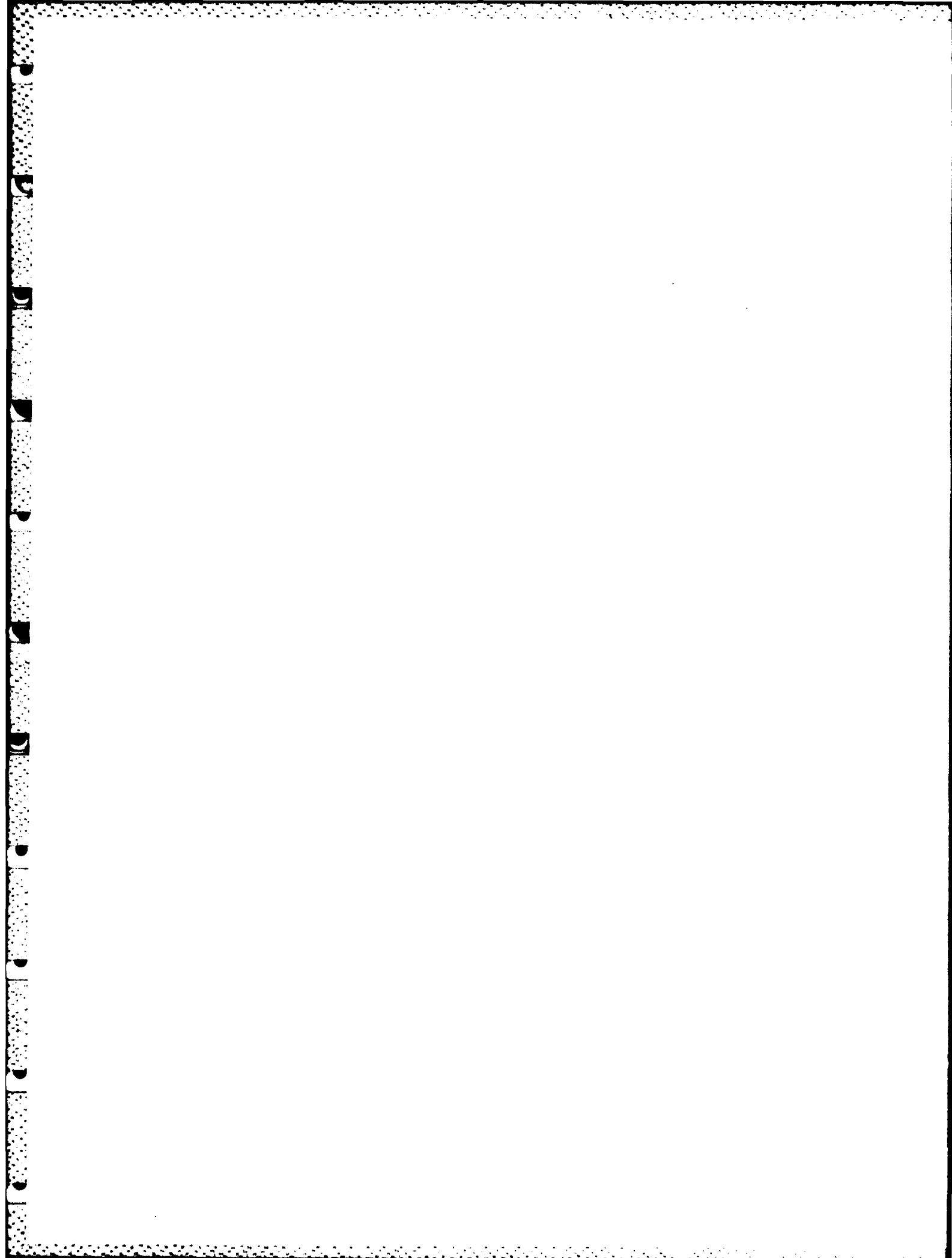
## NOMENCLATURE

$C_\mu$	constant in equation for $\mu_t$
$C_p$	$(\equiv \frac{\Delta P}{\rho U_B^2})$ pressure coefficient
$De$	$(\equiv Re \sqrt{\frac{D_H/2}{R_c}})$ Dean number
$D_H$	hydraulic diameter
$k$	$(\equiv \frac{1}{2} \overline{u_i^2})$ kinetic energy of turbulence
$P$	mean pressure
$R$	local radius of curvature of a streamline
$R_c$	$(\equiv \frac{r_i + r_o}{2})$ mean radius of curvature of the bend
$Re$	$(\equiv \frac{D_H U_B}{\nu})$ Reynolds number
$r$	transverse or radial coordinate in bend
$r_i$	inner-radius of bend (convex wall)
$r_o$	outer-radius of bend (concave wall)
$s$	streamline coordinate direction
$U_B$	bulk average velocity
$U_r$	transverse or radial component of mean velocity (in straight ducts and bend)
$U_\theta$	streamwise or longitudinal component of mean velocity (in straight ducts and bend)
$\tilde{u}_r$	$(\equiv \sqrt{\overline{u_r^2}})$ r.m.s. of transverse normal stress (in straight ducts and bend)
$\tilde{u}_\theta$	$(\equiv \sqrt{\overline{u_\theta^2}})$ r.m.s. of streamwise normal stress (in straight ducts and bend)
$\overline{u_\theta u_r}$	$\theta, r$ component of Reynolds stress (in straight ducts and bend)

$V$	magnitude of vector velocity at a point
$x$	streamwise or longitudinal coordinate in straight ducts
$x_H$	$(\equiv x/D_H)$ normalized streamwise coordinate in straight ducts
$y$	$(\equiv r - r_i)$ transverse coordinate in straight ducts and bends
$z$	spanwise coordinate in straight ducts and bends

#### Greek symbols

$\alpha$	angle by which a Bernouilli surface is turned
$\epsilon$	isotropic rate of dissipation of $k$
$\eta$	$(\equiv (r - r_i)/(r_o - r_i))$ normalized transverse or radial coordinate
$\theta$	streamwise or longitudinal coordinate in bend
$\kappa$	Von Karman constant
$\nu$	laminar kinematic viscosity
$\nu_t$	turbulent kinematic viscosity
$\xi_r$	vorticity component in radial direction
$\xi$	vorticity component in longitudinal direction
$\rho$	density
$\phi$	angle between the normal acceleration and normal to a Bernouilli surface
$\Omega_0$	initial uniform vorticity in the plane of the bend



## 1. INTRODUCTION

### 1.1 Secondary Motions in Ducted Flows

Flows in ducts with curvature experience pressure induced cross-stream (secondary) motions of academic interest, and having very significant consequences in many industrial applications involving heat and mass transfer. Further to the motions induced by the transverse pressure gradient, gradients of the Reynolds stresses in the cross-stream plane can also produce a secondary flow. The latter flow is sometimes referred to as secondary flow of the "second kind" and, unlike the pressure-gradient driven flow of the "first kind", does not arise in the laminar flow regime. Typically, motions of the first kind are 10-30 times faster than motions of the second kind, suggesting that the cross-stream flow in a curved duct is principally dominated by mean pressure forces. The theory of secondary flow induced by lateral curvature of the main flow and by gradients of the Reynolds stresses respectively has been reviewed recently by Johnston [1].

Experimental measurements of developing mean flow and turbulence characteristics in a 90° bend of square cross-section have been reported by Humphrey, Whitelaw and Yee [2] and by Taylor, Whitelaw and Yianneskis [3]. These studies were performed using non-disturbing laser-Doppler velocimetry techniques. In [3] thin boundary layers were purposefully induced at the bend inlet plane, whereas in [2] essentially fully developed straight duct flow was presented as the inlet condition. The most marked differences between the results of these two studies were, in general, the: a) stronger secondary motions, and b) higher levels of turbulence, experienced by the flow with thicker inlet boundary layers. In a study also addressing the influence of inlet plane boundary layer thickness on secondary motions, Bruun [4] has made Pitot tube measurements of the mean velocity and pressure

distributions in a  $120^\circ$  bend of rectangular cross-section. In [4] a limited amount of total pressure field data is reported for three locations in a straight duct section downstream of the bend. Detailed measurements of the much weaker Reynolds stress driven secondary motions for the case of developing flow in a duct of square cross-section have been reported by Melling and Whitelaw [5], and in a series of papers by Gessner et al., the latest reference being [6]. It is noteworthy that the flow field measurements in [2,3] do not show the symmetric corner vortex structures characteristic of straight duct flow. This supports the notion that in the bend sections of these studies the cross-stream flow was influenced more strongly by the transverse mean pressure-gradient than by gradients of the Reynolds stresses.

Curved duct turbulent flow calculations based on the numerical solution of the Navier-Stokes equations have been made by Humphrey, Whitelaw and Yee [2] for their experimental configuration, and more recently by Buggeln, Briley and McDonald [7] for the flow measured by Taylor, Whitelaw and Yianneskis [3]. In [2] a two-equation  $k-\epsilon$  model of turbulence was used while in [7] the authors employed the one-equation model investigated by Shamroth and Gabeling [8]. In general, both studies show good agreement between measurements and calculations of the mean velocity components up to a bend angle of approximately  $45^\circ$ , but as of this point significant deviations appear. For bend angles larger than  $45^\circ$  calculations in [7] are in better accord with the measurements than corresponding results in [2]. This is attributed primarily to the thinner boundary layer inlet condition present in [3], which was responsible for the production of weaker secondary motions than were observed and predicted in [2]. It should be remarked that cost considerations dictated the use of coarse grids in both of the above studies and, since significant levels of numerical diffusion probably affected the results, there is an inadequate basis for judging the merits and demerits of the turbulence models used respectively by the authors.

A review of computational methods for internal flows has been carried out by McNally and Sockol [9]. The following is a brief summary relating to numerical techniques of relevance to this work. Within the class of numerical methods which neglects streamwise diffusion is the partially-parabolic procedure proposed by Pratap and Spalding [10] for calculating flow in curved ducts. In this method, iterated forward marching sweeps of the three-dimensional flow field are performed, yielding solutions of the momentum equations and corrections to the pressure field, until local and global continuity are attained. This type of numerical procedure was used by Chang et al [11] to predict the flow of [2] after modifying the procedure to include quadratic upstream interpolation of convection terms as in Han et al [12] to reduce numerical diffusion. In general, better agreement was found in [11] than in [2] between mean velocity measurements and calculations as a consequence of the numerical improvements to the calculation scheme.

The advantages of partially-parabolic procedures over fully-elliptic ones are mainly two. First, they require considerably less computer memory since, in a three-dimensional flow calculation, pressure is the only variable requiring full three-dimensional storage. The second advantage derives from the first. Due to the reduced memory requirements, with a partially-parabolic procedure it becomes feasible to compute three-dimensional flows on calculation grids refined to the point where streamwise numerical diffusion is a substantially weaker source of numerical inaccuracy. A disadvantage of the partially-parabolic procedure is the requirement of calculation times comparable to those of an elliptic procedure.

Inviscid flow approximations for the calculation of flows in curved ducts have been proposed by, for example, Briley and McDonal [13]. The numerical procedure developed by these authors represents an extension of viscous forward marching methods in that it accounts approximately for transverse variations in streamwise pressure gradient. While this approach

appears particularly promising for fast and relatively inexpensive curved flow computations, work continues on its development and application; see Krekovsky, Briley and McDonald [14].

In contrast to the pressure-dominated flows arising in curved ducts, the difficulties associated with predicting Reynolds stress driven secondary motions in ducts of non-circular cross-section are principally related to the accurate modeling of cross-stream turbulent flow anisotropy. Brundrett and Baines [15] have shown that the turbulence term contributing most strongly to mean streamwise vorticity in steady, incompressible, constant property flow is  $\frac{\partial^2}{\partial y \partial z} (\overline{u_y^2} - \overline{u_z^2})$ . In a later study, Perkins [16] also demonstrated the importance of the term  $(\frac{\partial^2}{\partial z^2} - \frac{\partial^2}{\partial y^2}) \overline{u_y u_z}$ . In these terms,  $y$ ,  $z$ ,  $u_y$  and  $u_z$  are the cross-stream coordinates and velocity fluctuations respectively. Since straight duct flows are correctly described by parabolic (boundary layer) equations, they do not pose serious impediments to accurate numerical solutions; the limitations are related to the turbulence models used. It can readily be shown that turbulence models based on the notion of an isotropic turbulent viscosity, with the implication that the principal axes of stress and strain are co-aligned, cannot account for the generation of stress-driven secondary motions. In their recent study, Naot and Rodi [17] have reviewed briefly various investigations employing Reynolds stress level closures to predict these motions. They conclude that the essential basic flow features can be predicted qualitatively with relatively simple algebraic stress closures. It is noteworthy that, except for the full Reynolds stress closure predictions by Reece [18], all numerical studies of the problem have neglected convection and diffusion contributions to the balance of  $\overline{u_i u_j}$ , thus implying the condition of an equilibrium turbulent flow.

## 1.2 The Problem of Interest

The flow configuration of interest to this study consists of a  $180^\circ$  bend of square cross-section preceded and followed by straight duct sections. Inside the bend section the flow pattern is established primarily by pressure-force imbalances. Within the downstream tangent the flow undergoes a relaxation driven by turbulence diffusion and redistribution processes. The flow configuration is directly relevant to heat exchangers, and is typical of industrial components used for coal-slurry transport. The flow patterns established in and downstream of the bend will strongly influence the detailed heat transfer characteristics dictating the overall performance of heat exchangers. Knowledge of the flow and of its turbulence characteristics is also necessary for understanding mechanisms of particle transport and surface wear by slurries.

## 1.3 Objectives of this Study

The objectives of this study have been mainly two:

1. To obtain detailed measurements by means of laser-Doppler velocimetry of the mean flow and turbulence characteristics in the curved and downstream sections of the above configuration.

In contrast to earlier work [2-6], the present configuration involves the combined effects of a  $180^\circ$  bend and downstream tangent. These are responsible for inducing a complex flow of very distinct and previously undocumented velocity characteristics. The body of experimental data offered here should be of value for extending the theoretical base required for developing and testing more comprehensive three-dimensional turbulence model formulations.

2. To test the capability of the two equation ( $k-\epsilon$ ) model of turbulence to predict the mean features of the flow configuration.



Elliptic calculations in [2] of the turbulent flow in a  $90^\circ$  bend of square cross-section yielded results in poor agreement with the measurements for bend angles larger than  $45^\circ$ . However, in that study it was not possible to separate satisfactorily the turbulence model failings from inaccuracies produced by numerical diffusion. Subsequent work by Chang et al [11] using a partially-parabolic scheme and higher order differencing of convective terms yielded substantially improved predictions. Their numerical method is employed here to establish more precisely the limitations of the  $k-\epsilon$  turbulence model for predicting strongly curved and relaxing three-dimensional confined flows.

#### 1.4 Outline of the Paper

The remainder of this paper is divided into four sections. In order, these discuss: a) The apparatus, instrumentation, experimental methodology and measurement error; b) The governing equations, turbulence model, flow field boundary conditions, finite differencing practices, solution algorithm and calculated test cases; c) The measured and calculated results, including laminar flow calculations; d) The major conclusions of this work with some specific recommendations.

## 2. THE EXPERIMENT

### 2.1 Flow System and Instrumentation

The experimental system was composed of: a water rig, of which the most important component was the flow test section; a laser-Doppler velocimeter and its associated electronic instrumentation; and a PDP 11/34 Digital Equipment Corporation minicomputer. A description of the experimental apparatus and instrumentation has already been given in [19]. A summary of that description, including later modifications to the apparatus, is provided here.

The basic components of the flow test section are shown schematically in Figure 1, and comprised two straight ducts and a bend of square cross-sections. The tangents were each 31 hydraulic diameters long and were respectively attached to the  $0^\circ$  (inlet) and  $180^\circ$  (outlet) plane of the bend. The ratio of bend mean radius of curvature to hydraulic diameter was  $R_c/D_H = 3.35$ . The bend component was constructed by machining an open, curved channel of mean radius of curvature  $R_c = 14.92 \text{ cm} (\pm 0.02 \text{ cm})$  into one of the faces of a large, flat, solid piece of plexiglass 7.6 cm thick. A plexiglass plate 1.27 cm thick was machined to fit snugly as a lid over the open channel piece, so yielding an enclosed curved duct shape of cross-section dimensions  $4.45 \times 4.45 \text{ cm}^2 (\pm 0.02 \times 0.02 \text{ cm}^2)$ . An O-ring seal placed between the open channel piece and the lid prevented water leaks. The modular form of this construction made disassembly easy for surface cleaning purposes. The upstream and downstream tangents were each 138 cm ( $\pm 0.02 \text{ cm}$ ) long and were also constructed from plexiglass, with flat walls 1.27 cm thick. These two ducts were joined by flanges to the bend, with special care taken to avoid possible mismatches between the component cross-sections which otherwise might disturb the flow.

A flow-straightening section 7.15 hydraulic diameters long was placed upstream of the straight duct attached to the bend inlet plane. The purpose of this device was to uniformize and accelerate the development of the cross-

stream plane distribution of the flow approaching the bend in the upstream tangent. Various arrangements of differently sized stainless steel screens were tested in combination with one or more perforated plexiglass plates 3.175 cm thick, containing 85 holes of 3.175 mm diameter arranged in a rectangular array spaced 4.495 mm on the centers in each direction. The most successful arrangement of plates and screens in the uniformizing section was found experimentally and is shown in Figure 2.

The test section was part of a closed loop system through which water at 20°C was made to flow by gravity from a constant head tank. From this tank the flow passed through the test section, and then into a large sump tank from where it was pumped back to the constant head tank by a 3/4 HP Burkes centrifugal pump. The constant head was ensured by a large diameter PVC overflow pipe extending through the bottom of the head tank. Flow to the head tank was controlled by a gate valve and measured using a 2 in. Barco venturi meter (P.N. 2-393) connected to a 50 in. (1.27 m) differential mercury manometer. In order to rule out the possibility of propagating perturbations induced by flow components, the use of valves, sharp bends and metering devices was avoided altogether along the test section flow loop. Flow to and from the test section tangents was channelled through 2 in. i.d. tygon tube pieces; flexible enough to be bent without kinks over a large radius of curvature, yet stiff enough to avoid wall collapse due to flow-induced pressure drop. Baffles located in the constant head tank served to dampen the swirling motion of the flow leaving the tank. Residual swirl from the head tank and secondary motions induced by mild curvature in the tygon tube upstream of the test section were eliminated by the flow-uniformizing section placed between the tygon tube and the upstream tangent. All experiments were conducted for the flow rate condition imposed by the constant head tank. This corresponded to a Reynolds number of  $Re = 62,000$  and a Dean number of  $De = 24,000$  in the flow test section.

Measurements of the mean flow and turbulence characteristics were made using the laser-Doppler velocimeter technique in backscatter mode [20]. The velocimeter employed is shown schematically in Figure 3 in relation to the flow test section. It comprised a 2 watt Lexel Argon-Ion water-cooled laser, a mirror stage for reflecting the laser beam  $180^\circ$  into the velocimeter optics, the optics, and a 4 in (10.2 cm) diameter mirror for reflecting the converging velocimeter beams from the horizontal to the vertical direction. This mirror also served the function of reflecting the back-scattered Doppler-shifted radiation into the velocimeter collecting optics. The optics were of the DISA 55X Modular Series and consisted of: two separately adjustable quarter-wave retardation plates; a 50:50 neutral beam splitter; a beam color splitter; a backscatter unit (containing a mirror inclined  $45^\circ$  with respect to the velocimeter optical axis, and serving to support at right angles to the optical axis the photomultiplier optics consisting of: a color separator; two interference filters and two RCA-4526 photomultiplier tubes); a pinhole section; a beam translator and a 310 mm achromatic focusing lens.

The laser and velocimeter optics were mounted to the top of a thick aluminum table, which was itself firmly bolted to an x, y, z traversing mechanism. The traversing mechanism could displace the table top  $\pm 7.5$  cm in  $5 \mu\text{m}$  increments along any of the coordinate axes by means of three linearly encoded stepping motors monitored by the Digital Equipment Corporation PDP 11/34 minicomputer. The minicomputer functioned as the central data acquisition and reduction controller. In addition to directing the spatial sequence of an experimental run, the computer was programmed to conduct the acquisition, statistical processing, plotting and storage of Doppler data validated and measured by a DISA 55L96 Doppler signal processor or "counter". The PDP 11/34 has a 256 K 16 bit random access memory and is equipped with dual hard RL01 magnetic disc drives (5 Mbytes each). The computer interacts by means of an

RT 11 software package with various input-output devices, including a Tektronix 4025 graphics terminal, a Decwriter II hardcopy terminal and a Tektronix 4662 digital pen plotter.

## 2.2 Experimental Methodology and Measurement Error

Prior to an experimental run, water was allowed to flow through the rig until it was purged of air bubbles and had attained a steady thermal state corresponding to  $20^{\circ}\text{C}$  ( $\pm 1^{\circ}\text{C}$ ). Mass flow through the test section was controlled by setting the constant head overflow condition to a mere trickle and continuously monitoring the pressure drop through the venturi meter connected to the head tank feed line.

At any given streamwise measurement station, the velocimeter support table was manually positioned such that the velocimeter horizontal optical axis was oriented perpendicular to the test section side; see Figure 3 for an example corresponding to a streamwise location of  $\theta = 180^{\circ}$ . Fine adjustments to the  $90^{\circ}$  beam deflector mirror ensured that the velocimeter vertical optical axis was perpendicular to the test section top surface. In combination, these adjustments produced a fringe pattern which was parallel (to within  $\pm 0.3^{\circ}$  at any  $y, z$  cross-section location) to the cross-stream plane of the test section. The velocimeter optical probe volume was formed by the intersection of two 514.5 nm (green) light beams with a half-angle in air of  $4.90^{\circ}$ , for which the volume characteristics were: a diameter of 0.09 mm, a length of 1.1 mm, and a fringe spacing of  $3.02\text{ }\mu\text{m}$  with about 28 fringes contained in the probe. In reality, spatial filtering and threshold settings on the counter reduced the dimensions of the optical probe. The probe volume was positioned at the top outer-wall corner, inside the test section, by fine control of the motorized traversing table. Positioning in the  $x$  and  $y$  coordinate directions was accurate to within  $\pm 0.05\text{ mm}$  while positioning in the  $z$  direction was accurate to better than  $\pm 0.5\text{ mm}$ .

With the reference corner position at a streamwise location established, the computer software was activated which controls signal acquisition and data processing on a sequentially scanned measurement-grid. After flow symmetry had been established at various streamwise stations, the bulk of the measurements were restricted to a symmetrical half of the test section, on a grid consisting of 4 to 5 profiles at different  $z$  locations, each containing 29 to 31 equally spaced points in the  $y$  direction. At each point on the measurement-grid the mean flow and turbulence characteristics were statistically determined from populations of 5 to 10 samples consisting of 1,000 measurements each. Each measurement was required to satisfy the counter 5/8 validation comparison to within a preset tolerance of 3%. At every validation of a Doppler burst a "data ready" signal was issued by the counter to a logic conversion circuit. This circuit then sent a triggering pulse to the computer parallel line interface module which was checked for data availability by a software loop approximately every 20  $\mu$ s. No interrupt routines were used for obtaining data due to the higher sample rates made possible by the handshake technique. Data rates of about 1 kHz, with approximately 60% validation, were obtained after the flow was seeded with cornstarch particles ranging in size between 1 and 10  $\mu$ m. Optical alignment and automatic grid scanning were performed at the following streamwise locations:  $x_H = -5, -1, 1, 5, 10, 20$  in the straight ducts, and  $\theta = 3^\circ, 45^\circ, 90^\circ, 130^\circ, 177^\circ$  in the bend.

Although capable of two-component measurements; the availability of only one counter during the early stages of this work restricted the use of the velocimeter to single channel mode for most of the experiments. Values for the streamwise component of mean velocity and normal stress,  $U_0$  and  $\overline{u_0^2}$ , were derived directly from measurements obtained with the velocimeter fringes aligned perpendicularly to the streamwise coordinate direction. Values for the transverse components,  $U_r$  and  $\overline{u_r^2}$ , and for the Reynolds stress,

$\overline{u_\theta u_r}$ , were derived as described in [2,5] by combining measurements obtained with fringes oriented at angles of  $+45^\circ$  and  $-45^\circ$  with respect to the streamwise direction. As a check, measurements of  $U_\theta$  and  $\overline{u_\theta^2}$  obtained in this manner were found to agree to within experimental error with the direct observations. Measurements involving the velocity component in the spanwise (z) coordinate direction could not be made accurately due to optical inaccessibility of the flow.

While the bulk of the measurements were made in the manner described above, with the velocimeter in single channel mode, towards the end of the experiment the availability of a second counter allowed us to perform a limited number of measurements using the two velocimeter channels simultaneously. For this case the interference fringe patterns were respectively aligned parallel and perpendicular to the streamwise velocity component. To resolve flow directional ambiguity, and also to optimize the filter range of the counters, a net frequency shift of 700 kHz was imposed on both channels using a DISA 55N10 Bragg cell combined with electronic downmixing. In this way additional measurements at  $X_H = -5, -1, 1$  and  $5$  in the respective tangents were obtained. In addition, careful checks were conducted of the data previously obtained at  $X_H = -5$  and  $5$  and at  $\theta = 3^\circ$  and  $177^\circ$ . In general, the checks showed very good agreement between the two measurement methods, for both of the velocity components and their respective normal stresses. However, at  $X_H = -5$  the two methods differed markedly with respect to the measurement of the very weak transverse velocity component arising at this location. The first method consistently showed larger scatter in the measurements and the uncertainty was ultimately traced to relatively small but significant inaccuracies associated with determining the  $\pm 45^\circ$  orientations required by this method. At  $X_H = -5, -1, 1$  and  $5$ , and  $\theta = 3^\circ$ , it is the more accurate frequency-shifted transverse velocity data which is reported here.

Error sources affecting the accuracy (systematic error) and precision (random error) of laser-Doppler measurements have been discussed by, for example, Durst, Melling and Whitelaw [20], Drain [21] and Buchhave [22]. In this study the most serious systematic errors were attributed to velocity gradient broadening and velocity bias respectively. Velocity gradient broadening has been analyzed by Melling [23] who proposed a simple method for estimating its magnitude. Various weighting methods have been proposed to correct for the velocity bias effect [21-22], but none of these is entirely satisfactory; they all involve assumptions regarding the statistical distribution of particles in the flow and, in practice, the corrections can be influenced by the additional problem of "incomplete-signal bias" [21-22]. For the conditions of this study, gradient broadening and velocity bias were estimated to be significant only in the near wall regions of the flow, where velocity gradients and turbulence intensities were highest and the data rate lowest. Fortunately, the errors are of similar magnitude and of opposite sign, tending to cancel out their respective effects on the measurements. For this reason, and because the errors were small anyway, corrections were not applied to the measurements. Table 1 presents estimates of the maximum combined inaccuracies of these two error sources on the quantities measured.

Values of the transverse mean velocity component,  $U_r$ , and of the Reynolds stress,  $\overline{u_\theta u_r}$ , were prone to a third systematic error. At the last four locations in the bend, and at  $X_H = 10$  and 20, these two quantities were derived from measurements taken at  $+45^\circ$  and  $-45^\circ$  to the streamwise flow direction. An error in setting this  $90^\circ$  angle could seriously affect the accuracy of these measurements. The problem has been considered by Humphrey [24] for a flow of similar characteristics to the present one, and he shows that an angular uncertainty of  $0.4^\circ$  can lead to an error of 5% in  $U_r$  and  $\pm 3\%$



in  $\overline{u_\theta u_r}$ . In this work special care was taken to ensure a maximum angular uncertainty of less than  $0.3^\circ$  in setting the  $\pm 45^\circ$  beam orientations.

The two main sources of random error affecting the precision of the measurements were attributed to statistical sampling uncertainty (due to the finite size of sample populations) and uncertainty in the determination of the reference or normalizing velocity,  $U_B$ . Estimates of the first uncertainty were derived from the measurements themselves and, for all quantities, were found to be less than  $\pm 1\%$  r.m.s. error. The error in  $U_B$  was larger ( $\pm 2\%$ ) and arose principally from uncertainties in the construction of the venturi meter. As a further check, the bulk mass flow at each longitudinal station was estimated by integrating the measurements. This yielded a value of  $U_B$  which was within  $\pm 6\%$  of the venturi meter measurement. Estimates of the maximum combined effects of these two errors on the measurements are provided in Table 1.

Measurements of the pressure coefficient,  $C_p$ , in the straight and curved duct test sections, using side wall pressure tapings connected to an inclined manometer bank, were also prone to a random r.m.s. error ranging from  $\pm 10\%$  at low absolute values of  $C_p$  to  $\pm 5\%$  at the higher values. The uncertainty in  $C_p$  was due mainly to the reading error associated with the manometer bank.

### 3. THE NUMERICAL PROCEDURE

#### 3.1 Governing Equations and Boundary Conditions

Three-dimensional, time averaged Navier-Stokes equations in cylindrical coordinates, modeled according to a two-equation ( $k$ - $\epsilon$ ) model of turbulence, are given in [2]. Except for the streamwise diffusion terms ( $\partial^2/\partial\theta^2$ ), exactly the same modeled partial differential equations were used for the partially-parabolic numerical predictions of this study. The  $k$ - $\epsilon$  model presumes the Boussinesq assumption, relating the stress and strain fields through the notion of an isotropic turbulent viscosity,  $\nu_t$ . This quantity is determined from the relation  $\nu_t = C_\mu k^2/\epsilon$  where, to a first approximation,  $C_\mu$  is a constant equal to 0.09.

The specification of boundary conditions was as follows. At the inlet plane ( $X_H = -5$ )  $U_x$ ,  $U_y$  and  $U_z$  were prescribed from measurements of this work; values of  $k$  were estimated from measurements of  $\overline{u_x^2}$  and  $\overline{u_y^2}$  (using symmetry considerations to derive  $\overline{u_z^2}$ , as was done for  $U_z$ ); and values for  $\epsilon$  were specified as in [25] by setting:

$$L_m = K D_H [\beta_x (1 - 1.2 \beta_x) \cdot \beta_y (1 - 1.2 \beta_y)]^{1/2} \quad (1)$$

with

$$\beta_x = \frac{x}{D_H} \left(1 - \frac{x}{D_H}\right) \quad \text{and} \quad \beta_y = \frac{y}{D_H} \left(1 - \frac{y}{D_H}\right)$$

in

$$\epsilon = C_D^{3/4} \frac{k^{3/2}}{L_m} \quad ; \quad C_D = 0.08 \quad (2)$$

At the exit plane ( $X_H = 5$ ) two types of boundary conditions were tried. First  $\partial P / \partial x$  was continuously adjusted to conform with streamwise continuity of mass, while  $\frac{\partial}{\partial x}(\partial P / \partial y)$  and  $\frac{\partial}{\partial x}(\partial P / \partial z)$  were set equal to zero. However, the results obtained did not differ from those calculated by setting  $\partial U / \partial x = 0$  at the exit plane instead. Because the  $k$ - $\epsilon$  model applies only to high Reynolds number flows, special treatment of the flow near the walls is required. This is achieved by assuming the existence of a logarithmic velocity distribution between any wall and the computed nodes nearest that wall. The additional assumption of an equilibrium flow in this region leads to a specification of the wall shear stress in terms of the wall-node velocity, kinetic energy and logarithmic law constants. Special treatments are also required for near wall determinations of  $k$  and  $\epsilon$ , and are described in [2]. It should be noticed that, except for the manner in which  $\epsilon$  was specified at the inlet plane boundary, the turbulence model in this study was identical to that in [2].

### 3.2 Finite Differencing and Numerical Algorithm

Finite difference forms of the transport equations appropriate to partially-parabolic flows were derived following the guidelines given by Pratap [26]. As in [26], an upwind differencing scheme was retained for the streamwise velocity component. However, the second-order accurate quadratic upstream interpolation technique (QUICK) proposed by Leonard [27] and tested by Han et al [12] for turbulent flow was included, providing a choice for the finite differencing of all convection terms contained in the cross-stream planes. The QUICK scheme was optional to the  $k$  and  $\epsilon$  equations as well as to the equations for velocity components. The implementation of the scheme in the numerical algorithm is summarized in Appendix I, a more detailed exposition is given by Chang [28].

The elliptic numerical procedure of [2] was modified to perform the partially-parabolic calculations of this study. The general form of the finite difference expression solved by the modified procedure is given by:

$$\phi_P = A_E^\phi \phi_E + A_W^\phi \phi_W + A_N^\phi \phi_N + A_S^\phi \phi_S + B^\phi (+ D \Delta P)^\phi \quad (3)$$

where  $\phi_P$  represents any one of the dependent variables solved at a position  $P$  in the discretized flow domain. The  $A_i^\phi$  coefficients are determined at their respective (East, West, ...) cell surfaces, and represent the combined contributions of convection and diffusion to the balance of  $\phi$ . The term  $B^\phi$  contains contributions arising from sources (or sinks) in the flow, plus the upstream convective contribution to the balance of  $\phi$ . The term in parentheses in Equation 1 arises only when  $\phi$  represents a velocity component, and accounts for the pressure gradient contribution to the balance of momentum. As in [2], the solution procedure employs a guess-and-correct sequence for the calculation of the three-dimensional pressure field. This involves the iterative calculation of both velocities and pressure, which are continuously corrected until the velocity components are in conformity with local (and global) mass continuity. In the present scheme, however, the flow variables are computed by marching through the flow domain along the main flow direction, with the flow variables at any streamwise plane being calculated solely from values at the upstream plane. The pressure field is always stored as a complete three-dimensional array. The remaining variables and coefficients are continuously recalculated and are stored temporarily as two-dimensional arrays only at the computed plane and the upstream plane adjacent to it. Details of the calculation sequence, including the pressure and velocity correction procedure and the tri-diagonal matrix algorithm solution technique, will be found in [26].

### 3.3 Testing

The correctness of the numerical procedure and of the turbulence model were separately checked by reference to calculations of several appropriately documented flows. The predicted test cases were: 2D, curved channel, developing

laminar and turbulent flows [7]; 3D straight duct, developing laminar flows with [12] and without [29] a wall sliding at right angles to the flow; 3D straight duct, developing turbulent flow [30]; 3D, 90° bend, developing laminar flows with thin [3] and thick [24] inlet boundary layers; and 3D, 90° bend, developing turbulent flow [2]. Except for the last configuration, agreement was excellent between measurements and predictions of mean flow quantities for all the test cases. As anticipated, the weak Reynolds stress driven secondary motions in the flow of [30] were not predicted by the  $k-\epsilon$  model.

Due to space limitations, detailed comparisons between measurements and predictions of the test cases are not provided here but are available in [28]. For the case of turbulent flow in a 90° bend, comparisons have been prepared by Chang et al [11] for the 1981-1982 AFOSR-HTTM-Stanford Conference on Complex Turbulent Flows. Predictions of this flow using the QUICK scheme show very encouraging agreement with corresponding measurements over an initial bend angle of 45°, but as of this position discrepancies of the order of 10-20% appear between measured and predicted values of  $U_\theta$ . In particular, the transverse location of maximum  $U_\theta$  on the symmetry plane at  $\theta = 90^\circ$  is placed at  $\eta = 0.82$  by the calculations, but is located at 0.60 in the measurements. Notwithstanding, these discrepancies are smaller than those found in [2] using the HYBRID (upwind/central) differencing technique and an elliptic numerical procedure.

Comparisons between the test cases predicted using both the HYBRID and the QUICK schemes showed clearly the superior performance of the latter for equivalent grid sizes and distribution of nodes. For example, calculations of the 90° bend laminar flow test cases using the QUICK scheme on a  $(z = 11) \times (r = 17) \times (\theta = 36)$  grid were as accurate as corresponding calculations using the HYBRID scheme on a  $(z = 15) \times (r = 25) \times (\theta = 36)$

grid. The predictions presented here for turbulent flow were restricted to an unequally spaced grid consisting of the following maximum distribution of grid nodes:  $(z = 14) \times (r = 25) \times (\theta = 45)$  in the  $180^\circ$  bend, and  $(z = 14) \times (y = 25) \times (x = 20)$  in the upstream and downstream tangents, both of length  $5 D_H$ . A typical converged run time for this grid represents  $10^{-5}$  CPUs per node visitation, and required 151  $k_B$  words of storage and a total run time of 1600s for 50 iterations. The criterion for convergence was that the maximum of the normalized residual summations should be less than  $10^{-3}$ .

Calculations of the flow were also performed on coarser grids. Comparisons of these results with the calculations provided here suggest that substantial grid refinements would be required to significantly improve the numerical accuracy of the present predictions. Computation costs simply prohibited the use of finer grids, or of extensive exploratory searches to optimize the distribution of grid nodes available.

#### 4. RESULTS AND DISCUSSION

Measurements of turbulent flow in the  $180^\circ$  bend, and in its upstream and downstream tangents, are presented and discussed in this section. These are compared with corresponding predictions at selected streamwise locations. Laminar flow predictions for the same configuration are also presented and discussed. Even though laminar flow measurements are lacking for comparison, the predictions are of value for: a) contrasting notable differences which arise in the calculations from using the HYBRID and the QUICK schemes respectively, without the complicating factors associated with turbulence model inaccuracies; b) helping to understand certain features of the turbulent flow which also arise in laminar flow regime.

In the figures corresponding to turbulent flow, calculated profiles are plotted for  $2z/D_H = 0$  and  $0.50$  only. Where the HYBRID and QUICK results coincide, a single profile is shown. Otherwise, HYBRID results are plotted as continuous lines and QUICK as dashed lines. The reader should note that dashed lines have also been used in some graphs for plotting best fits to experimental data with a larger than normal degree of scatter at the  $2z/D_H = 0.75$  and  $0.875$  spanwise locations. Because photographic reduction of the figures presented in this section for discussion has reduced the accuracy with which readings can be made from them, full scale plots of the turbulent flow data are provided in Appendix II. Laminar flow calculations are given in Appendix III.

##### 4.1 Turbulent Flow Measurements and Calculations

Measurements of the flow in the upstream tangent, taken at  $X_H = -5$  and  $-1$  are shown in Figures 6 and 7 respectively. Comparing the data at these two stations, particularly the Reynolds stress measurements shown in Figure 17, suggests that the flow is still developing at  $X_H = -5$ , after travelling a distance of  $30 D_H$  from the uniformizing section. Figures 5 and 17 provide

comparisons of the measurements at  $X_H = -1$  with corresponding profiles interpolated from the data obtained by Melling and Whitelaw [5] at 36.8 hydraulic diameters in a straight duct of square cross-section. The two data sets are in agreement to within the experimental error of the measurements. Since the measurements by Melling and Whitelaw correspond to an essentially developed flow, the differences shown in Figure 5 for the radial (transverse) velocity component are attributed mainly to the elliptic influence of the bend on the flow in the tangent. Similar observations on the influence of a bend on its upstream tangent flow have been noted by Humphrey et al [2] and Taylor et al [3] in the same  $90^\circ$  bend configuration but with differing inlet conditions. Taylor et al found that in a turbulent flow with relatively thin boundary layers the bend influenced the measurements taken at  $X_H = -0.75$ , their furthest upstream location. Measurements at  $X_H = -2.5$  taken by Humphrey et al with essentially fully developed flow conditions in the upstream tangent suggested only a weak elliptic effect of the bend on the flow at this location. However, these authors did not measure the transverse velocity component; their commentary is based on the unchanged appearance of streamwise velocity and turbulence intensity contours between  $X_H = -11$  and  $X_H = -2.5$ . By contrast, for the conditions of the present experiment, the velocity data suggests that the favorable streamwise pressure gradient along the inner wall of the bend (see Figure 4) induces a mean transverse flow directed at the inner wall which is already noticeable at  $X_H = -5$ . Although weak ( $U_r/U_B \approx 0.02$ ), it appears that the transverse flow induced by pressure forces in the upstream duct overcomes the weaker stress-driven cross-stream motion (shown clearly in the measurements of Melling and Whitelaw), and results in  $U_r$  profiles whose shapes, and variations of shape with  $z$  location, agree qualitatively with a simple superposition of the pressure-induced and stress-driven cross-stream flows.



Calculations of  $U_r$  at  $\theta = 3^\circ$  (and between this location and  $X_H = -5$ , not given here) always showed the flow moving towards the convex wall-side of the test section. Because the turbulence model is insensitive to stress-driven secondary motions, this result, and the calculated displacement of the maximum in  $U_\theta$  towards the convex wall, clearly support the experimental finding that elliptic effects are transmitted from the bend into the upstream tangent via the pressure field, farther than has previously been observed. As with the  $U_r$  velocity component, the discrepancies shown between calculated and measured turbulent stresses at  $\theta = 3^\circ$  arise from the assumption of isotropy in the turbulence model. To predict more accurately the cross-stream motion and turbulent stresses in the upstream tangent requires modeling of important anisotropic flow characteristics such as near-wall pressure-strain effects. These effects cannot be dealt with in the context of the model employed here.

The mean velocity and turbulent stress data taken at different streamwise locations in the bend are plotted in Figures 8-12 and 18. The pressure drop measured at the side wall of the bend is shown in Fig. 4. In general, the sense of the flow up to  $\theta = 90^\circ$  is in agreement with earlier observations of, for example, Humphrey et al [2] and Taylor et al [3]. Closer inspection of the plots reveals additional interesting features. The measurements of the pressure coefficient  $C_p$  show the initially expected opposing pressure gradient at the concave wall and the favorable gradient at the convex. In contrast to the data measured in [3] for a  $90^\circ$  bend, the maximum and minimum values of  $C_p$  do not coincide at the same streamwise location. In this work the value of  $C_p$  maximizes at the concave wall at  $\theta \approx 45^\circ$ , and attains its minimum value at the convex wall at  $\theta \approx 177^\circ$ . As of  $\theta \approx 45^\circ$ , the streamwise pressure gradient is favorable throughout most of the bend. At  $\theta = 3^\circ$  the

streamwise velocity profiles all shown their maximum values displaced towards the inner radius wall, due to the favorable streamwise pressure gradient there. The radial component of velocity is everywhere directed towards the inner wall except for a small flow region about the symmetry plane. This region marks the inception of secondary flow, driven by the transverse pressure gradient which arises due to lateral curvature of the main flow in the bend. The secondary flow is more intense at  $\theta = 45^\circ$  as shown in Figure 9. At  $\theta = 45^\circ$ , the profile for  $U_r$  near the side wall ( $2z/D_H = 0.75$ ) shows a large negative velocity, while the profiles at the other  $z$  locations are large and positive. The sense of motion is from the convex to the concave surface along the symmetry plane, and back to the convex surface along the side walls of the bend. As of  $\theta = 45^\circ$ , measurements of  $U_r$  at all  $z$  locations show this component always positive (directed from the convex to the concave surface). This means that the cross-stream plane return flow adjacent to a flat wall in the bend is confined to a narrow region less than  $D_H/8$  in width. A simplified mass balance at  $\theta = 90^\circ$  suggests that the radial component of velocity in this narrow region varies between 0 at the wall and a maximum of about  $0.40 \times U_B$  at the peak location. This result is in qualitative agreement with the observations of Taylor et al [3]. The highest return flow measured by them ( $0.40 \times U_B$ ) was found at  $2z/D_H = 0.95$  and  $\theta = 60^\circ$  in a  $90^\circ$  bend with  $Re = 40,000$  and  $R_C/D = 2.3$ . Calculations of the present flow gave a peak value of  $U_r/U_B = 0.30$  at  $2z/D_H = 0.95$ , at the  $90^\circ$  plane.

Between  $\theta = 3^\circ$  and  $90^\circ$ , the influence of destabilizing curvature raises the levels of all the measured Reynolds stresses at the concave wall of the bend. The effect is particularly noticeable in the plots for the stresses at  $\theta = 45^\circ$ , and has decreased by the time the flow reaches the  $\theta = 90^\circ$  plane. Similar observations have been made by Eskinazi and Yeh [31] in a two-dimensional curved channel flow, and by Humphrey et al [2] and Taylor et al [3] in their respective curved duct flows. In particular, Eskinazi and Yeh

demonstrate the strong generation of  $\overline{u_r^2}$  near a concave wall and its corresponding suppression near a convex wall. While at  $\theta = 45^\circ$  the present flow is already three-dimensional, the results for  $\tilde{u}_r/U_B$  are in qualitative agreement with the observations of Eskinazi and Yeh. Destabilizing and stabilizing curvature effects at the respective concave and convex walls of the present flow are responsible for producing large levels of anisotropy. For example, at  $\theta = 45^\circ$ ,  $\overline{u_\theta^2}/\overline{u_r^2} \approx 2$  near the concave wall. Wall-dampening of radial fluctuations in the flow, coupled with pressure redistribution and turbulent diffusion [31] of energy between the normal stresses, account for the larger levels of  $\overline{u_\theta^2}$ .

At  $\theta = 90^\circ$  and  $130^\circ$ , plots of the two velocity components and their corresponding normal stresses show striking variations in the radial coordinate direction. These take the form of relatively large decelerations in the mean flow components at about  $\eta = 0.4$  and are accompanied by relatively large increases in  $\tilde{u}_\theta$  and decreases in  $\tilde{u}_r$  respectively at the same locations. The streamwise deceleration of  $U_\theta$  and  $U_r$  is due to the "pumping" of low speed fluid from the peripheral region of the duct into the core of the flow. Whereas viscous effects provide the mechanism for flow retardation at the walls, it is the inviscid mechanism of lateral flow curvature which drives the cross-stream motion. The phenomenon has been analyzed and described in depth by Hawthorne [32], and Horlock and Lakshminarayana [33] discuss it extensively in the context of turbomachinery aerodynamics. In particular, the latter authors provide general expressions for the generation of streamwise vorticity including the influence of Bernoulli surface rotation and viscous effects. Hawthorne shows that in flows where the angle,  $\phi$ , between the direction of normal acceleration and the normal to the Bernoulli surface (a surface of constant total pressure) is  $\phi \neq 0$ , streamwise vorticity is induced. For a small bend deflection angle  $\theta$  in a flow with initial uniform vorticity

$\Omega_0$  in the plane of the bend, the expression derived by Hawthorne [32] is:

$$\xi_\theta = -2 \Omega_0 \theta \quad (4)$$

The same result was obtained by Squire and Winter [34] using a different analytical approach and is valid for Bernouilli surfaces which remain undisturbed during passage through bend ( $\phi = \text{constant}$ ).

It is important to realize that the inviscid mechanism acts over the entire cross-section of the flow (provided  $\phi \neq 0$ ). For the kind of flow of interest here, the distortion of Bernouilli surfaces during passage of the flow around the bend cannot be neglected. A first approximation accounting for this distortion leads to an equation for  $\alpha$ , the angle by which the Bernouilli surfaces turn. The result derived by Hawthorne [32] is:

$$\left(\frac{D_H}{R_C}\right) \frac{d^2 \alpha}{d\theta^2} = \cos \alpha \quad (5)$$

This equation is analogous to that governing the motion of a pendulum and, as shown by Hawthorne, predicts that the flow through a bend should oscillate between  $\alpha = 0$  and  $\alpha = \pi$  with a period (or bend angle) for a complete oscillation approximately equal to  $2\pi/\sqrt{R_C/D_H}$ . The secondary motion is analogous to the kinetic energy of the pendulum and also oscillates with the same period, passing through zero after each  $\pi\sqrt{D_H/R_C}$  radians of turn. For the present flow a complete oscillation corresponds to about  $197^\circ$ . This means that at about  $98^\circ$  the inviscid mechanism starts working to oppose the original sense of the cross-stream motion, with a maximum negative amplitude at  $\theta = 148^\circ$ . The result, as shown in Figures 11 and 12 for  $\theta = 130^\circ$  and  $177^\circ$ .

For  $\theta = 90^\circ$  and  $130^\circ$ , plots of the Reynolds stresses show large changes at the radial positions where  $U_\theta$  and  $U_r$  have been decelerated. Transport equations for the turbulent stresses can be obtained [35], and for  $\overline{u_\theta^2}$  and  $\overline{u_r^2}$  they take the forms given below:

$$\frac{D}{Dt} \left( \frac{\overline{u_\theta^2}}{2} \right) = - \overline{u_\theta u_r} \frac{\partial U_\theta}{\partial r} - \overline{u_\theta^2} \left( \frac{1}{r} \frac{\partial U_\theta}{\partial \theta} + \frac{U_r}{r} \right) - \overline{u_\theta u_z} \frac{\partial U_\theta}{\partial z} + P_\theta^S + D_\theta \quad (6)$$

$$\frac{D}{Dt} \left( \frac{\overline{u_r^2}}{2} \right) = - \overline{u_r^2} \frac{\partial U_r}{\partial r} + \overline{u_\theta u_r} \left( \frac{U_\theta}{r} - \frac{1}{r} \frac{\partial U_r}{\partial \theta} \right) - \overline{u_r u_z} \frac{\partial U_r}{\partial z} + P_r^S + D_r \quad (7)$$

In the above equations,  $P_\theta^S$  and  $P_r^S$  represent pressure strain redistribution terms,  $D_\theta$  and  $D_r$  denote the effects of turbulent diffusion and dissipation, and viscous diffusion is neglected. The terms written out explicitly on the right-hand side of these two equations represent generation of the stress component and, hence, of the kinetic energy of turbulence,  $k$ . Analysis of the normal stress equations, including the effects due to pressure strain, turbulent diffusion and dissipation, while desirable, is hampered by the unavailability of appropriate experimental data; hence, the contributions of the latter terms to the respective balances cannot presently be established. Nevertheless, simplified analysis of the generation terms alone provides a basis for checking consistency in the measurements and can shed light on the behavior of the flow. In the vicinity of the bend symmetry plane, symmetry considerations support the notion that the generation terms in Eqns. (6 and 7) involving the  $z$  coordinate direction should be small relative to those involving variations in the  $r$  and  $\theta$  directions. Approximate balances for  $\overline{u_\theta^2}$  and  $\overline{u_r^2}$  are then given by:

$$\frac{D}{Dt} \left( \frac{\bar{u}_\theta^2}{2} \right) = - \underbrace{\bar{u}_\theta \bar{u}_r \frac{\partial \bar{u}_\theta}{\partial r}}_A + \bar{u}_\theta^2 \left[ \underbrace{-\frac{1}{r} \frac{\partial \bar{u}_\theta}{\partial \theta}}_B - \underbrace{\frac{\bar{u}_r}{r}}_C \right] \quad (8)$$

$$\frac{D}{Dt} \left( \frac{\bar{u}_r^2}{2} \right) = - \underbrace{\bar{u}_r^2 \frac{\partial \bar{u}_r}{\partial r}}_D + \bar{u}_\theta \bar{u}_r \left[ \underbrace{\frac{\bar{u}_\theta}{r}}_E - \underbrace{\frac{1}{r} \frac{\partial \bar{u}_r}{\partial \theta}}_F \right] \quad (9)$$

At  $90^\circ$   $\bar{u}_\theta \bar{u}_r$  is positive everywhere and, except for a small region  $0.2 \leq \eta \leq 0.4$  where  $\partial \bar{u}_\theta / \partial r$  is negative, term A represents a negative contribution to the balance of  $\bar{u}_\theta^2$ . From  $\theta = 45^\circ$  to  $90^\circ$  the streamwise velocity component  $U_\theta$  is decelerated between  $\eta \approx 0.2$  and  $0.5$  by the inviscid mechanism explained above. The result is for term B in Eq. (8) to contribute positively (together with term A) to the balance of  $\bar{u}_\theta^2$ . At all radial locations near the symmetry plane, term C represents a reduction in the magnitude of  $\bar{u}_\theta^2$ , but because of the small values of the ratio  $\bar{u}_r/r$ , the contribution of this term relative to A and B is small. As shown in Figure (10), the net result is to produce a local increase in the magnitude of  $\bar{u}_\theta$  between  $\eta = 0.4$  and  $0.5$  approximately.

In a similar manner, the localized minimum in  $\bar{u}_r$  at  $\eta \approx 0.4$  in the  $90^\circ$  plane can be explained. At all radial locations term E in Eq. (9) contributes positively to the balance of  $\bar{u}_r^2$ , although weakly near the position of the minimum in  $\bar{u}_r$  because of the small magnitude of  $\bar{u}_\theta \bar{u}_r$  there. Between  $\theta = 45^\circ$  and  $90^\circ$  the plots for  $U_r$  show that, as for  $U_\theta$ ,  $U_r$  has also been decelerated leading to a positive contribution of term F to the balance of  $\bar{u}_r^2$ . However, the relatively strong streamwise deceleration in  $U_r$  induces large radial variations in its profiles producing regions in the flow where  $\partial \bar{u}_r / \partial r$  is large and positive. As shown in Fig. (10), this occurs between  $\eta \approx 0.2$  (at

$2z/D_H = 0.75$ ) and 0.7 (at  $2z/D_H = 0$ ) and leads to a negative contribution of term D to the balance of  $\overline{u_r^2}$ . Since term D is the only one contributing negatively to  $\overline{u_r^2}$  it must be the cause for the local minima in the profiles for  $\overline{u_r^2}$  at  $\theta = 90^\circ$ . Therefore, the effect of this term in the balance must be large. It appears that the two terms, B in Eq. (8) and D in Eq. (9), are the principle source and sink for  $\overline{u_\theta^2}$  and  $\overline{u_r^2}$  respectively in this simplified analysis. The gradual disappearance of the maxima in  $\overline{u_\theta}$  and the minima in  $\overline{u_r}$  between  $\theta = 130^\circ$  and  $177^\circ$  is due to the inviscid oscillatory nature of the flow since, by restoring high speed fluid to the core of the flow (see Figures 11 and 12), the respective roles of terms B and D in Eqns. (8 and 9) are reversed.

The anisotropic effects in  $\overline{u_\theta^2}$  and  $\overline{u_r^2}$  discussed above can not be reproduced by the calculations. Nor is it surprising that the minima observed in the experimental profiles for the mean velocity components at  $\theta = 90^\circ$  and  $130^\circ$  are not predicted. The assumption of local isotropy in the turbulence model produces such large levels of *false physical diffusion* as to preclude an accurate spatial resolution of the flow. For example, at  $\theta = 90^\circ$  in the symmetry plane of the bend, estimates of  $v_t/v$  from the measurements suggest that the ratio is less than 10 between  $\eta = 0.1$  and 0.9. However, calculations of this ratio at the same  $z = 0$  location vary from 40 ( $0 \leq \eta \leq 0.4$ ) to 300 ( $0.4 < \eta \leq 0.95$ ). Although *numerical diffusion* compounds the problem, the fact that it is the more accurate QUICK scheme results which show *worse* agreement with the measurements at this location, strongly supports the contention that the source of false diffusion is more physical in nature (due to the model) than it is numerical (due to the differencing scheme). In fact, the higher levels of numerical diffusion in the HYBRID scheme distort physical diffusion in the turbulence model and lead to the incorrect impression of better predictions at various streamwise locations!

In general, the QUICK scheme calculations of mean radial velocity show better qualitative agreement with the measurements than the HYBRID results. Both schemes yield calculated values of  $k$  which are in reasonably good agreement with estimates of  $k$  from the measurements; with  $k_{\text{meas}}$  approximated as  $k_{\text{meas}} = \frac{1}{2}(\overline{u_\theta^2} + 2 \overline{u_r^2})$ . However, the agreement is misleading. When summed, the experimentally determined maxima in  $\overline{u_\theta^2}$  and the minima in  $\overline{u_r^2}$  compensate to yield fairly uniform radial distributions of  $k_{\text{meas}}$ . To indicate clearly the inadequacy of the model, the plots provided show comparisons between predicted values of  $\bar{u}_\theta$  and  $\bar{u}_r$  (calculated assuming  $\overline{u_\theta^2} = \overline{u_r^2} = \frac{2}{3} k_{\text{calc}}$ ) and direct measurements of these stresses at  $2z/D_H = 0$  and  $0.5$ .

In several of the plots, both of the profiles given for  $U_\theta$  at  $2z/D_H = 0$  and  $0.5$  respectively show larger values of this component than were actually measured, suggesting different values for the experimental and computed mass flows in the streamwise direction. In fact, predictions of  $U_\theta$  nearer the wall, not shown here, yielded values smaller than those measured and gave the required mass balance.

Numerical experiments showed that a smaller length scale specification in Eq. (2) ( $\ell_m \approx 0.01 D_H$ ) at the inlet plane ( $X_H = -5$ ) led to considerably reduced levels of the predicted turbulent kinetic energy. As a consequence, even though there was much worse agreement between predicted and estimated values of  $k$ , in the vicinity of  $\theta = 90^\circ$  profiles of  $U_\theta$  (but not of  $U_r$ ) showed the local minima displayed by the measurements. Again, this type of partial agreement is misleading since it is artificially *reduced physical diffusion* (through the specification of a larger dissipation at the inlet plane) which yields the result. In general, much better overall predictions were obtained by prescribing an inlet plane length scale variation as outlined in section 3.1.



At  $\theta = 177^\circ$  the flow in the bend shows all the maxima in the  $U_\theta$  profiles displaced towards the concave wall in the presence of relatively large levels of transverse flow. Even though the radial velocity component has been decreasing steadily from about  $\theta = 90^\circ$  due to the oscillatory inviscid flow mechanism, there is no evidence in the  $U_r$  profiles at any location in the bend of a Dean instability in the vicinity of the concave wall. The instability is of the type found by Taylor in concentric cylinder flows [36] and has been observed experimentally by, for example, Cheng et al [37]. It has been predicted numerically only in laminar flow regime [38-40]. Conceivably, in a bend of larger deflection angle than the present one, the inviscid flow oscillation could also induce an extra pair of vortices in the vicinity of the concave wall. There is supporting evidence for this conjecture in Figure 8 (Station 12) of Hawthorne's paper [32] and in the measured results of this work at  $X_H = 1$ . At this location the inviscid flow mechanism has not ceased to apply completely because of the persistence of streamline curvature in the flow. Such a mechanism for generating an extra pair of vortices in the cross-stream plane is distinct from the Dean instability which is associated with destabilizing curvature effects. At  $\theta = 177^\circ$  both of the normal stresses display a surprising degree of uniformity and the shear stress is small, implying that the flow is well-mixed and relatively isotropic at this location. Except for  $U_r$ , at this station the calculations are in very good agreement with the measurements. Although inaccurate in terms of absolute values, QUICK scheme predictions of  $U_r$  are vastly superior to those obtained with the HYBRID scheme. The QUICK scheme faithfully reproduces the measured profile curvatures while the HYBRID scheme predicts negative values where none exist in the measurements!

At  $X_H = 1$  (Figure 13) the secondary flow emerging from the bend has experienced a drastic change in both its magnitude and sense. The radial velocity component has been reduced to less than about 4% and a transverse flow appears near the concave wall, opposite in sense to that existing within the bend at the same radial location. A similar observation was made by Taylor et al [3] in their laminar flow measurements at  $X_H = 2.5$ . As mentioned above, the phenomenon is attributed to the persistence of the inviscid flow mechanism downstream of the bend. Because of the fairly uniform and similar levels of the normal stress components measured at  $\theta = 177^\circ$  and  $X_H = 1$ , it is unlikely that gradients of these stresses are altering significantly the intensity and pattern of the cross-stream flow at these stations.

As of  $X_H = 0$  the flow in the downstream tangent reverts slowly to a straight duct flow condition, with the maximum in the  $U_\theta$  component tending towards the duct center. However, the maximum has moved only a small amount, from  $\eta \approx 0.9$  to a value of about 0.65 over a duct length of  $20 D_H$ . Similar indications of developing straight duct flow also appear in the profiles for the longitudinal turbulence intensity  $\bar{u}_\theta/U_B$  and the shear stress at  $X_H = 5, 10$  and  $20$  (see Figures 14-16 and 19). By contrast, the transverse components of mean velocity and turbulence intensity do not show the same rates of adjustment to the new flow conditions. The profiles for  $U_r$  indicate that as of  $X_H = 5$  a cross-stream flow pattern, similar but much weaker to that in the bend, arises in the downstream tangent. At  $X_H = 2.5$ , their furthest downstream station, Taylor et al observed the same result in their turbulent flow measurements.

The resurgence of a bend-like secondary motion in the downstream tangent is surprising and, at present, not fully understood. Calculations of the flow between  $X_H = 0$  and  $5$ , using the QUICK scheme are in qualitative

agreement with the measurements. In particular, the transverse variations of  $U_r$  at  $2z/D_H = 0$  and  $0.5$  are correctly simulated by QUICK but incorrectly simulated by HYBRID. The persistence of a peak in  $U_\theta$  near the convex-wall side of the duct at  $2z/D_H = 0.50$  (see Fig. 14) is due to turbulence model deficiencies. Because of smearing by numerical diffusion, this is not reflected in the HYBRID calculation.

Predicted cross-stream vector plots and streamwise velocity contours of the flow at  $\theta = 177^\circ$  using the two differencing schemes are given in Fig. 20. The results show that the HYBRID scheme predicts two large vortices per half-symmetry plane in the bend while the QUICK scheme predicts essentially one, with a second, much smaller counter-rotating vortex, at the convex wall. The HYBRID results are in blatant disagreement with the measurements, the QUICK results are in qualitative agreement and this situation persists up to the exit plane at  $X_H = 5$ .

#### 4.2 Laminar Flow Calculations

Laminar flow calculations were performed for the same configuration investigated in turbulent flow and are presented in Appendix III. Two cases were predicted corresponding to a  $Re = 890$  and  $De = 344$ . In the first case a plug flow inlet condition was specified for  $U_\theta$ , while in the second case a parabolic distribution was used. In both cases the inlet plane cross-stream velocity components were set equal to zero. The other boundary conditions used were: a) no slip and impermeable surfaces at all walls; and b) fully developed flow condition at  $X_H = 5$ . The inlet plane was fixed at  $X_H = -5$ .

In the plots cross-stream and streamwise velocities have been normalized by the bulk average velocity,  $U_B = 0.02$  m/s. The outer (concave) wall position is located at the top of each plot, while the inner (convex) wall position is shown at the bottom. In each figure, the top two plots correspond to QUICK scheme calculations and the bottom two correspond to HYBRID scheme calculations. Because of flow symmetry only one half of the test section cross-section is shown in the figures.

##### Plug Flow Inlet Condition

QUICK scheme (QS) and HYBRID scheme (HS) calculations of this case show clearly at  $\theta = 3^\circ$  that the flow entering the bend is influenced by two effects. One is the tendency of the streamwise velocity component to slow down along the periphery of the duct while it speeds up in the center; the other is the inception of the pressure driven secondary motion, that is, generation of streamwise vorticity at the side walls of the bend by deflection of transverse vorticity in the streamwise direction. Both schemes show higher values of the  $U_z$  component at the convex wall.

At  $\theta = 45^\circ$  the HS shows the maximum in  $U_\theta$  displaced towards the concave wall, while the QS places the maximum at the center of the duct and predicts slightly lower levels of secondary motion. Larger levels of numerical diffusion in the HS produce early thickening of the side-wall boundary layers necessary for inducing the secondary motion.

At  $\theta = 90^\circ$  both schemes show the appearance of a second but weaker vortex near the convex wall, counter-rotating to the main secondary motion. This vortex is attributed to a less favorable streamwise pressure gradient at the convex wall as of  $\theta \approx 90^\circ$ . At  $\theta = 130^\circ$  the QS shows the convex wall vortex extended over a larger region on the convex wall-side of the flow, and at  $177^\circ$  shows it has disappeared. By contrast, the HS shows that the convex wall vortex has disappeared by  $\theta = 130^\circ$ , and instead predicts a Dean-type instability in the form of a new vortex at the destabilizing concave wall. The concave-wall vortex predicted by the HS persists at all streamwise locations as of  $\theta = 130^\circ$ , but never appears in the QS calculations. This may seem puzzling at first, since concave wall vortex pairs are known to arise in curved duct flow [37] and are responsible for "pumping" low speed fluid from the concave wall into the flow along the symmetry plane. However, they have been predicted only for fully developed laminar flow conditions [38-40], or in developing laminar flows with initially thick side-wall boundary layers [13] (flows with relatively large viscous effects). The larger levels of numerical diffusion associated with the HS produce early thickening of the side wall boundary layers and yield conditions favorable to the formation of the concave wall vortex pair. Overall, the HS predicts a flow tending to full development more quickly than the flow predicted by the QS.

In both cases the QS and HS predictions show drastic reductions in the magnitude of the cross-stream motion of the flow leaving the bend which drops

from about  $0.20 \times U_B$  at  $\theta = 177^\circ$  to about  $0.05 \times U_B$  at  $X_H = 1$ . There is a striking difference in the sense of the transverse flow along the symmetry plane at these two locations. Whereas the QS always shows this flow moving radially outwards, the HS predicts a motion radially inwards in the concave wall region of the flow.

#### Parabolic Flow Inlet Condition

Specification of a parabolic inlet flow condition immediately imposes the presence of transverse vorticity throughout the entire flow entering the bend. This is in contrast to the plug flow case discussed above, for which transverse vorticity must be diffused and convected from the side walls of the bend as the flow evolves. In this sense, the present case has more in common with the measured turbulent flow than the plug flow case.

At  $\theta = 3^\circ$  both the QS and the HS calculations show a weak radial velocity component directed from the concave to the convex wall, in response to the favorable  $\partial P / \partial \theta$  at the convex wall. However, the  $U_\theta$  contours show little influence of the transverse flow. At  $\theta = 45^\circ$  a strong secondary motion has evolved and at the side wall  $U_r \approx 0.65 \times U_B$ . The higher secondary motion predicted relative to the plug flow case is due to the thicker side-wall boundary layer in the present flow.

At  $\theta = 45^\circ$  and  $90^\circ$  the QS predictions reveal the presence of a corner vortex on the convex wall due to viscous effects. This vortex is associated with local separation and produces the "wall stall" observed on the suction surfaces in cascade flows [33]. The HS predictions fail to reveal its presence.

Between  $\theta = 90^\circ$  and  $177^\circ$  transverse variations of  $U_\theta$  predicted by the QS are in very good qualitative agreement with the turbulent flow measurements; corresponding predictions using the HS are not. The role of the inviscid

flow mechanism is clearly shown: initially low speed flow from the convex wall is pumped into the core of the flow ( $\theta = 90^\circ$ ), the trend being reversed subsequently to restore high speed fluid in the core ( $\theta = 130^\circ$ ). The oscillating character of the flow in the bend is also supported by QS predictions of the cross-stream velocities. The vector plots show that the magnitude of the secondary motion is largest at  $\theta \approx 45^\circ$  and smallest at  $\theta \approx 130^\circ$  (in agreement with the inviscid flow analysis of Hawthorne [32]). In the present case, viscosity dampens the oscillation and reduces the magnitude of the secondary motion in passage through the bend. In a long enough bend, a non-oscillating asymptotic flow condition should eventually be reached.

As in the plug flow case, between  $\theta = 45^\circ$  and  $130^\circ$  the QS predictions reveal a convex-wall vortex adjacent to the symmetry plane. By  $\theta = 177^\circ$  the vortex has disappeared. The HS reveals the presence of this vortex between  $\theta = 45^\circ$  and  $130^\circ$  only. Likewise, the presence of a Dean-type vortex structure at the concave wall is revealed by both calculation schemes as of  $\theta = 130^\circ$ . At  $\theta = 177^\circ$  the size and intensity of the Dean-type vortex predicted by the QS are larger than the values predicted by the HS. Numerical diffusion in the HS predictions is responsible for smearing out this vortex structure and reducing its intensity in passage through the bend. The combined pumping of low speed fluid from both curved walls into the core flow along the symmetry plane has the effect of isolating a region of high speed streamwise flow between the side wall and symmetry plane of the bend.

Downstream of the bend, plots of the cross-stream flow predicted using the QS show the quick decay of two cross-stream vortical structures whose origins were the pressure driven secondary motion and Dean instability respectively in the bend. Strictly, these two mechanisms are not independent in the present configuration. Due to the unit aspect ratio of the duct, there

exists a synergic interaction between them. HS calculations at the same locations ( $X_H = 1$  and 5) show a faster decay of the structures, which is attributed to numerical diffusion. It is interesting to observe that the sense of the transverse velocity component predicted by the QS at  $X_H = 1$  is in complete qualitative agreement with the turbulent flow measurement of this component, shown in Figure 13 of the text.

For both the plug flow and the parabolic flow inlet distributions, it is important to note that the respective flows in the bend did not reach a fully developed state and were significantly influenced by the presence of the downstream tangent.



## 5. CONCLUSIONS AND RECOMMENDATIONS

The new measurements provided here for the mean flow in strongly curved 180° bends reveal features which are in qualitative agreement with results obtained from inviscid flow analysis. Measurements of the turbulence characteristics of the flow at  $\theta = 90^\circ$  and  $130^\circ$  show striking variations in the radial direction which appear to be due to large shearing motions induced by the inviscid mechanism in the core of the flow. Within the context of an interpretation which neglects turbulence diffusion and pressure redistribution effects, the velocity gradients induced in the core of the flow work locally on the turbulent stresses to increase the longitudinal stress component ( $\overline{u_\theta^2}$ ) and decrease the radial stress component ( $\overline{u_r^2}$ ).

Between  $\theta = 0^\circ$  and  $45^\circ$ , stabilizing and destabilizing curvature effects at the convex and concave wall respectively are responsible for generating relatively large levels of anisotropy near these surfaces. As of  $\theta = 45^\circ$ , the cross-stream motion contributes to the production of a more complicated anisotropic pattern in the turbulent stresses. For example, regions of negative production of turbulent kinetic energy arise at  $\theta = 90^\circ$ . Between  $\theta = 130^\circ$  and  $177^\circ$  the anisotropy in the measured normal stresses is reduced, due to the uniformizing influence of the secondary motion in the flow.

Measurements of  $U_r$  in the bend show that, except for around  $\theta = 45^\circ$ , the return flow in the cross-stream plane is restricted to fairly narrow bands of width  $\approx D_H/8$  adjacent to each of the side walls. The measurements of  $U_r$  did not reveal vortex structures at the convex wall in the bend, nor at the concave wall where they might be expected to arise due to the Dean instability. However, the sense of the cross-stream flow at  $X_H = 1$  does suggest a brief appearance of this type of instability in the exit tangent.

Between  $\theta = 0^\circ$  and  $X_H = 20$  there was no evidence in the measurements of a significant Reynolds stress driven secondary motion.

In this investigation the influence of the bend on the upstream tangent flow is already noticeable at  $X_H = -5$ . Although weak, a transverse flow is set up at this location (and at  $X_H = -1$ ) of characteristics which correspond with the simple notion of a superposition of two cross-stream motions: the first induced by Reynolds stress gradients in the cross-stream plane; the second due to the favorable streamwise pressure gradient arising at the convex wall in the bend. In the downstream tangent secondary motions are drastically decreased between  $\theta = 180^\circ$  and  $X_H = 1$ . The decrease is related to the oscillating nature of the secondary motion which, as shown by inviscid flow theory and supported by the present results, as of  $\theta = 90^\circ$  has started opposing the initial source of circulation set up by the transverse pressure gradient in the bend. Between  $X_H = 1$  and 20 the flow reestablishes characteristics typical of straight ducts. However, the measurements show the persistence of a weak secondary motion in the downstream tangent with the same sense of rotation as the flow in the bend and a slow recovery of the radial normal stress compared to the longitudinal component.

Predictions of the experimental flow were made with a  $k-\epsilon$  model of turbulence using a partially-parabolic numerical procedure. Two finite differencing techniques were used with global accuracies of first order (HYBRID) and second order (QUICK). Testing and predictions with QUICK in the laminar flow regime clearly showed it to be superior to HYBRID. The differences between the results obtained using the two schemes in turbulent flow are notable. Of the two, only QUICK reproduces correctly the trends in the measured cross-stream flow. The HYBRID scheme gives the incorrect impression of better streamwise component velocity predictions. This is due to numerical diffusion which smears out the spacial variation of this

component. Although QUICK scheme predictions for  $U_\theta$  differ more from the measurements, this is explained by the fact that with numerical diffusion reduced, it is the false physical diffusion in the  $k-\epsilon$  model which is revealed by the computed results.

Numerical experiments confirmed a fairly strong sensitivity of the model to the inlet plane specification of dissipation. Fixing a small-but incorrect-dissipation length scale at the inlet plane led to somewhat improved predictions of the  $U_\theta$  component at  $\theta = 90^\circ$ , where this component shows large changes in the transverse direction. However, predictions of  $U_r$  and of  $k$  were much less satisfactory.

In an earlier study [11] it was reported that predictions of turbulent flow in a  $90^\circ$  bend were mildly sensitive to the sense of cross-stream flow fixed at the inlet boundary condition. The effect was too small to alter significantly the streamwise evolution of the flow. In this study, insignificant differences were observed between predictions of the flow with the cross-stream motion set equal to zero, and predictions with the cross-stream motion specified from the measurements. The insensitivity of the flow in a bend to the inlet plane streamwise component of vorticity is explained by reference to the general form of the equation for the variation of this quantity along a streamline [33]:

$$\frac{\partial}{\partial s} \left( \frac{\xi_\theta}{V} \right) = - \frac{2\xi_r}{VR} + \frac{v \nabla^2 \xi_\theta}{V^2}$$

In the case of a flow entering a bend from a straight duct, generally  $\xi_r \gg \xi_\theta$ , especially near the side walls. As a consequence, the equation shows that along streamlines curving through the bend, the streamwise development of vorticity is due primarily to deflection of transverse vorticity. Viscous

diffusion of streamwise vorticity, even in turbulent flows, is of secondary importance.

Laminar flow calculations of the experimental configuration have been performed for two entrance flow conditions corresponding to plug flow and parabolic flow profiles. Both QUICK and HYBRID scheme predictions were made. Significant differences between the two schemes are attributed to the larger levels of numerical diffusion in the HYBRID differencing approach. QUICK scheme calculations reveal four types of cross-stream motion which overlap at different locations in the bend: the main cross stream flow, driven by the transverse pressure gradient; a small vortex located at the convex wall, of brief existence, associated with a decrease in the favorable streamwise pressure gradient at this wall in passage through the bend; a larger vortex located on the concave wall, of a persistent nature, associated with the Dean type instability arising in connection with destabilizing curvature effects; a small vortex located in the convex wall corner, of brief existence, driven by the side-wall boundary layer and associated with the phenomenon of stall in turbine cascades. Oscillation of the main flow was predicted numerically by the QUICK scheme and was most intense in the parabolic flow case. Because of the larger net content of transverse vorticity at the inlet plane, the parabolic flow predictions resemble the turbulent flow measurements more than the plug flow case.

The following recommendations are offered for continuing work:

1. Laminar flow measurements should be performed in the bend and downstream tangent to establish definitively the superior performance of QUICK for predicting curved duct flows and for investigating the various vortical structures predicted by this scheme.
2. More detailed turbulent flow measurements are required to understand the relaxation processes taking place in the downstream tangent.

3. Algebraic and/or Reynolds stress models must be advanced in order to predict the strong anisotropic features of 3-D curved duct flows. Since convection of the stress components appears to be important, the algebraic stress closure approach is likely to yield less satisfactory results than a full Reynolds stress closure. Modeling at the stress-equation closure level will certainly be required to predict wall interactions correctly, including curvature effects. The models must be developed so that they apply to the strongly curved ducts of practical interest.

## ACKNOWLEDGEMENTS

Special thanks are due to Professor B.E. Launder for frequent, valuable discussions pertaining to the turbulence model and differencing schemes; to Dr. T. Han for his contributions during the early stages of the development of the numerical procedure; and to Dr. J. Sabnis and Mr. M. Arnal for their assistance with the experimental measurements. This investigation was made possible by the Office of Naval Research through Contract No. N00014-80-C-0031. Additional financial support for the computations was provided by the Technical Coordination Staff of the Office of Fossil Energy of the U.S. Department of Energy, under Contract No. DE-AC03-76SF0098 through the Fossil Energy Materials Program, Oakridge National Laboratory, Oakridge, Tennessee. We are indebted to Mr. K. Ellingsworth of the Office of Naval Research and Mr. A. Levy of the Lawrence Berkeley Laboratory for their unflagging support of our work. We are indebted to Mrs. J. Reed for the typing of this manuscript.

## REFERENCES

1. J.P. Johnston, "Internal Flows," in Turbulence, edited by P. Bradshaw, Topics in Applied Physics, Vol. 12, Springer Verlag, 1978.
2. J.A.C. Humphrey, J.H. Whitelaw and G. Yee, "Turbulent Flow in a Square Duct with Strong Curvature," J. Fluid Mech., 103, 443, 1981.
3. A.M.K.P. Taylor, J.H. Whitelaw and M. Yanneskis, "Curved Ducts with Strong Secondary Motion: Velocity Measurements of Developing Laminar and Turbulent Flow," to appear in J. Fluids Eng., 1982.
4. H.H. Bruun, "An Experimental Investigation of Secondary Flow Losses in Bends with Rectangular Cross Sections," University of Cambridge, Department of Engineering, Report No. CUED/A-Turbo/TR 95, 1979.
5. A. Melling and J.H. Whitelaw, "Turbulent Flow in a Rectangular Duct," J. Fluid Mech., 78, 289, 1976.
6. F.B. Gessner and A.F. Emery, "The Numerical Prediction of Developing Turbulent Flow in Rectangular Ducts," to appear JFE, 1982.
7. R.C. Buggeln, W.R. Briley and H. McDonald, "Computation of Laminar and Turbulent Flow in Curved Ducts, Channels, and Pipes using the Navier-Stokes Equations," Report R80-920006-F, prepared for the Office of Naval Research, December 1980.
8. S.J. Shamroth and H.J. Gibeling, "The Prediction of the Turbulent Flow Field About an Isolated Airfoil," AIAA Paper, 79-1543, 1979.
9. W.D. McNally and P. Sockol, "Computational Methods for Internal Flows with Emphasis on Turbomachinery," NASA-TM-82764, presented at the Symposium on Computers in Flow/reductions and Fluid Dynamics Experiments, at the ASME Winter Annual Meeting, Washington D.C., November 15-20, 1981.
10. V.S. Pratap and D.B. Spalding, "Numerical Computations of the Flow in Curved Ducts," Aero. Quart., 26, 219, 1975.
11. S.M. Chang, T. Han, J.A.C. Humphrey and B.E. Launder, "Prediction of Case 512 for the 1981-82 AFOSR-HTTM-Stanford Conference on Complex Turbulent Flows," to appear in Volume II of the Conference Proceedings, 1982.
12. T. Han, J.A.C. Humphrey and B.E. Launder, "A Comparison of Hybrid and Quadratic-Upstream Differencing in High Reynolds Number Elliptic Flows," Comp. Meth. App. Mech. Eng., 29, 81, 1981.
13. W.R. Briley and H. McDonald, "Analysis and Computation of Viscous Subsonic Primary and Secondary Flows," AIAA Paper No. 79-1453, 4th AIAA-CFD Conference, Williamsburgh, Virginia, 1979.
14. J.P. Kreskovsky, W.R. Briley and H. McDonald, "Prediction of Laminar and Turbulent Primary and Secondary Flows in Strongly Curved Ducts," Report R80-900007-12, prepared for the NASA Lewis Research Center, September 1980.

15. E. Brundrett and W.D. Baines, "The Production and Diffusion of Vorticity in Duct Flow," J. Fluid Mech., 19, 375, 1964.
16. J.H. Perkins, "The Formulation of Streamwise Vorticity in Turbulent Flow," J. Fluid Mech., 44, 721, 1970.
17. D. Naot and W. Rodi, "Numerical Simulation of Secondary Currents in Open Channel Flow with an Algebraic Stress Turbulence Model," SFB 80/T/187, Sonderforschungsbereich 80, Ausbreitungs und Transportvorgänge in Stromungen, Universität Karlsruhe, 1981.
18. G.J. Reece, "A Generalized Reynolds Stress Model of Turbulence," Ph.D. Thesis, University of London, 1976.
19. J.A.C. Humphrey and B.E. Launder, Annual Technical Report submitted to the Office of Naval Research, under Contract No. N00014-80-0031, for project entitled "Turbulent Flow and Heat Transfer in Passage Around 180° Bend - An Experimental and Numerical Study," September 1980.
20. F. Durst, A. Melling and J.H. Whitelaw, "Principles and Practice of laser-Doppler Anemometry," Academic Press, London, 1976.
21. L.E. Drain, "The Laser-Doppler Technique," John Wiley and Sons Ltd., New York, 1980.
22. P. Buchhave, "The Measurement of Turbulence with the Burst-Type Laser Doppler Anemometer - Errors and Correction Methods," Ph.D. Thesis, State University of New York at Buffalo, 1979.
23. A. Melling, "Investigation of Flow in Non-Circular Ducts and Other Configurations by laser-Doppler Anemometry," Ph.D. Thesis, University of London, 1975.
24. J.A.C. Humphrey, "Flows in Ducts with Curvature and Roughness," Ph.D. Thesis, University of London, 1977.
25. K. Hanjalic, "Two-Dimensional Asymmetric Flow in Ducts," Ph.D. Thesis, University of London, 1970.
26. V.S. Pratap, "Flow and Heat Transfer in Curved Ducts," Ph.D. Thesis, University of London, 1975.
27. B.P. Leonard, "A Stable and Accurate Convective Modeling Procedure Based on Quadratic Upstream Interpolation," Comput. Meths. Appl. Mech. Engrg., 19, 59, 1979.
28. S.M. Chang, "Measurement and Calculation of Developing Turbulent Flow in a U-Bend and Downstream Tangent of Square Cross-Section," Ph.D. Thesis, University of California, Berkeley, to appear in 1983.
29. S.V. Patankar and D.B. Spalding, "A Calculation Procedure for Heat, Mass and Momentum Transfer in Three-Dimensional Parabolic Flows," Int. J. Heat Mass Transfer, 15, 1787, 1972.



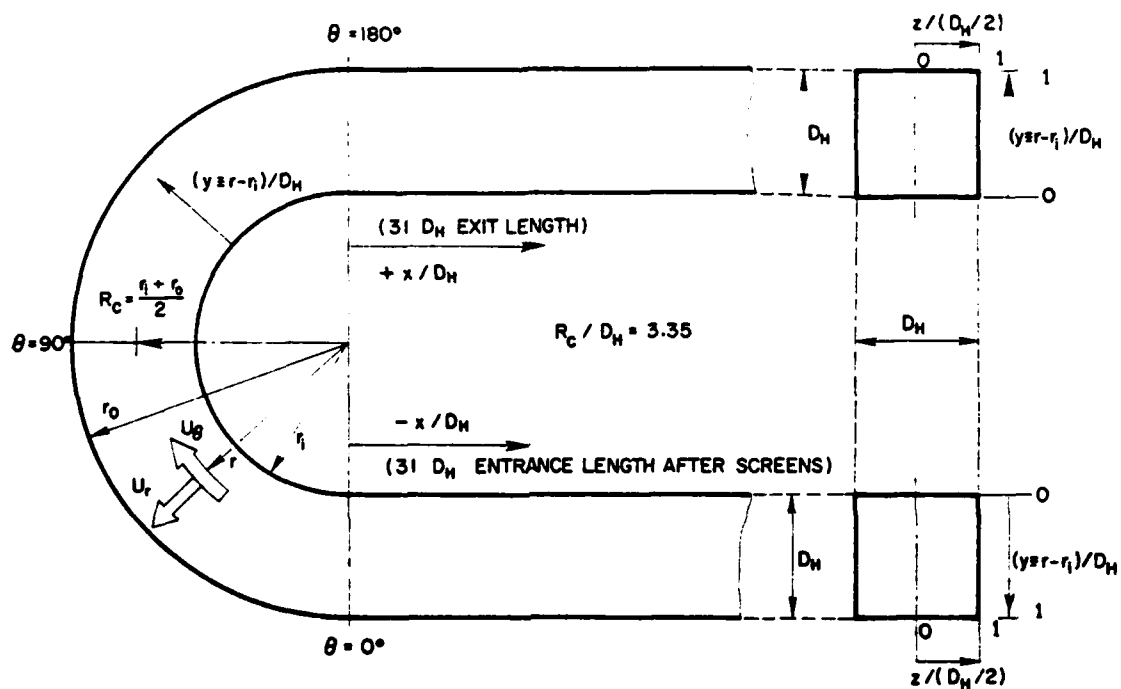
30. F.B. Gessner, J.K. Po and A.F. Emery, "Measurements of Developing Turbulent Flow in a Straight Duct," Turbulent Shear Flows I, Springer Verlag, Berlin. Editors: F. Durst, B.E. Launder, F.W. Schmidt and J.H. Whitelaw, 1979.
31. S. Eskinazi and H. Yeh, "An Investigation on Fully Developed Turbulent Flows in a Curved Channel," J. Aero. Sci., 23, 23, 1956.
32. W.R. Hawthorne, "Secondary Circulation in Fluid Flow," Proc. Roy. Soc. London ser. A. 206, 374, 1951.
33. J.H. Horlock and B. Lakshminarayana, "Secondary Flows: Theory, Experiment, and Application in Turbomachinery Aerodynamics," Ann. Rev. Fluid Mech., 5, 247, 1973.
34. H.B. Squire and K.G. Winter, "The Secondary Flow in a Cascade of Airfoils in a Non-uniform Stream," J. Aeronaut. Sci., 18, 271, 1951.
35. D. Bryant and J.A.C. Humphrey, "Conservation Equations for Laminar and Turbulent Flows in General Three-Dimensional Curvilinear Coordinates," Imperial College of Science and Technology, London, Report No. CHT-76-6, 1976.
36. W.R. Dean, "Fluid Motion in a Curved Channel," Proc. Roy. Soc. London, ser. A, 121, 402, 1928.
37. K.C. Cheng, J. Nakayama, and M. Akiyama, "Effect of Finite and Infinite Aspect Ratios on Flow Patterns in Curved Rectangular Channels," Flow Visualization, edited by T. Asanuma, McGraw-Hill, 1979.
38. K.N. Ghia and J.S. Sokhey, "Laminar Incompressible Viscous Flows in Curved Ducts of Regular Cross-Sections," J. Fluid Engineering, 99, 640, 1977.
39. K.C. Cheng, R-C. Lin, and J-W. Ou, "Graetz Problem in Curved Rectangular Channels with Convective Boundary Condition - The Effect of Secondary Flow on Liquid Solidification-Free Zone," Int. J. Heat Mass Transfer, 18, 996, 1975.
40. B. Joseph, E.P. Smith and R.J. Adler, "Numerical Treatment of Laminar Flow in Helically Coiled Tubes of Square Cross-Section," AIChE J., 21, No. 5, 965, 1975.

Quantity	Range of Maximum Systematic Error + (deviation %)	Maximum Random Error ++ (r.m.s. %)
$U_{\theta}/U_B$	- 1% to 2%	$\pm 2\%$
$U_r/U_B$	- 1% to 2%	$\pm 2\%$ to $\pm 3\%$
$\tilde{u}_{\theta}/U_B$	- 2% to 2%	$\pm 2\%$ to $\pm 3\%$
$\tilde{u}_r/U_B$	- 2% to 2%	$\pm 2\%$ to $\pm 4\%$
$\overline{u_{\theta}u_r}/U_B^2$	- 2% to 2%	$\pm 3\%$ to $\pm 7\%$

+ Error confined mainly to near wall flow regions; does not include angular uncertainty discussed in text.

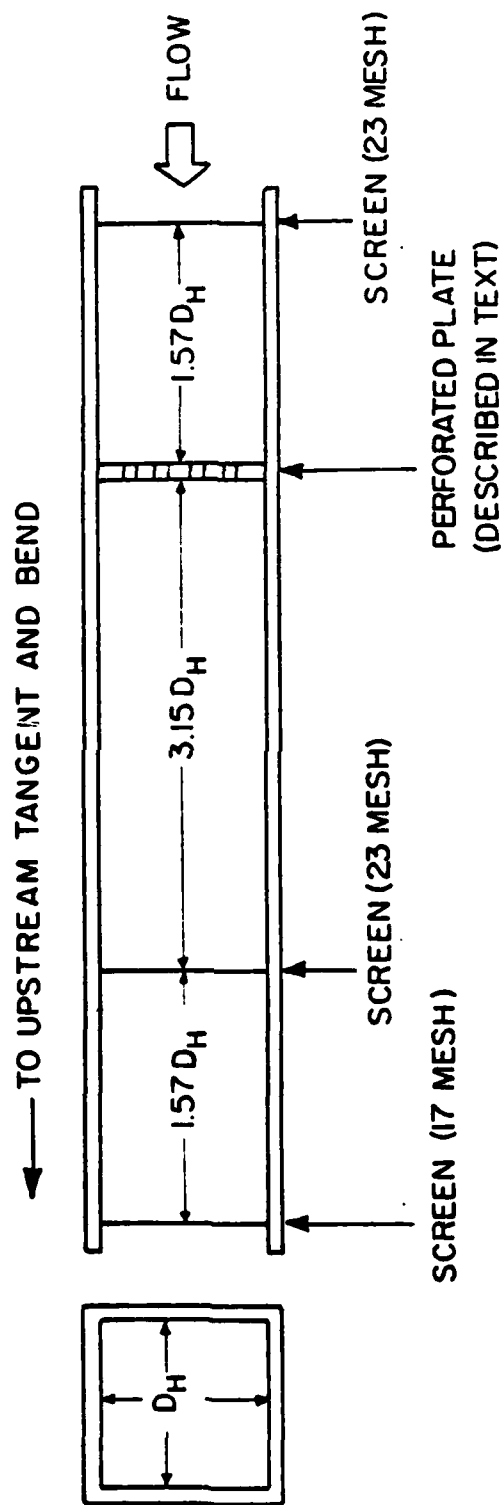
++ Largest errors confined to small flow regions; does not include a small positioning uncertainty of probe volume in the flow.

Table 1: Tabulation of Estimated Maximum Measurement Errors



XBL 8210-2772

Figure 1 Schematic showing test section dimensions, coordinate system and velocity components of the flow.



XBL 8210-2771

Figure 2 Optimum experimental arrangement of stainless steel screens and perforated plate in the flow-uniformizing section preceding the upstream tangent.

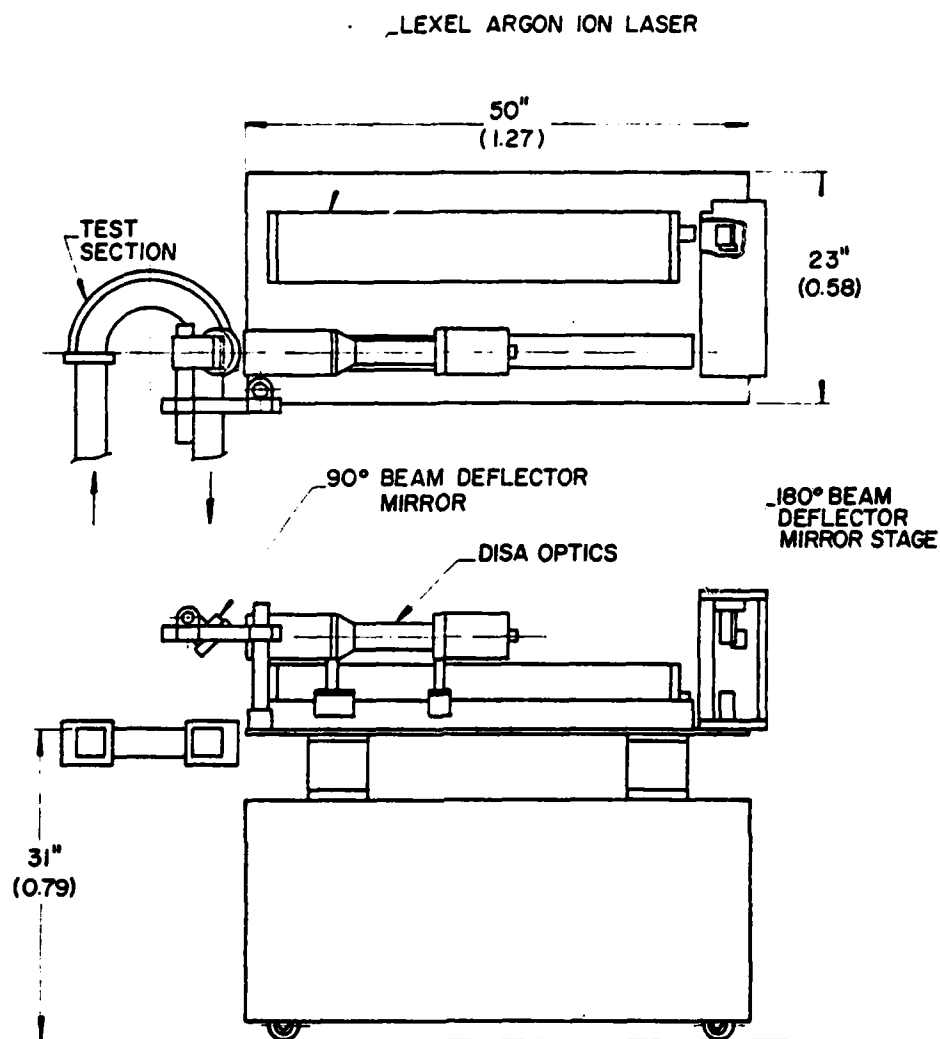
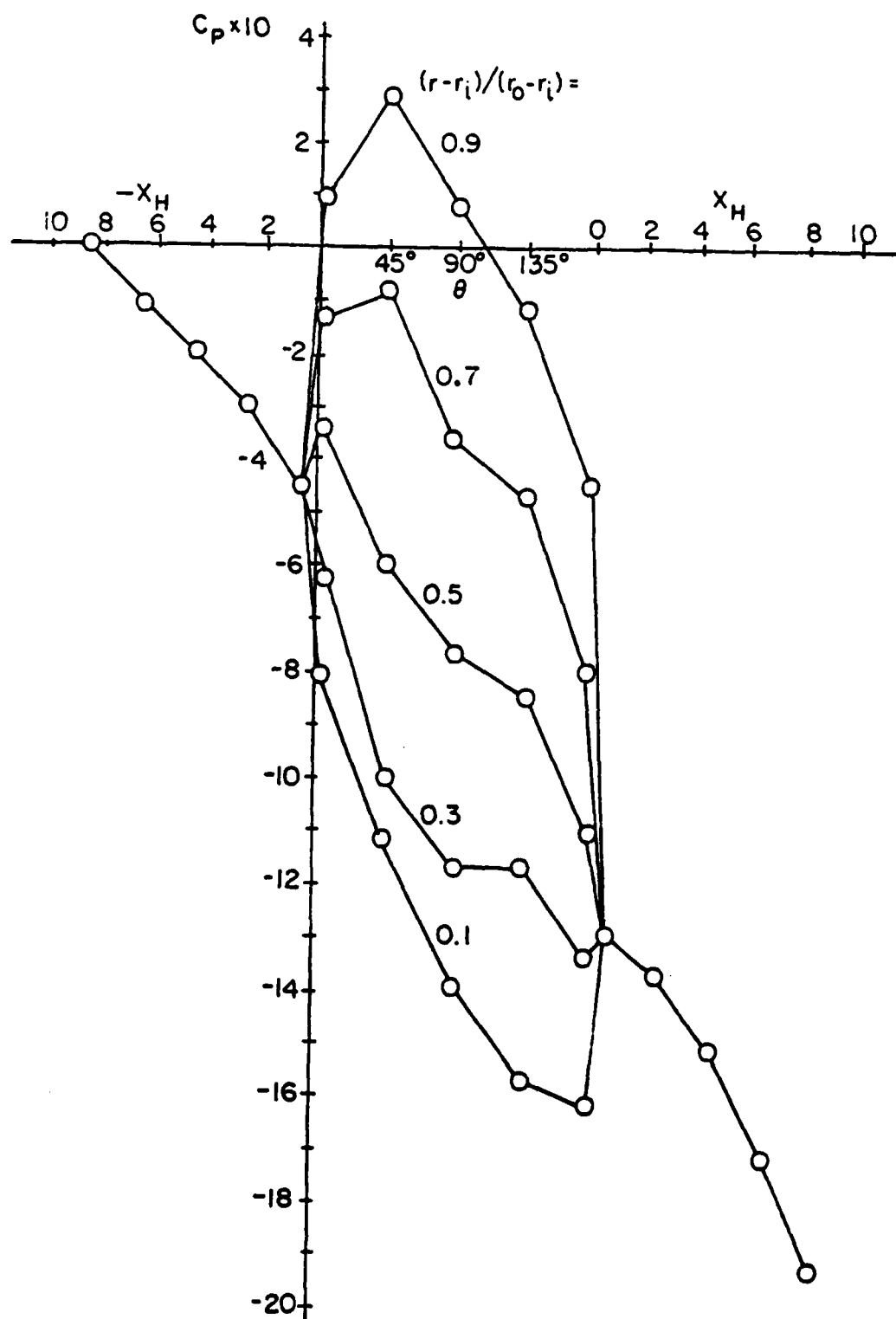


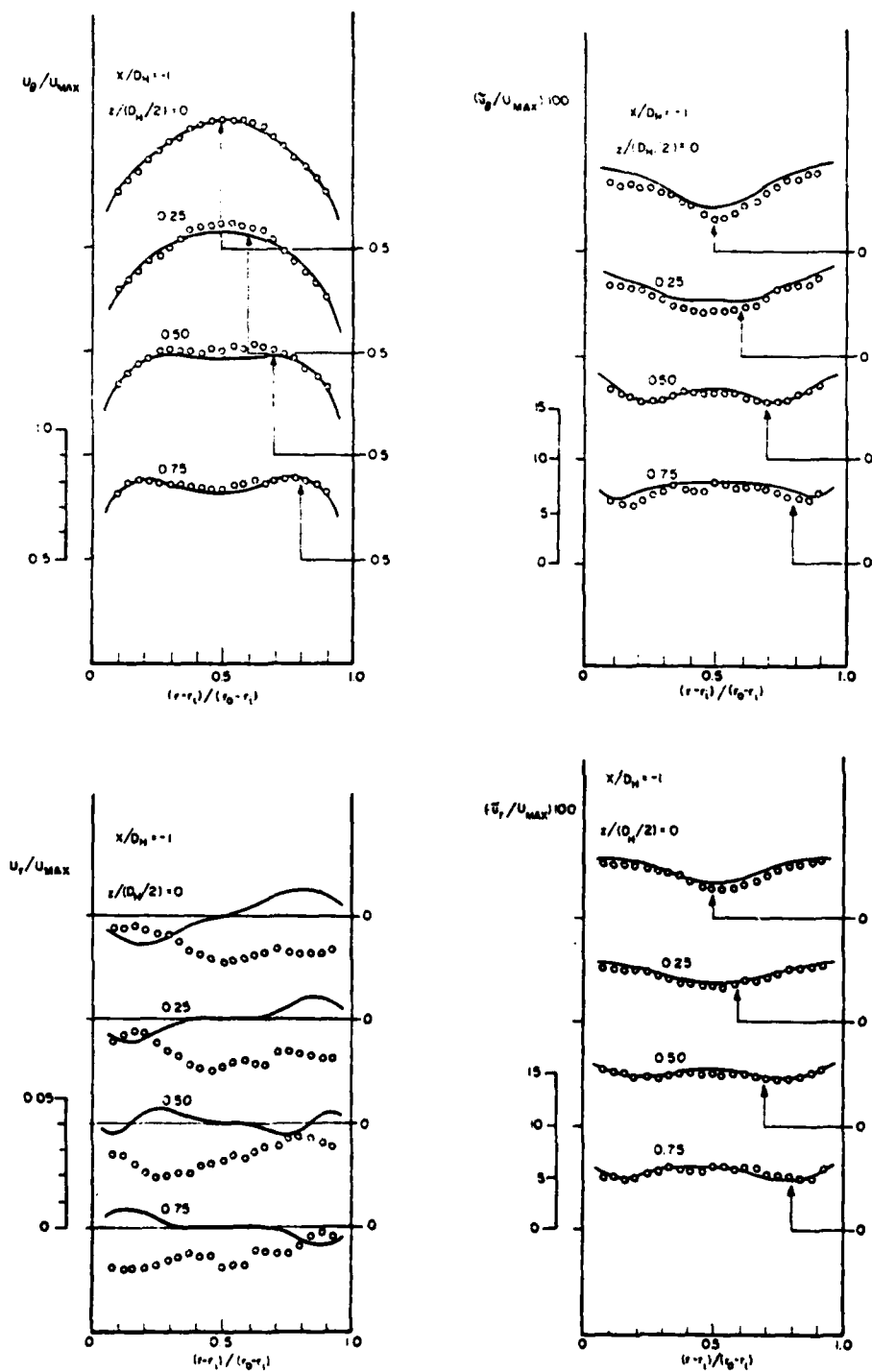
Figure 3 Top and side view of laser-Doppler velocimeter aligned for measurements at a bend angle  $\theta = 180^\circ$ . Traversing mechanism details are not shown.

XBL 8210-2779



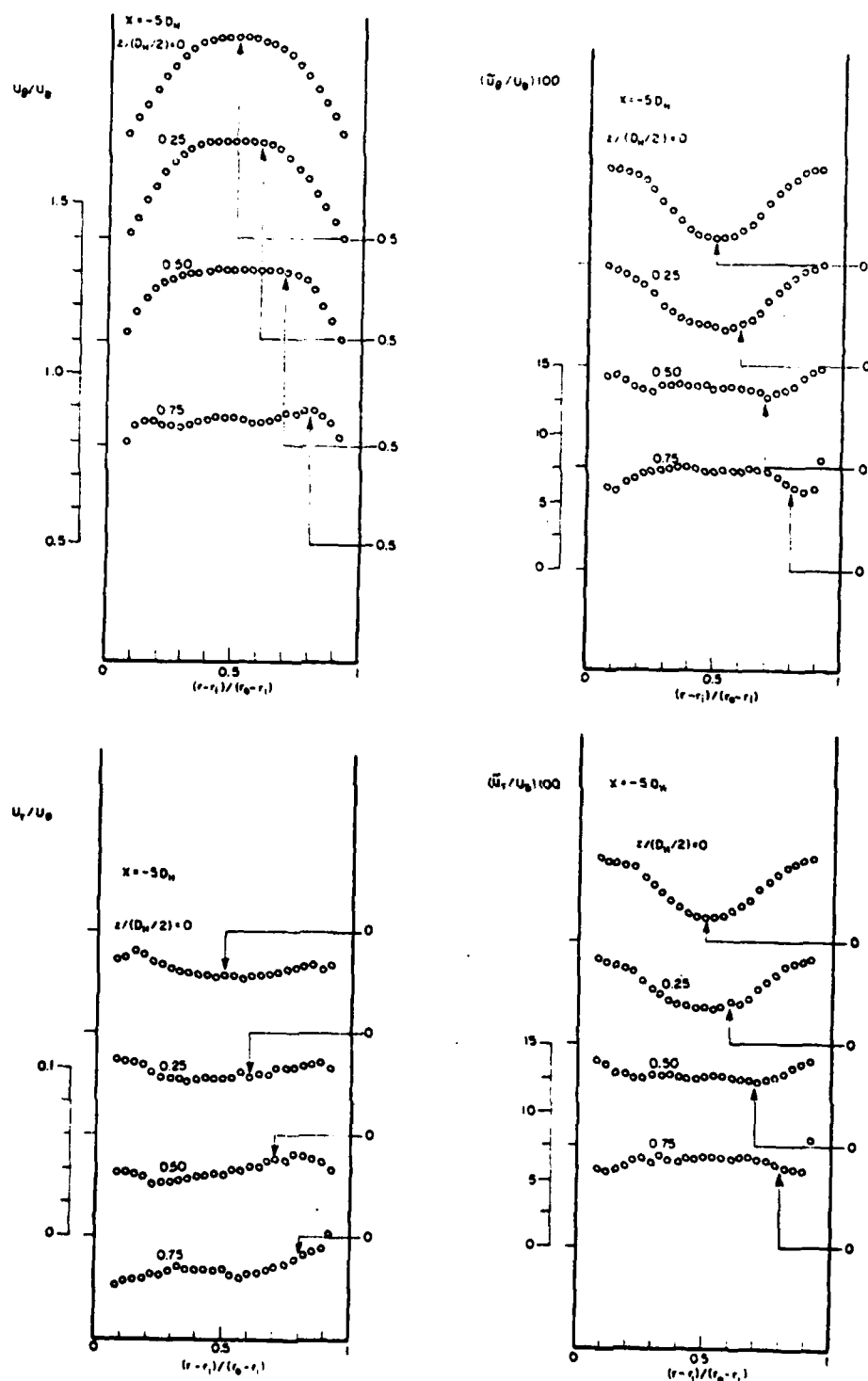
XBL S210-2770

Figure 4 Distribution of pressure coefficient ( $C_p = \Delta P / \rho U_B^2$ ) in the bend and tangents for conditions of the experiment:  $Re = 64,000$ ,  $R_c/D_H = 3.35$  and  $De = 24,000$ . Measurements made through pressure taps on side walls of test section components.



XBL 8210-2803

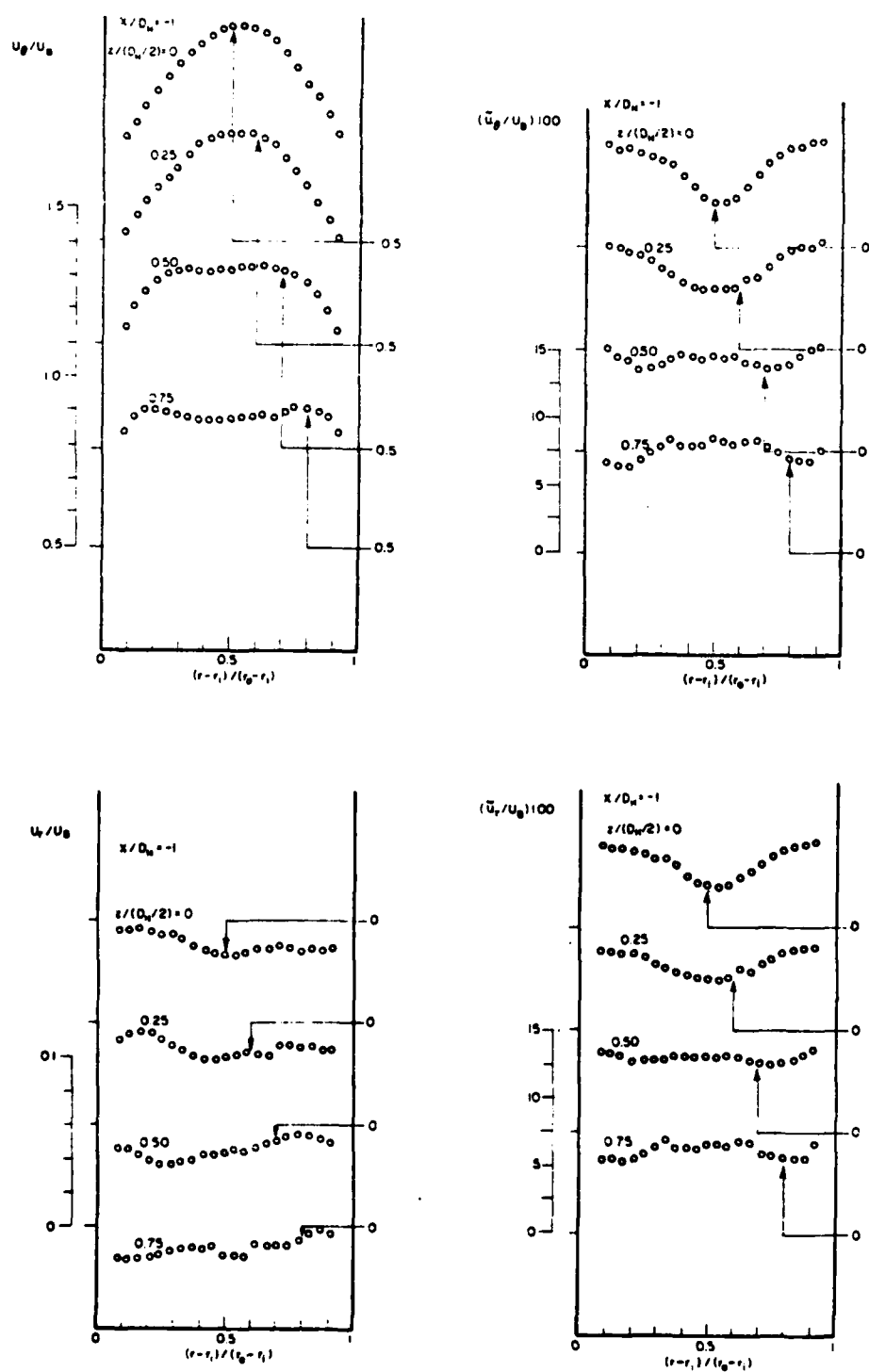
Figure 5 Comparison between turbulent flow measurements of mean velocity and normal stress from this work (o) at  $X_H = -1$  and measurements by Melling and Whitelaw (—) after a development length of  $36.8 D_H$ .



XBL 8210-2798

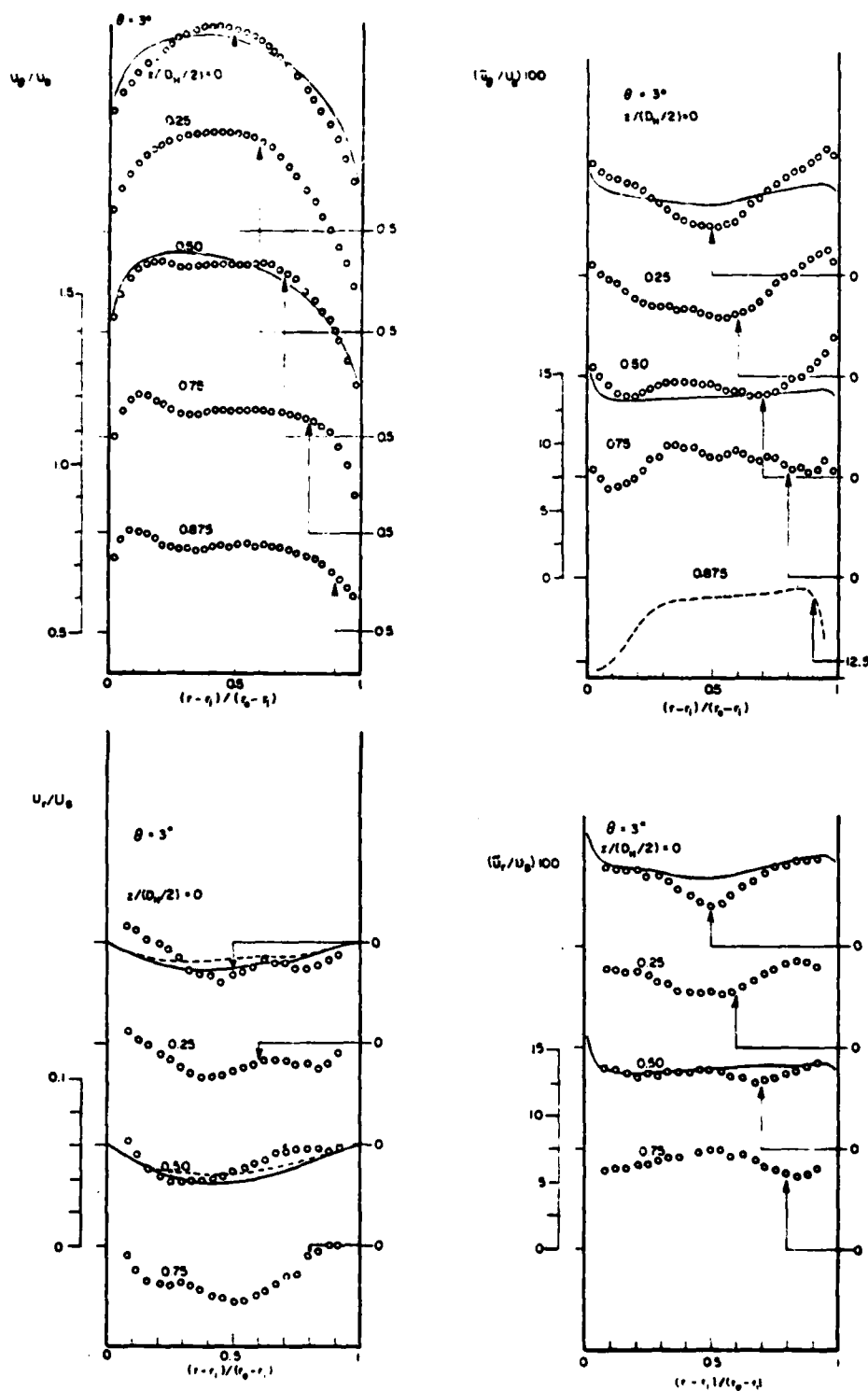
Figure 6 Turbulent flow measurements of mean velocity and normal stress in the upstream tangent at  $X_H = -5$ .





XBL 8210-2774

Figure 7 Turbulent flow measurements of mean velocity and normal stress in the upstream tangent at  $X_H = -1$ .



XBL 8210-2775

Figure 8 Turbulent flow measurements and calculations of mean velocity and normal stress in the bend at  $\theta = 3^\circ$ : (—) HYBRID, (---) QUICK; dashed line at 0.875 is best fit to measurements.

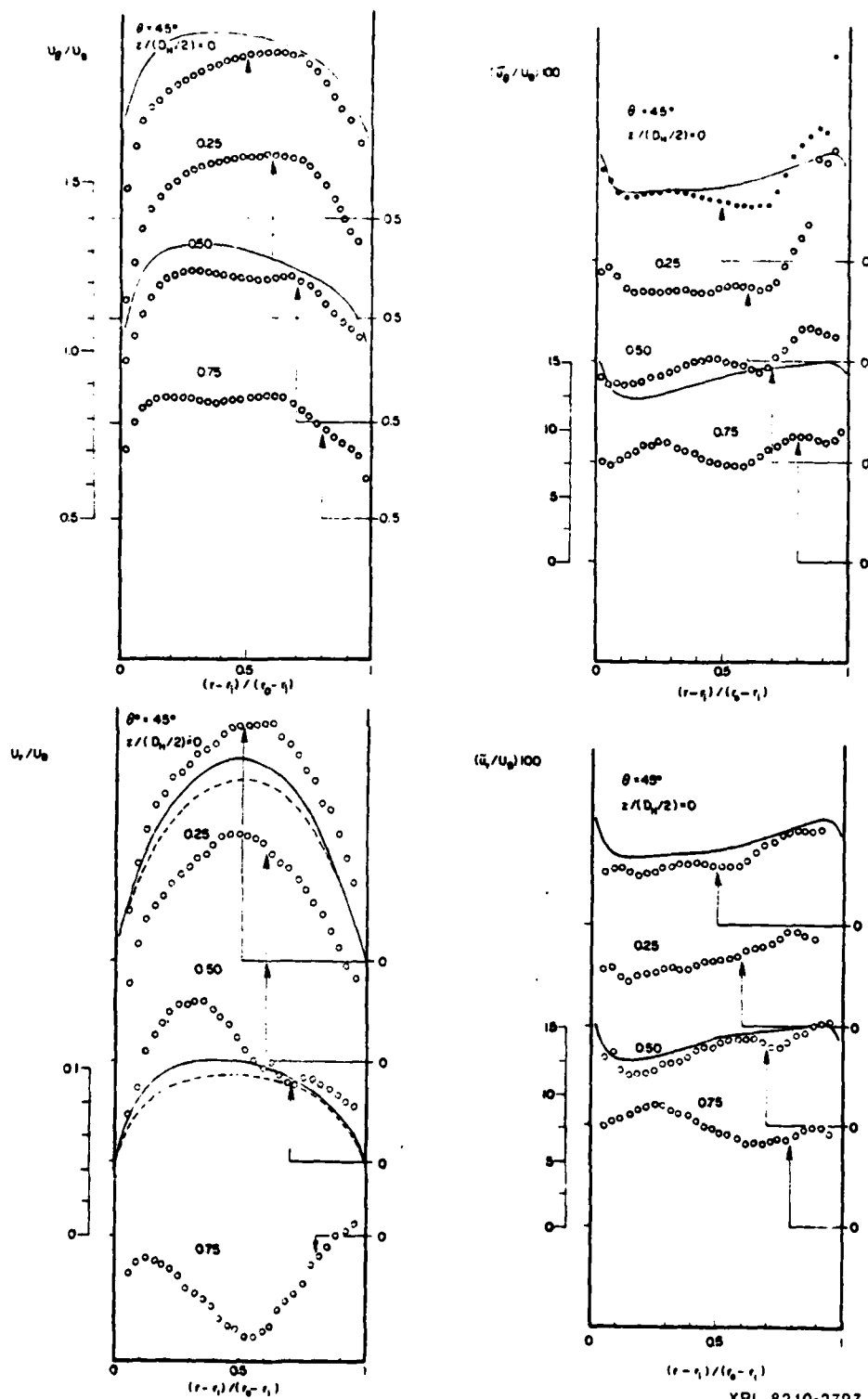


Figure 9 Turbulent flow measurements and calculations of mean velocity and normal stress in the bend at  $\theta = 45^\circ$ : (—)HYBRID, (---) QUICK.

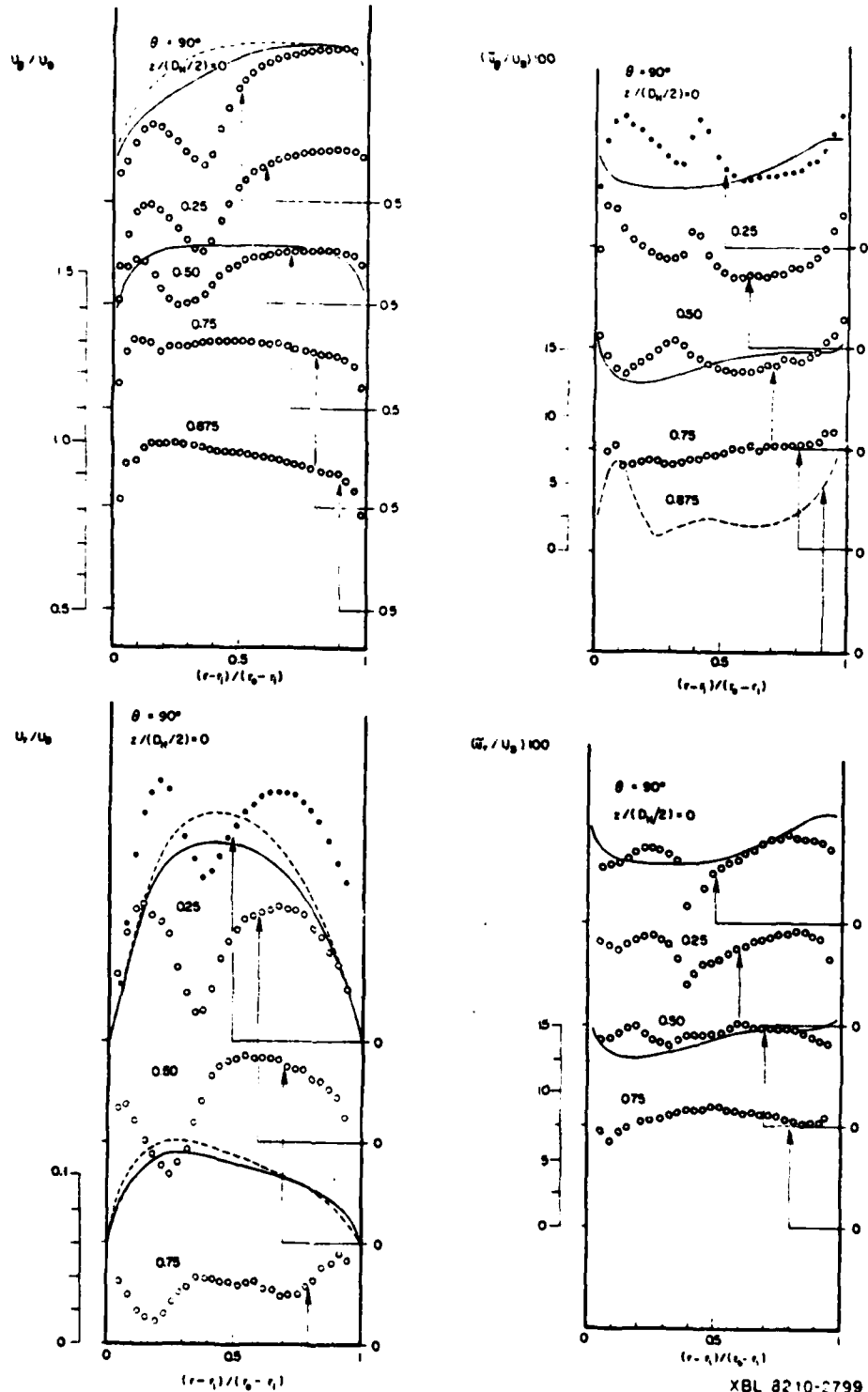
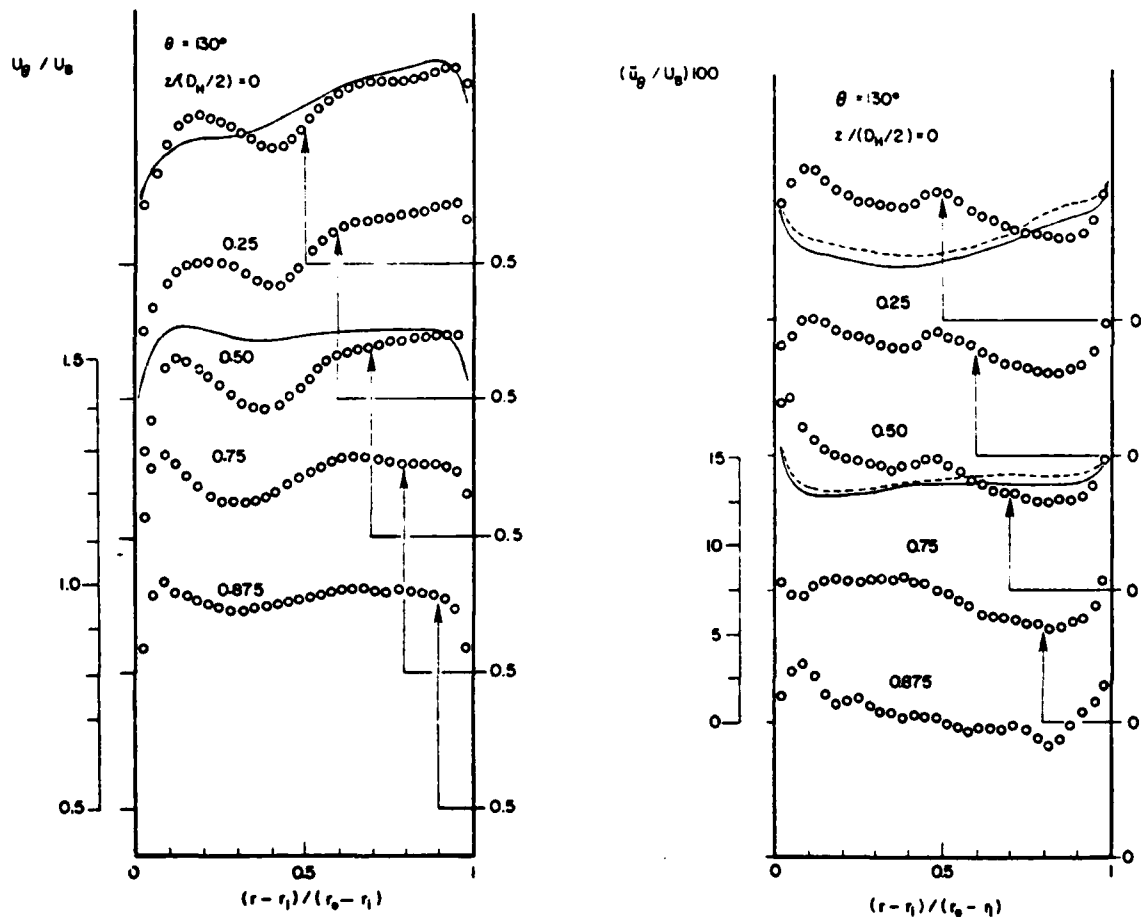
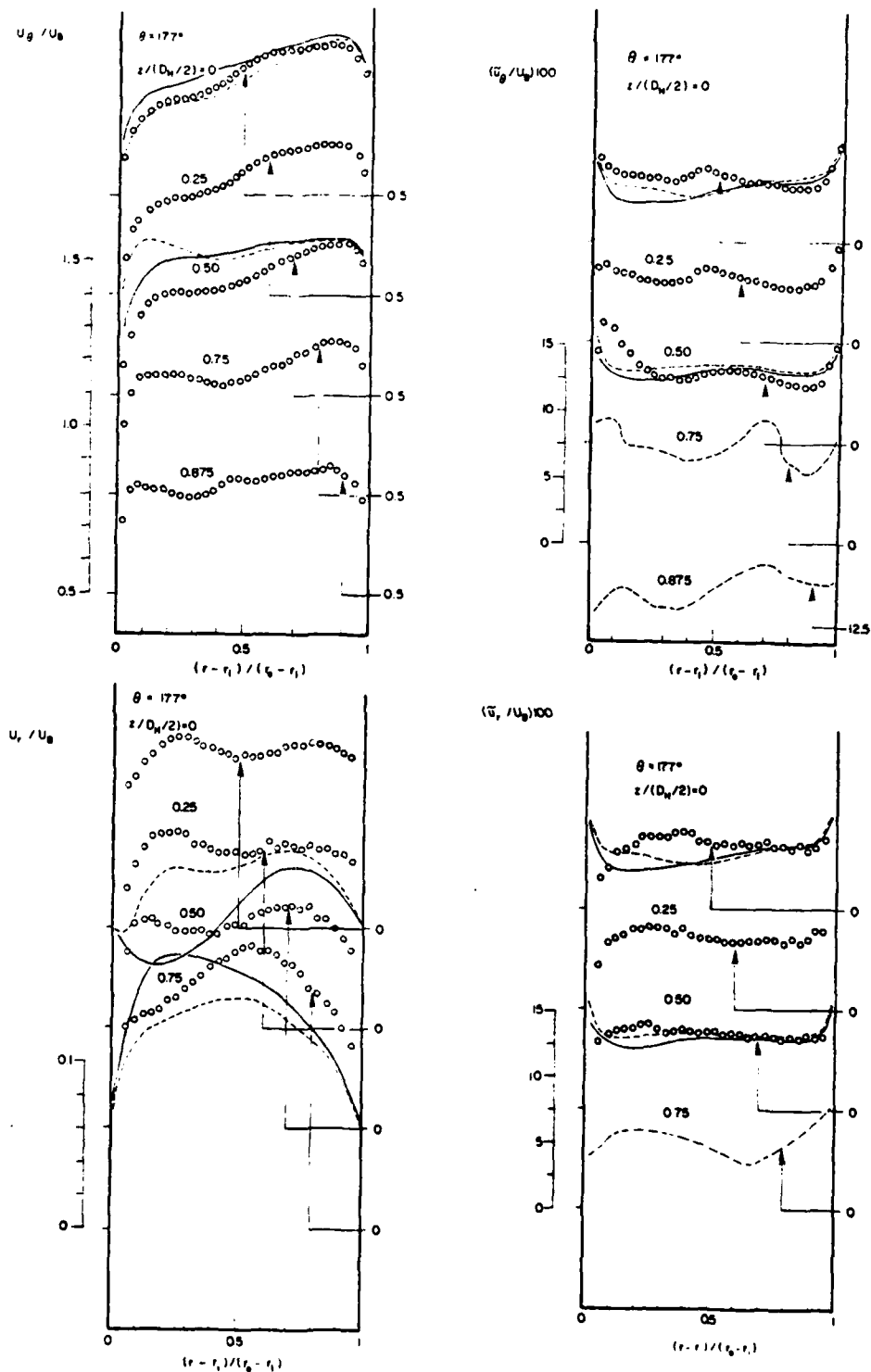


Figure 10 Turbulent flow measurements and calculations of mean velocity and normal stress in the bend at  $\theta = 90^\circ$ : (—)HYBRID, (---) QUICK; dashed line at 0.875 is best fit to measurements.



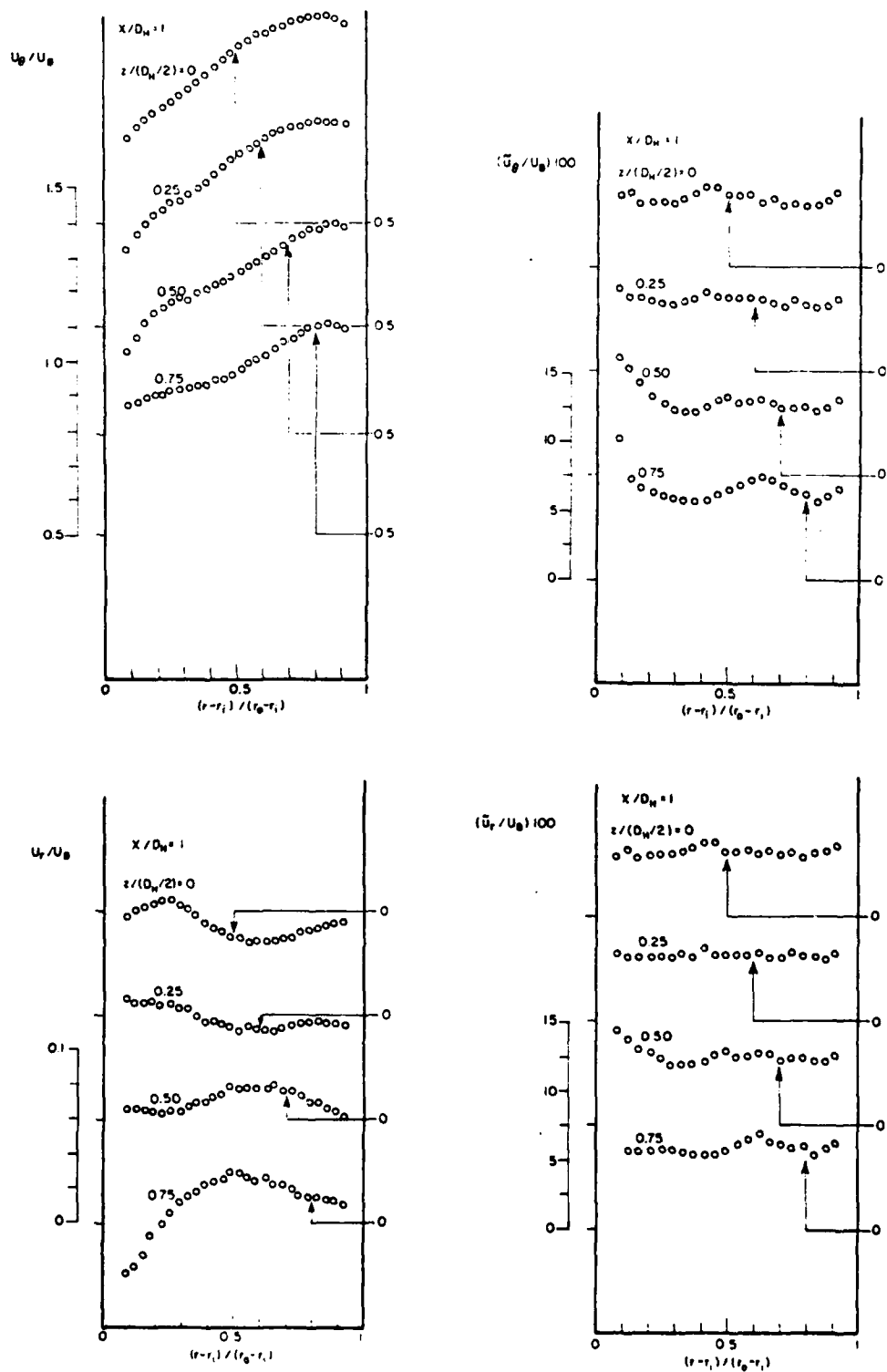
XBL 6210-2796

Figure 11 Turbulent flow measurements and calculations of mean velocity and normal stress in the bend at  $\theta = 130^\circ$ : (—) HYBRID, (---) QUICK.



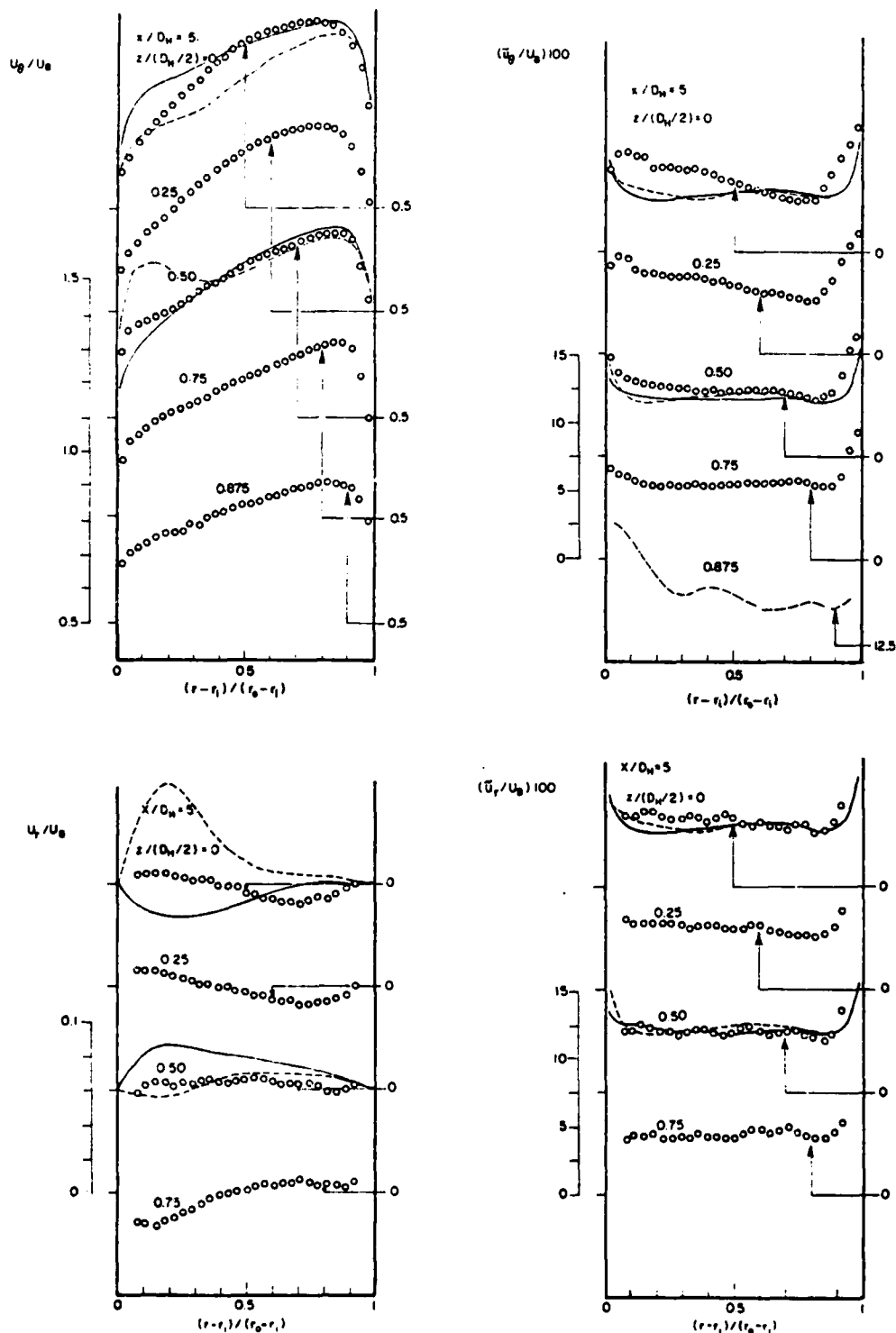
XBL 8210-2802

Figure 12 Turbulent flow measurements and calculations of mean velocity and normal stress in the bend at  $\theta = 177^\circ$ : (—) HYBRID, (---) QUICK; dashed lines at 0.75 and 0.875 are best fits to measurements.



XBL 8210-2778

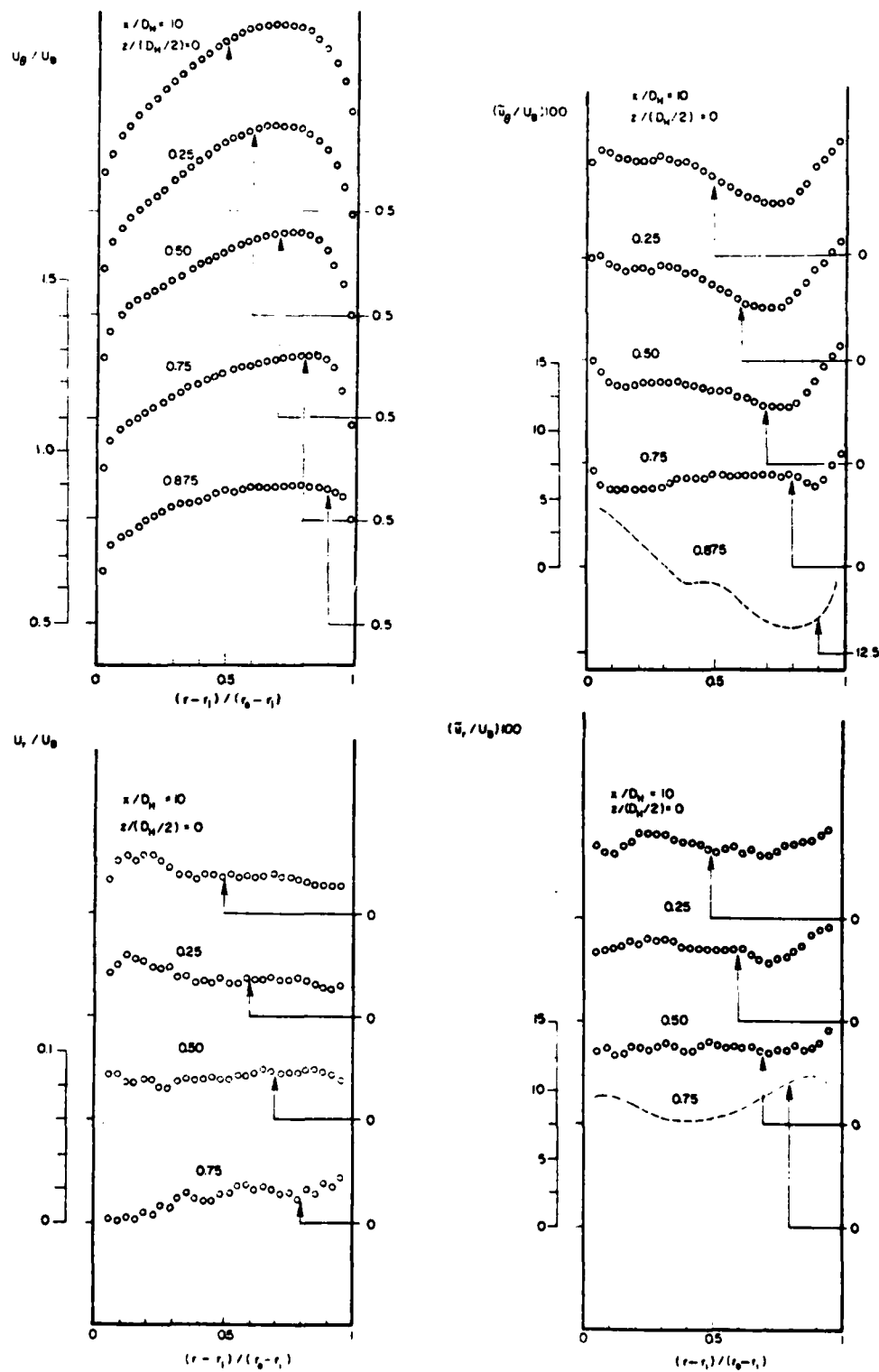
Figure 13 Turbulent flow measurements of mean velocity and normal stress in the downstream tangent at  $X_H = 1$ .



XBL 8210-2777

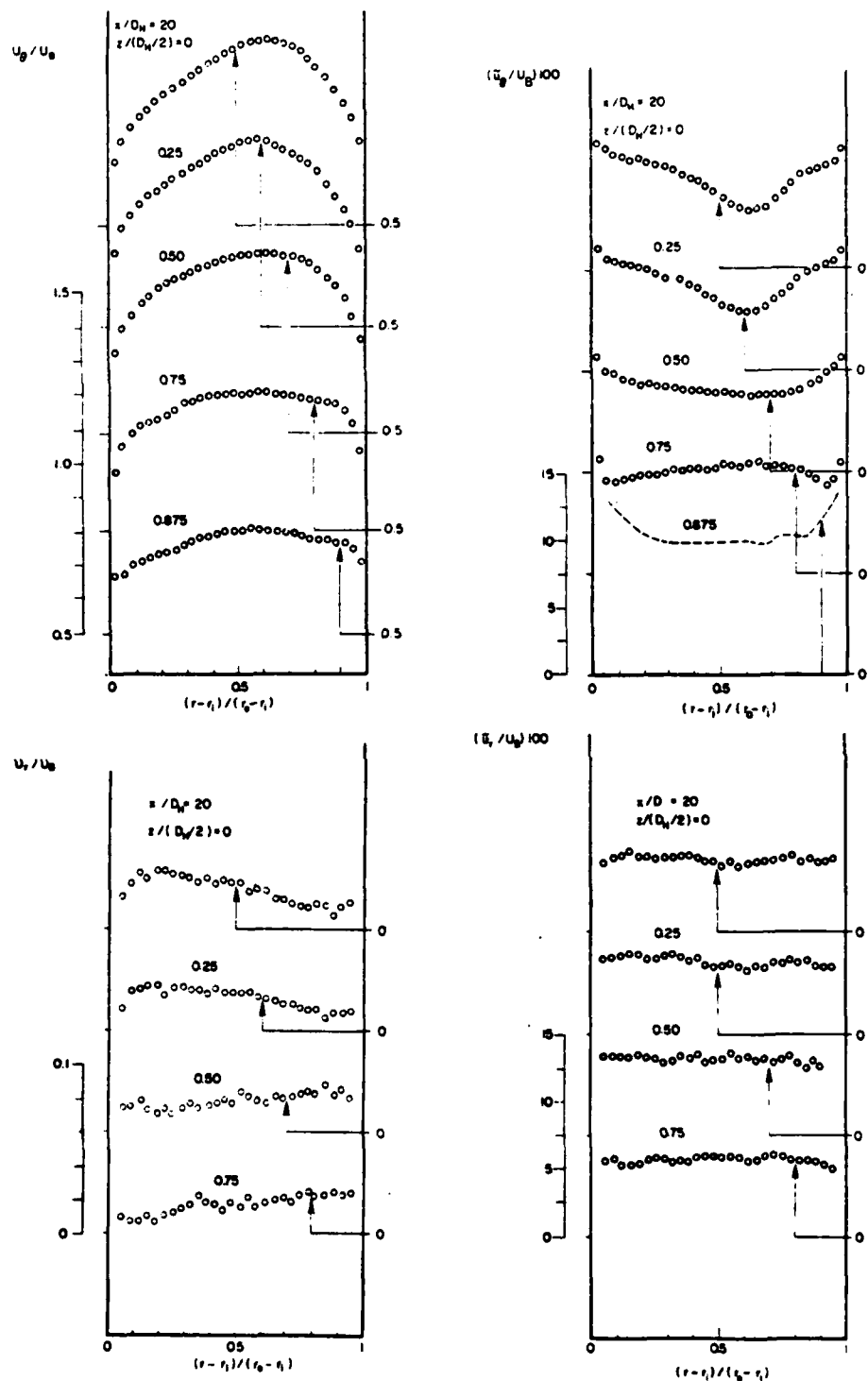
Figure 14 Turbulent flow measurements and calculations of mean velocity and normal stress in the downstream tangent at  $X_H = 5$ : (—) HYBRID, (---) QUICK; dashed line at 0.875 is best fit to measurements.





XBL 8210-2776

Figure 15 Turbulent flow measurements of mean velocity and normal stress in the downstream tangent at  $X_H = 10$ ; dashed lines at 0.75 and 0.875 are best fits to measurements.



XBL 8210-2804

Figure 16 Turbulent flow measurements of mean velocity and normal stress in the downstream tangent at  $X_H = 20$ ; dashed line at 0.875 is best fit to measurements.

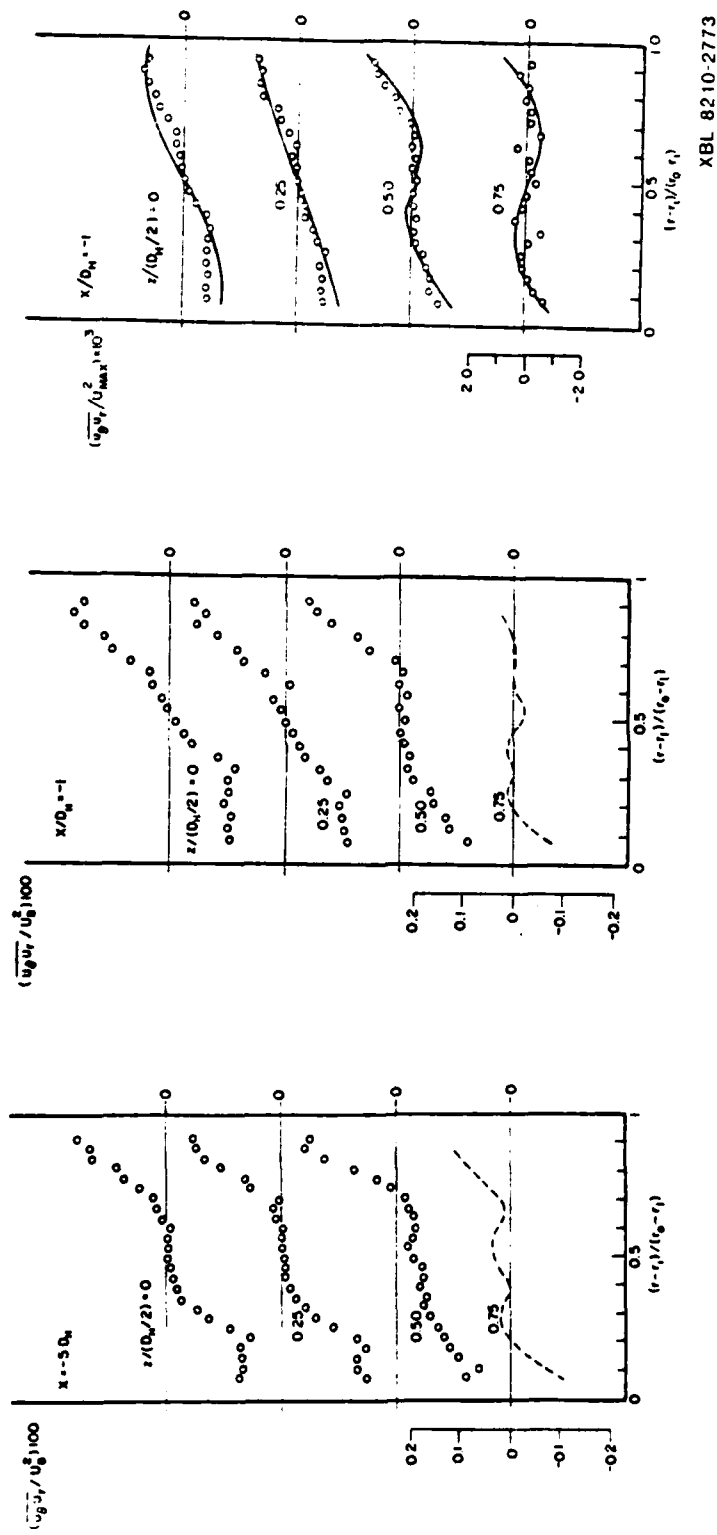
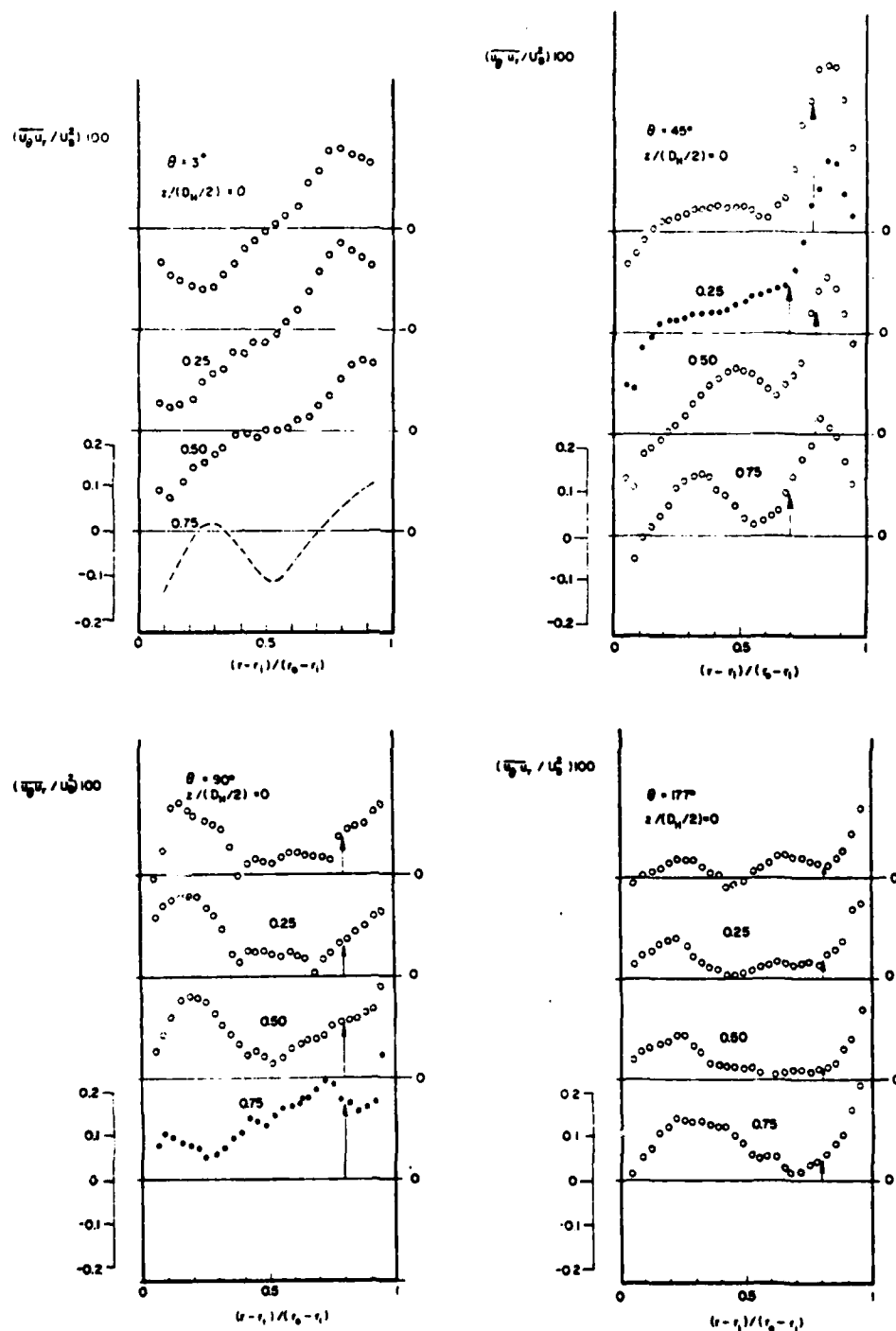
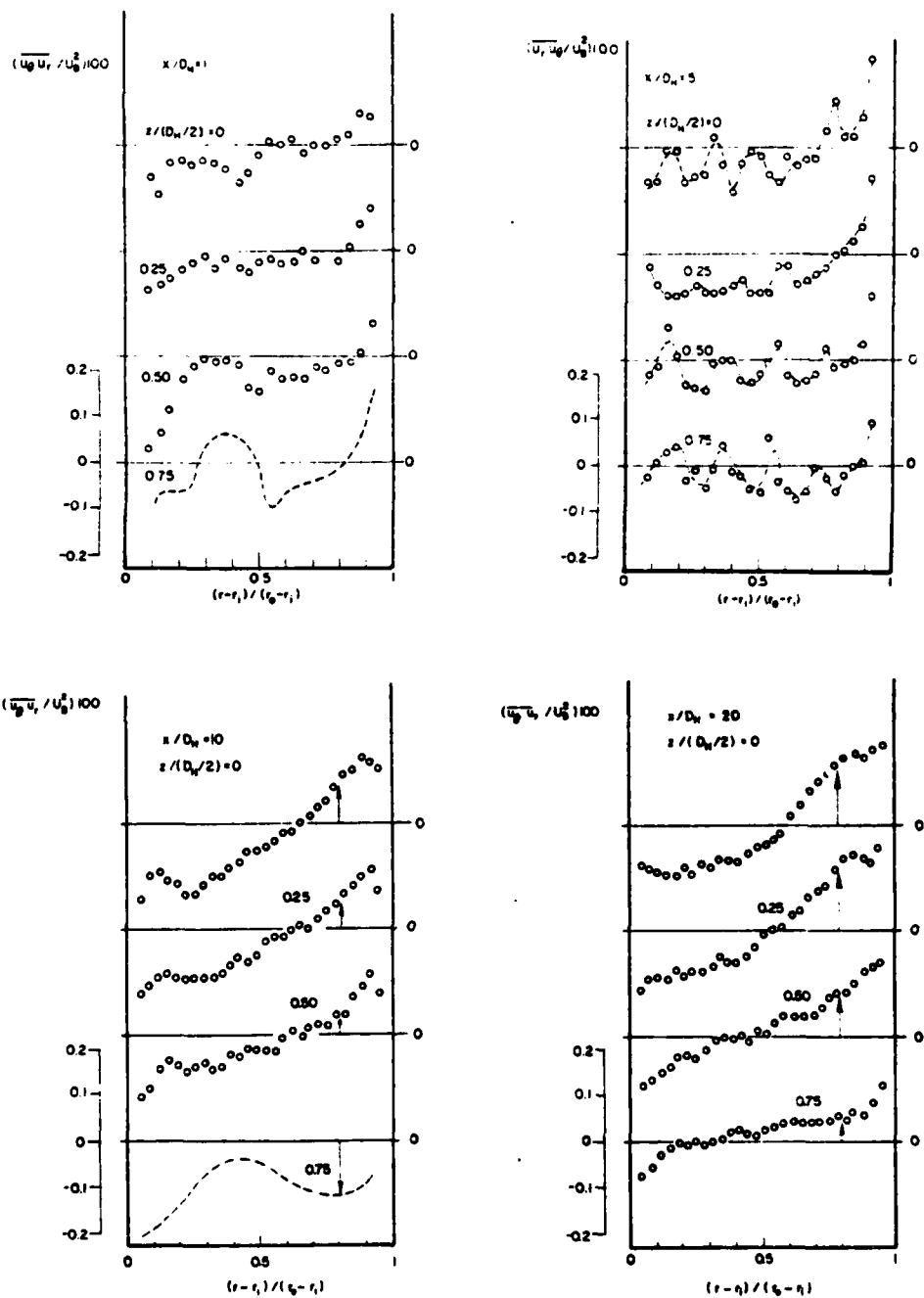


Figure 17 Turbulent flow measurements of shear stress at  $X_H = -5$  and  $-1$   
 (o) data from this work; (---) data from Melling and Whitelaw;  
 dashed lines at 0.75 are best fit to data.



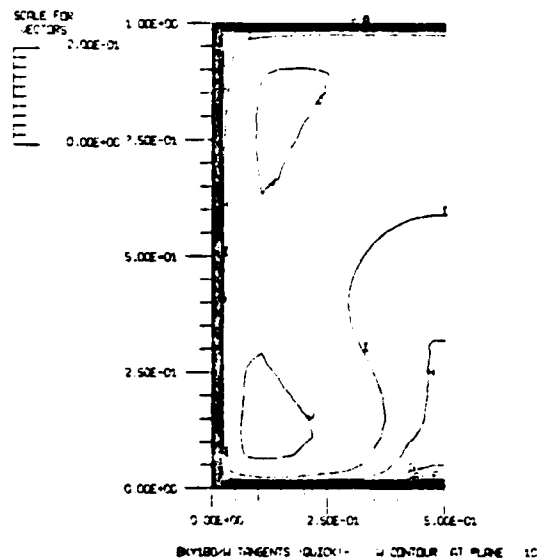
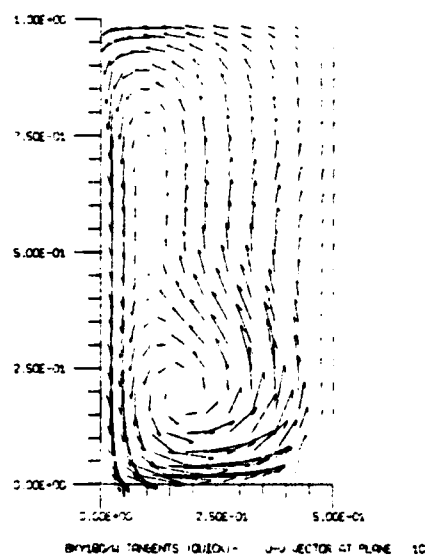
XBL 8210-2801

Figure 18 Turbulent flow measurements of shear stress at four longitudinal stations in the bend; dashed line at 0.75 is best fit to measurements.



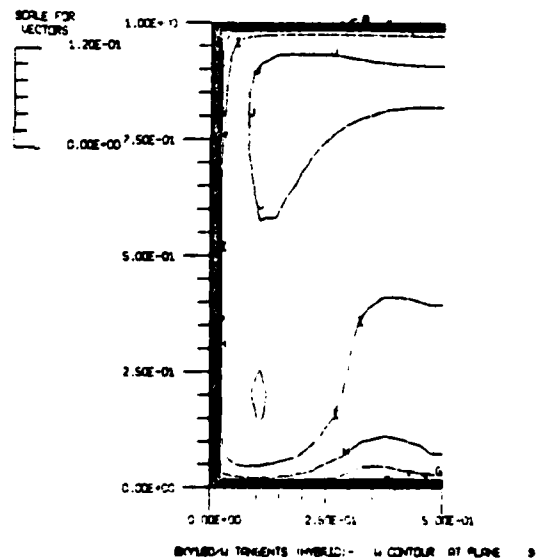
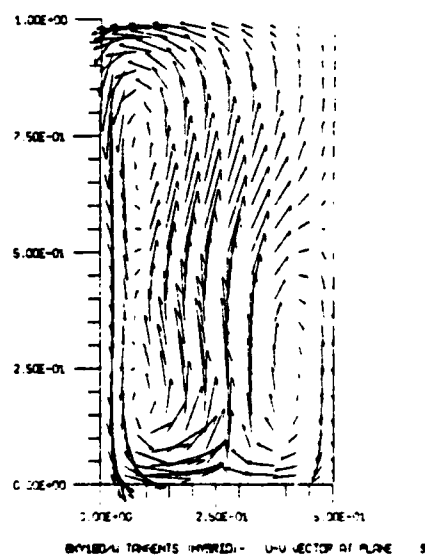
XBL 8210-2800

Figure 19 Turbulent flow measurements of shear stress at four longitudinal stations in the downstream tangent; dashed lines are best fits to measurements.



CONTOUR LEVELS

1	0.00E+00
2	0.10E+01
3	0.20E+01
4	0.30E+01
5	0.40E+01
6	0.50E+01
7	0.60E+01
8	0.70E+01
9	0.80E+01
10	0.90E+01
11	1.00E+01



CONTOUR LEVELS

1	0.00E+00
2	0.10E+01
3	0.20E+01
4	0.30E+01
5	0.40E+01
6	0.50E+01
7	0.60E+01
8	0.70E+01
9	0.80E+01
10	0.90E+01
11	1.00E+01

REL 0010-4707

Figure 20 Turbulent flow predictions of cross-stream and streamwise velocities at  $\theta = 177^\circ$ : velocity components are normalized by  $U_B$ ; outer radius (concave) wall is shown at the top of each plot.

## APPENDIX I

### QUICK SCHEME FORMULATION FOR TRANSPORT VARIABLES

This appendix contains a brief account of the formulation of the QUICK scheme as well as its incorporation into TEACH-type codes. It is illustrated via a simple 1-D problem. The appropriate 2-D counterparts are summarized in table A-1. Details of the scheme formulation can be found in, for example, [27,28] and of its testing in [12].

As an example, consider the simplified convection-diffusion equation

$$\frac{\partial}{\partial x} (\rho U \phi) - \frac{\partial}{\partial x} \left( \gamma \frac{\partial \phi}{\partial x} \right) = 0 \quad (\text{A.1})$$

Following the standard control volume approach of TEACH-type codes [29], equation (A.1) is integrated over its cell, shown in Figure A.1. Using central differencing for the diffusion terms, equation (A.1), with all the subscripts and dimensions referred to Figure A.1, becomes

$$C_e \phi_e - C_w \phi_w - D_e (\phi_E - \phi_P) + D_w (\phi_P - \phi_W) = 0 \quad (\text{A.2})$$

where

$$C_e \equiv (\rho U)_e$$

$$C_w \equiv (\rho U)_w$$

$$D_e \equiv \gamma_e / \delta X_i$$

and

$$D_w \equiv \gamma_w / \delta X_{i-1}$$

For the convection terms  $C_e \phi_e$  and  $C_w \phi_w$ , Leonard [27] proposed a quadratic upwind interpolation scheme (QUICK) to approximate  $\phi_e$  and  $\phi_w$  at the surfaces of the control cell. The proper formulae for the east surface are:



$$\phi_e = \frac{1}{2}(\phi_E + \phi_P) - \frac{(\delta_i)^2}{8} \left( \frac{\phi_{EE} - \phi_E}{\delta_{i+1}} - \frac{\phi_E - \phi_P}{\delta_i} \right) / \Delta_{i+1}, \quad \text{if } C_e < 0$$

or

(A.3)

$$\phi_e = \frac{1}{2}(\phi_E + \phi_P) - \frac{(\delta_i)^2}{8} \left( \frac{\phi_E - \phi_P}{\delta_i} - \frac{\phi_P - \phi_W}{\delta_{i-1}} \right) / \Delta_i, \quad \text{if } C_e > 0.$$

To facilitate the incorporation of QUICK into equation (A.2), equations (A.3) are written in the compact form:

$$\phi_e = \frac{1}{2}(\phi_E + \phi_P) + \alpha_e \phi_P + \beta_e \quad (\text{A.4})$$

$$\text{where } \alpha_e = \begin{cases} \delta_i(1 + \delta_i/\delta_{i-1})/8\Delta_i & \text{if } C_e > 0 \\ -\delta_i/8\Delta_{i-1} & \text{if } C_e < 0 \end{cases}$$

$$\text{and } \beta_e = \begin{cases} -(\delta_i)^2(\phi_E/\delta_i + \phi_W/\delta_{i-1})/8\Delta_i & \text{if } C_e > 0 \\ -(\delta_i)^2(\phi_{EE} - \phi_E)/\delta_{i+1} - \phi_E/\delta_i)/8\Delta_{i+1} & \text{if } C_e < 0 \end{cases}.$$

Similarly we write

$$\phi_w = \frac{1}{2}(\phi_P + \phi_W) + \alpha_w \phi_P + \beta_w \quad (\text{A.5})$$

Substituting equations (A.4) and (A.5) into equation (A.2) and rearranging yields:

$$\begin{aligned}
 \phi_p \{ D_e + \frac{1}{2} C_e + D_w - \frac{1}{2} C_w - (\alpha_w C_w - \alpha_e C_e) \} &= \phi_E \{ D_e - \frac{1}{2} C_e \} \\
 &+ \phi_W \{ D_w + \frac{1}{2} C_w \} + (\beta_w C_w - \beta_e C_e)
 \end{aligned}
 \tag{A.6}$$

Finally, adding the continuity relation  $C_w - C_e = 0$  multiplied by  $\phi_p$  to both sides of equation (A.6), yields:

$$\{ A_E + A_W - S_p \} \phi_p = A_E \phi_E + A_W \phi_W + S_u
 \tag{A.7}$$

$$\begin{aligned}
 \text{with } A_E &= D_e - \frac{1}{2} C_e \\
 A_W &= D_w + \frac{1}{2} C_w \\
 S_p &= \alpha_w C_w - \alpha_e C_e \\
 \text{and } S_u &= \beta_w C_w - \beta_e C_e .
 \end{aligned}$$

Table A.1 summarizes the appropriate formulae for general 2-D problems. It is worth noting that the separation of terms  $\alpha_i$  and  $\beta_i$  in Table A.1 ensures that  $S_p$  is always negative. This is a highly desirable result for convergence of the matrix inversion routine.

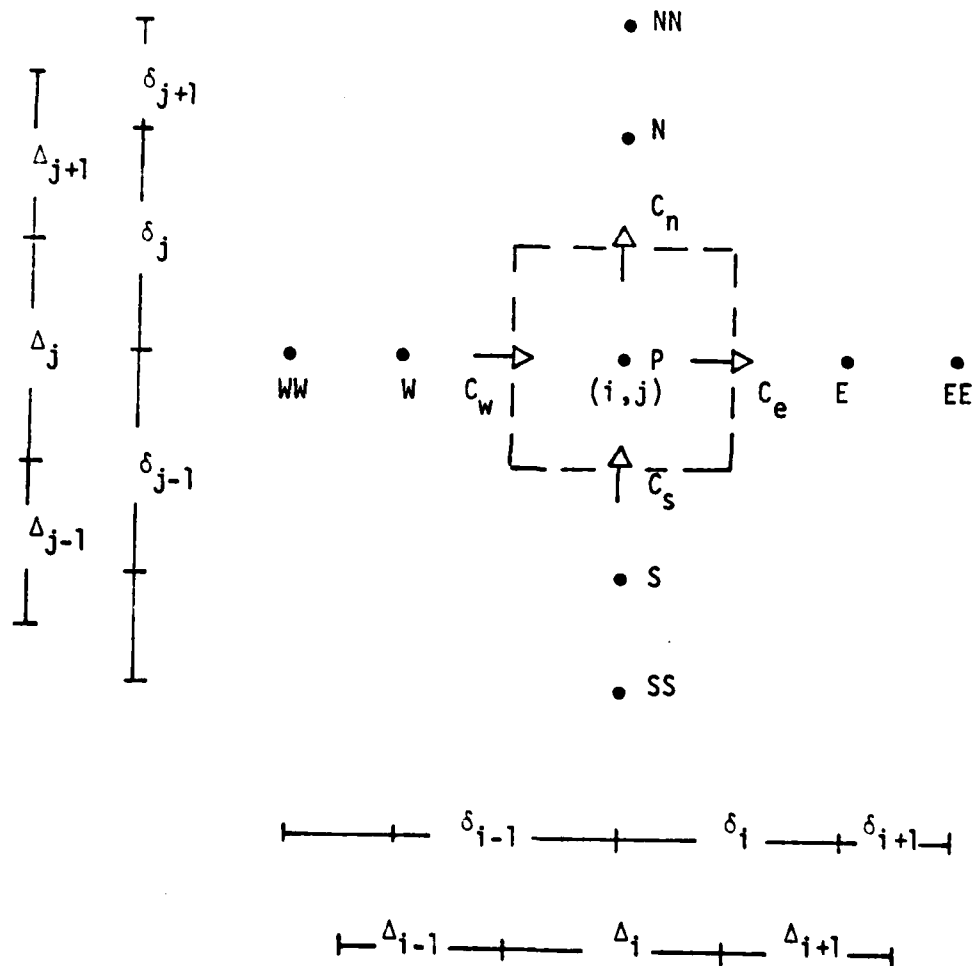


Figure A.1

$\psi_i$	$\alpha_i$	$\beta_i$	$C_i$
$\phi_e = \frac{1}{2}(\phi_E + \phi_P) + \alpha_e \phi_P + \beta_e$	$\frac{\delta_{i-1}}{8\Delta_i} (1 + \frac{\delta_i}{\delta_{i-1}})$	$-\frac{(\delta_i)^2}{8\Delta_i} (\frac{\phi_E}{\delta_i} + \frac{\phi_W}{\delta_{i-1}})$	$C_e > 0$
	$-\frac{\delta_i}{8\Delta_{i+1}}$	$-\frac{(\delta_i)^2}{8\Delta_{i+1}} (\frac{\phi_{EE} - \phi_E}{\delta_{i+1}} - \frac{\phi_E}{\delta_i})$	$C_e < 0$
$\phi_W = \frac{1}{2}(\phi_P + \phi_W) + \alpha_W \phi_P + \beta_W$	$-\frac{\delta_{i-1}}{8\Delta_{i-1}}$	$\frac{(\delta_{i-1})^2}{8\Delta_{i-1}} (\frac{\phi_W}{\delta_{i-1}} + \frac{\phi_W - \phi_{WW}}{\delta_{i-2}})$	$C_W > 0$
	$\frac{\delta_{i-1}}{8\Delta_i} (1 + \frac{\delta_{i-1}}{\delta_i})$	$-\frac{(\delta_{i-1})^2}{8\Delta_i} (\frac{\phi_E}{\delta_i} + \frac{\phi_W}{\delta_{i-1}})$	$C_W < 0$
$\phi_n = \frac{1}{2}(\phi_N + \phi_P) + \alpha_n \phi_P + \beta_n$	$\frac{\delta_j}{8\Delta_j} (1 + \frac{\delta_j}{\delta_{j-1}})$	$-\frac{(\delta_j)^2}{8\Delta_j} (\frac{\phi_N}{\delta_j} + \frac{\phi_S}{\delta_{j-1}})$	$C_n > 0$
	$-\frac{\delta_j}{8\Delta_{j+1}}$	$-\frac{(\delta_j)^2}{8\Delta_{j+1}} (\frac{\phi_{NN} - \phi_N}{\delta_{j+1}} - \frac{\phi_N}{\delta_j})$	$C_n < 0$
$\phi_S = \frac{1}{2}(\phi_P + \phi_S) + \alpha_S \phi_P + \beta_S$	$-\frac{\delta_{j-1}}{8\Delta_{j-1}}$	$\frac{(\delta_{j-1})^2}{8\Delta_{j-1}} (\frac{\phi_S}{\delta_{j-1}} + \frac{\phi_S - \phi_{SS}}{\delta_{j-2}})$	$C_S > 0$
	$\frac{\delta_{j-1}}{8\Delta_j} (1 + \frac{\delta_{j-1}}{\delta_j})$	$-\frac{(\delta_{j-1})^2}{8\Delta_j} (\frac{\phi_N}{\delta_j} + \frac{\phi_S}{\delta_{j-1}})$	$C_S < 0$

$$\phi_P \{A_E + A_W + A_N + A_S - S_P\} = \phi_E A_E + \phi_W A_W + \phi_N A_N + \phi_S A_S + S_U$$

$$S_P = C_W^\lambda W - C_e^\alpha e + C_S^\alpha s - C_n^\alpha n$$

$$S_U = C_W^\beta W - C_e^\beta e + C_S^\beta s - C_n^\beta n$$

TABLE A.1

## APPENDIX II

### FULL SCALE PLOTS OF TURBULENT FLOW DATA

Due to reproduction and mailing costs, some copies of this report are lacking the extensive data set pertaining to Appendix II. If full-scale plots are not included here, they will be made available upon request. See title page for mailing address of the Principal Investigator.

APPENDIX III

PLOTS OF LAMINAR FLOW CALCULATIONS

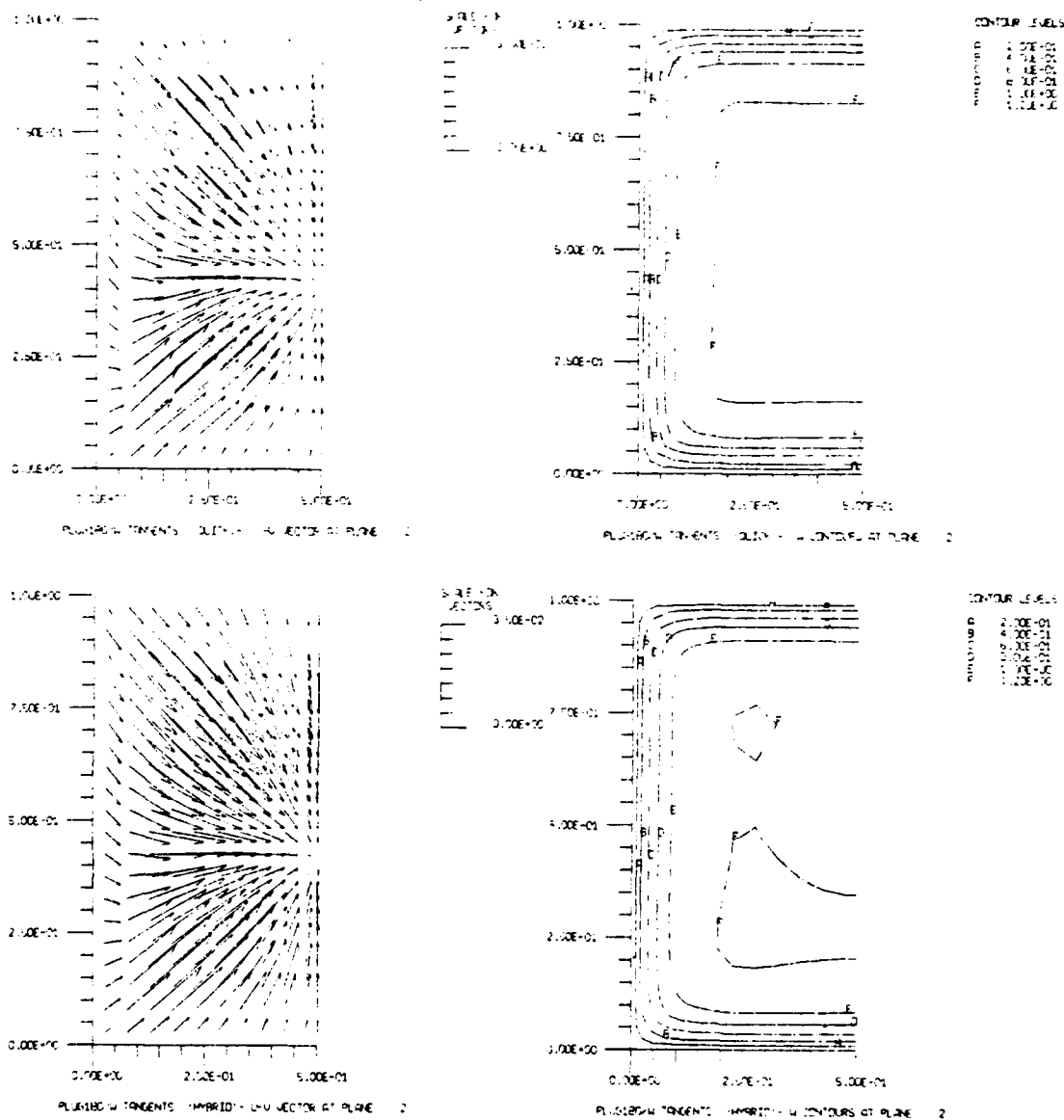
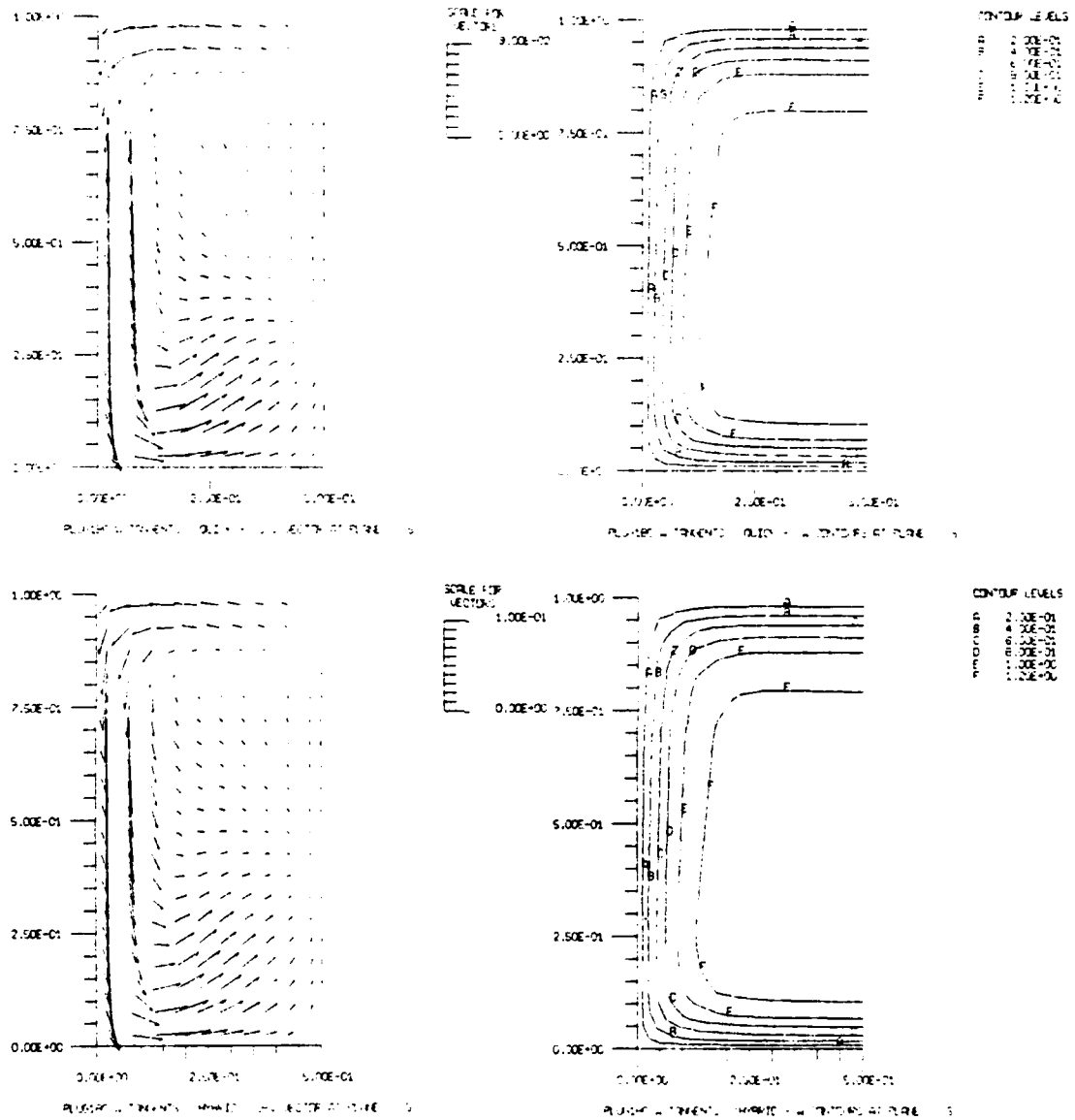


Figure 1: Calculated cross-stream and streamwise velocity components at  $X_H = -1$  in laminar regime. Plug flow inlet profile. Components normalized by  $U_B = 0.02$  m/s. Outer radius at top of each plot.



101 0210-2785

Figure 2: Calculated cross-stream and streamwise velocity components at  $\theta = 3^\circ$  in laminar regime. Plug flow inlet profile. Components normalized by  $U_B = 0.02$  m/s. Outer radius at top of each plot.



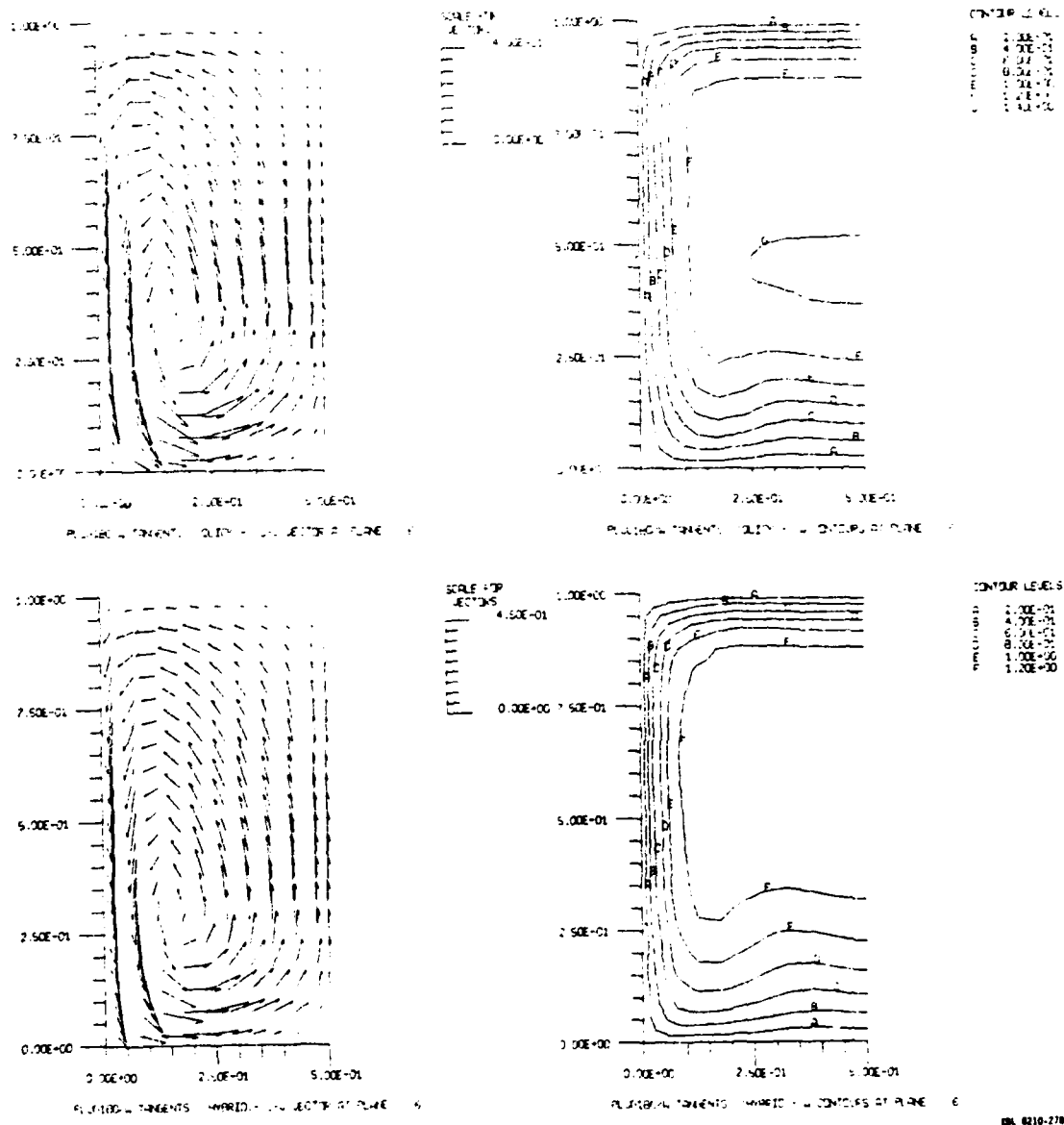
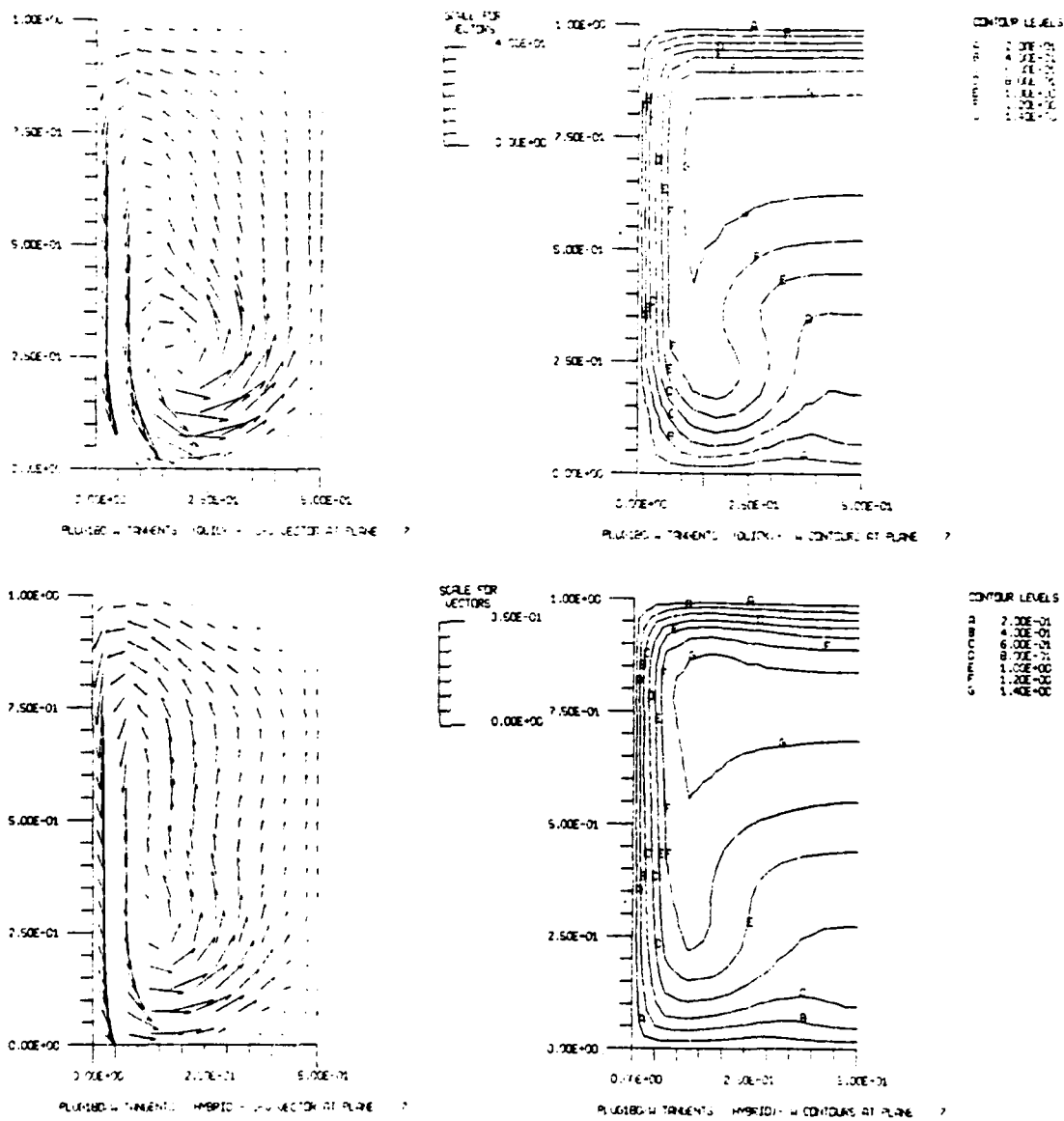


Figure 3: Calculated cross-stream and streamwise velocity components at  $\theta = 45^\circ$  in laminar regime. Plug flow inlet profile. Components normalized by  $U_B = 0.02$  m/s. Outer radius at top of each plot.



NSA 8810-2783

Figure 4: Calculated cross-stream and streamwise velocity components at  $\theta = 90^\circ$  in laminar regime. Plug flow inlet profile. Components normalized by  $U_B = 0.02$  m/s. Outer radius at top of each plot.

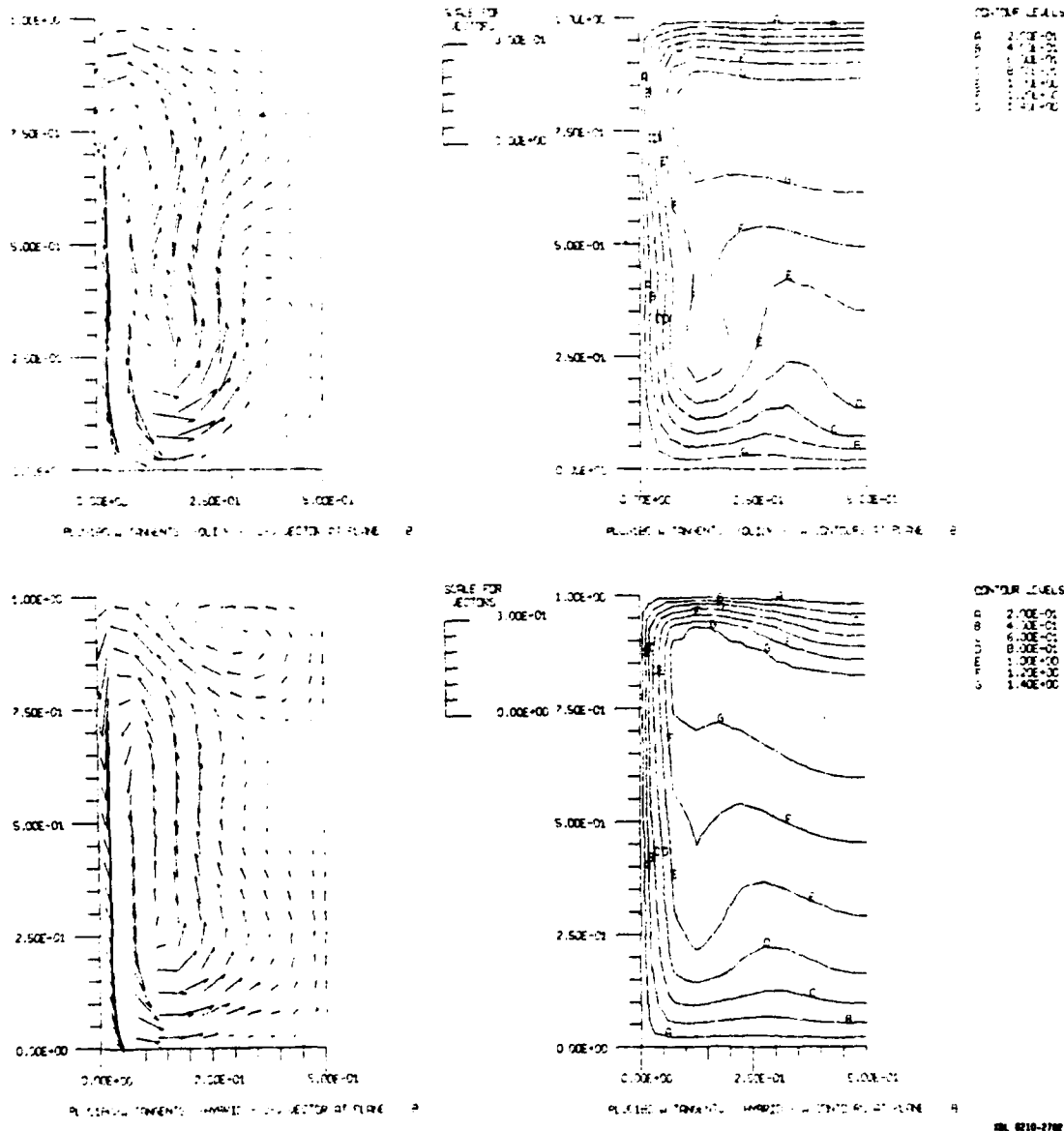


Figure 5: Calculated cross-stream and streamwise velocity components at  $\theta = 130^\circ$  in laminar regime. Plug flow inlet profile. Components normalized by  $U_B = 0.02$  m/s. Outer radius at top of each plot.

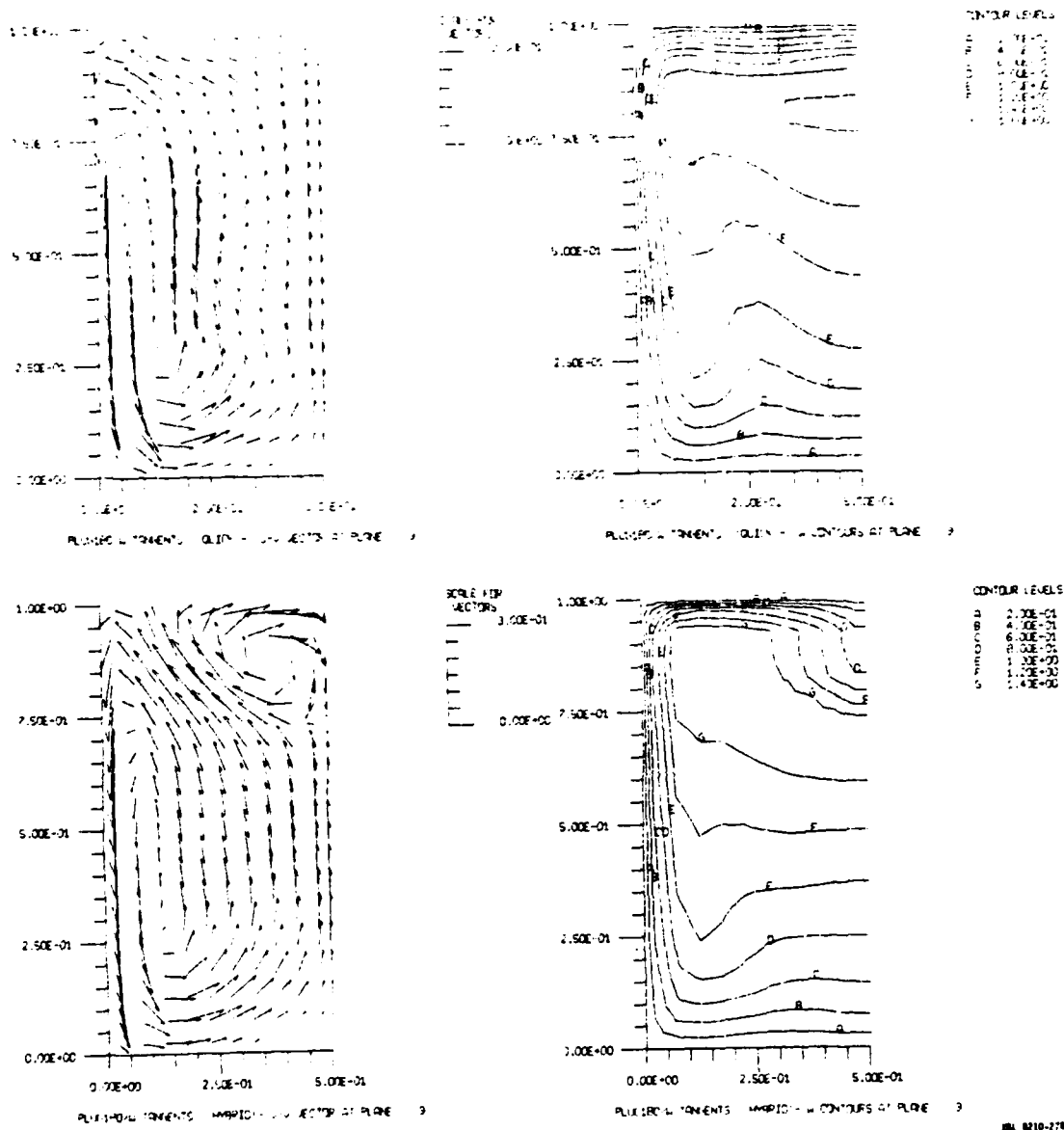


Figure 6: Calculated cross-stream and streamwise velocity components at  $\theta = 177^\circ$  in laminar regime. Plug flow inlet profile. Components normalized by  $U_0 = 0.02$  m/s. Outer radius at top of each plot.

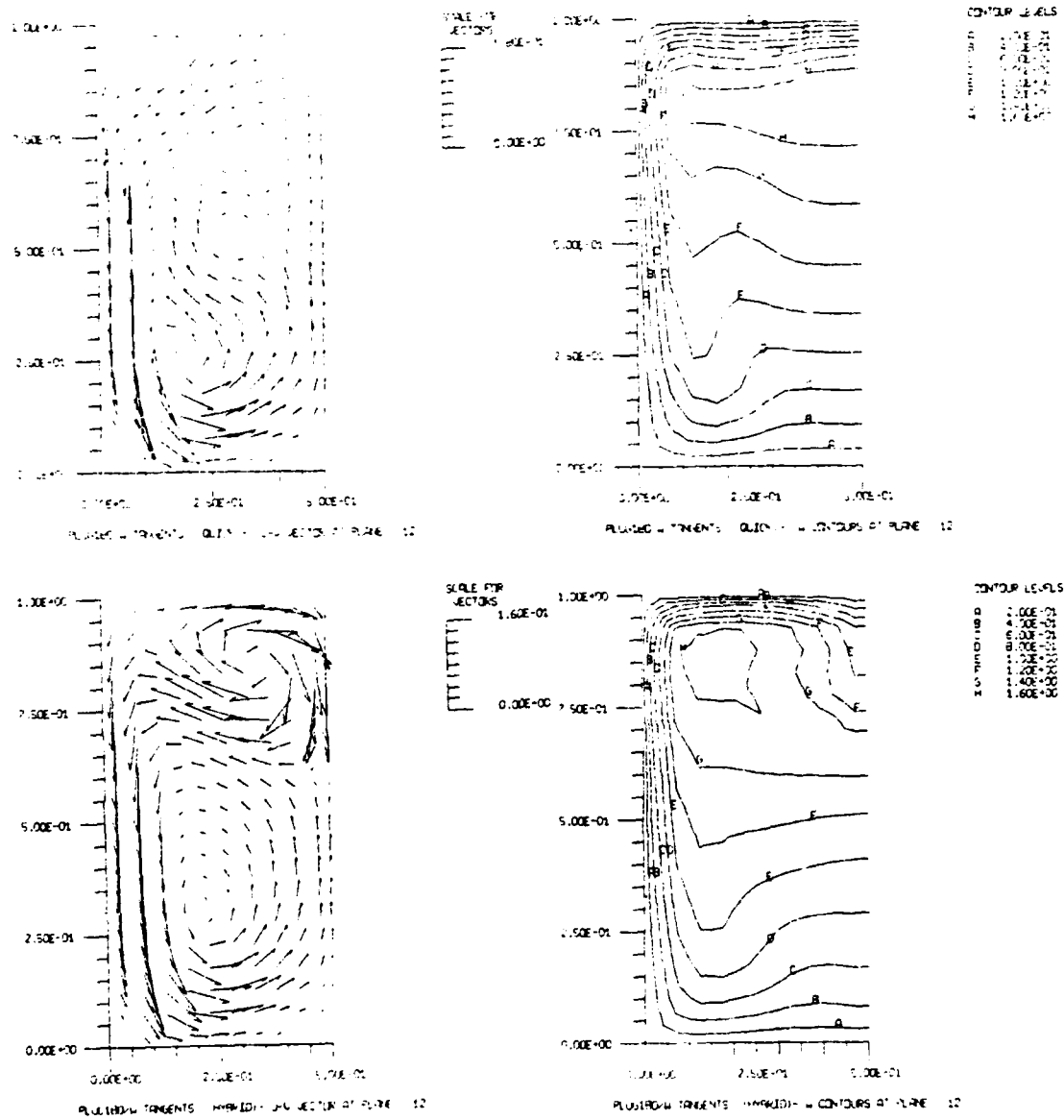


Figure 7: Calculated cross-stream and streamwise velocity components at  $X_H = 1$  in laminar regime. Plug flow inlet profile. Components normalized by  $U_B = 0.02$  m/s. Outer radius at top of each plot.

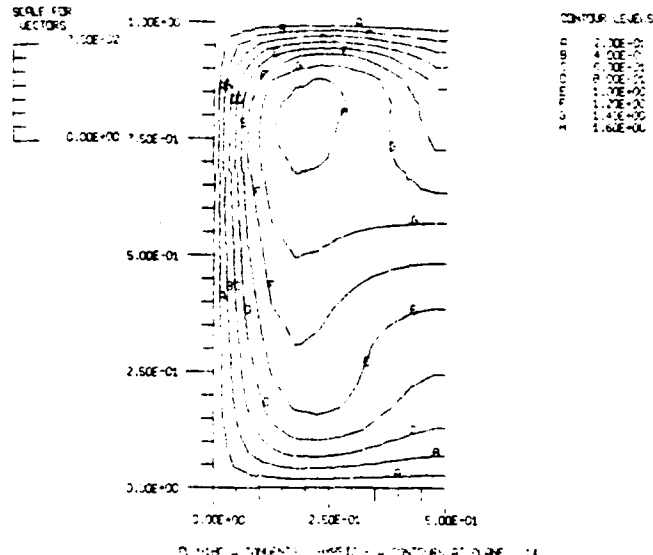
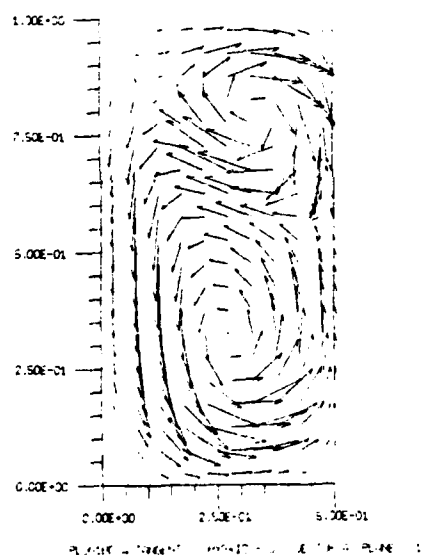
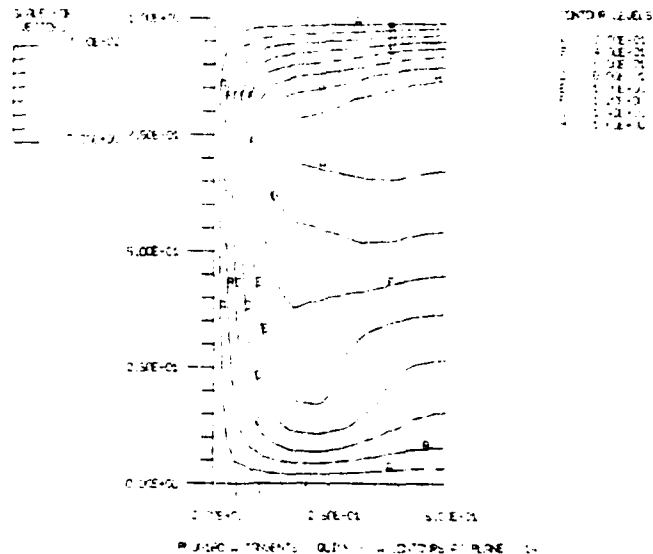
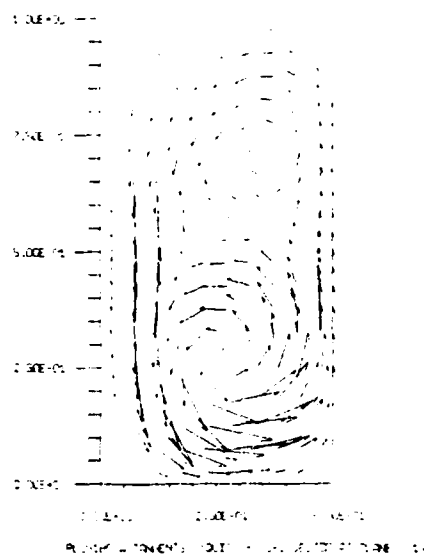


Figure 8: Calculated cross-stream and streamwise velocity components at  $X_H = 5$  in laminar regime. Plug flow inlet profile. Components normalized by  $U_B = 0.02$  m/s. Outer radius at top of each plot.

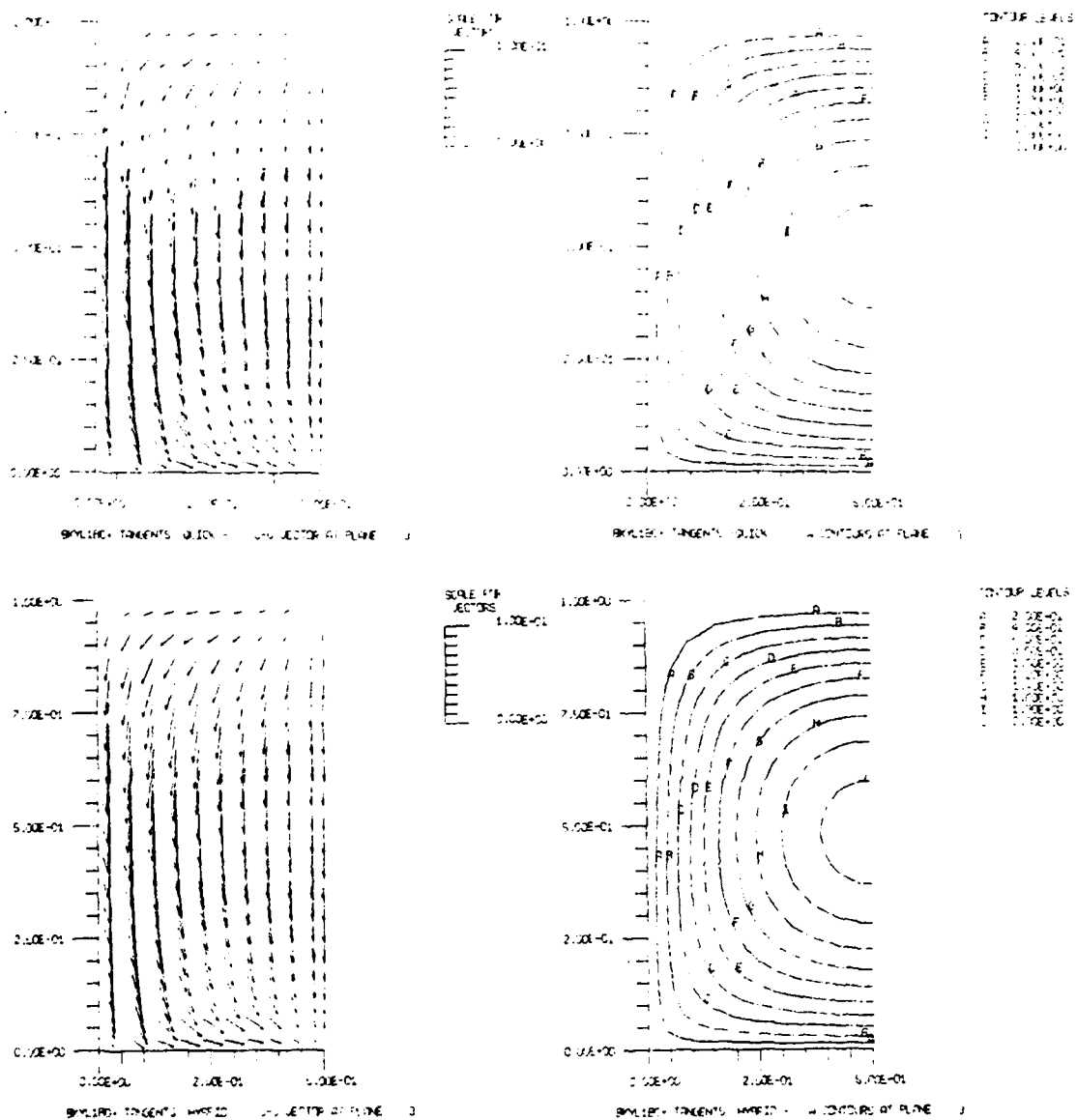
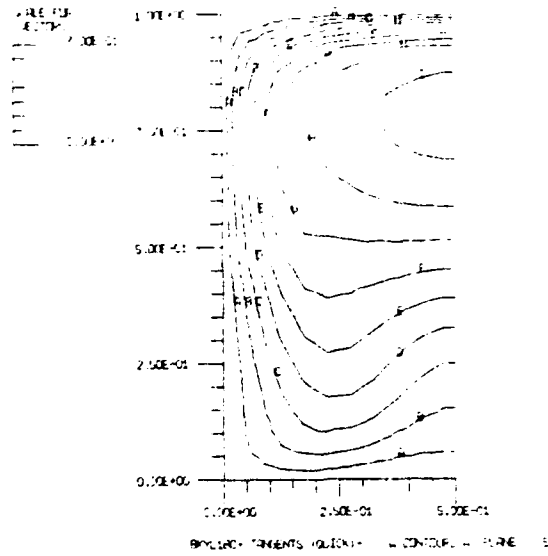
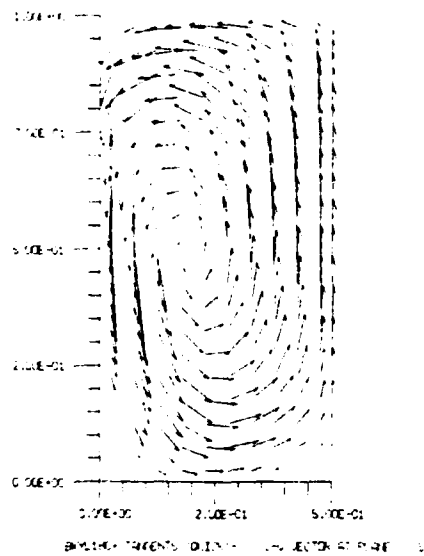
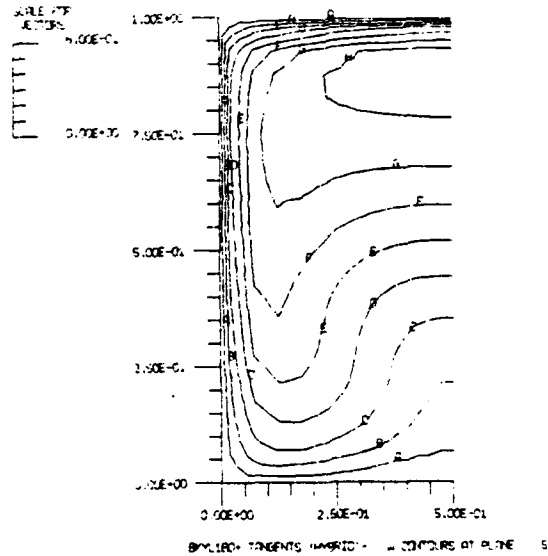
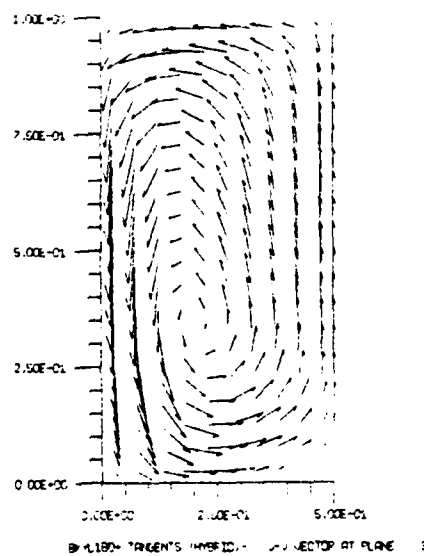


Figure 9: Calculated cross-stream and streamwise velocity components at  $\theta = 3^\circ$  in laminar regime. Parabolic flow inlet profile. Components normalized by  $U_B = 0.02$  m/s. Outer radius at top of each plot.



CONT. LEVEL
1.00E+01
0.50E+01
0.00E+00
-0.50E+01
-1.00E+01



CONT. LEVEL
1.00E+01
0.50E+01
0.00E+00
-0.50E+01
-1.00E+01

181 8210-2794

Figure 10: Calculated cross-stream and streamwise velocity components at  $\theta = 45^\circ$  in laminar regime. Parabolic flow inlet profile. Components normalized by  $U_B = 0.02$  m/s. Outer radius at top of each plot.



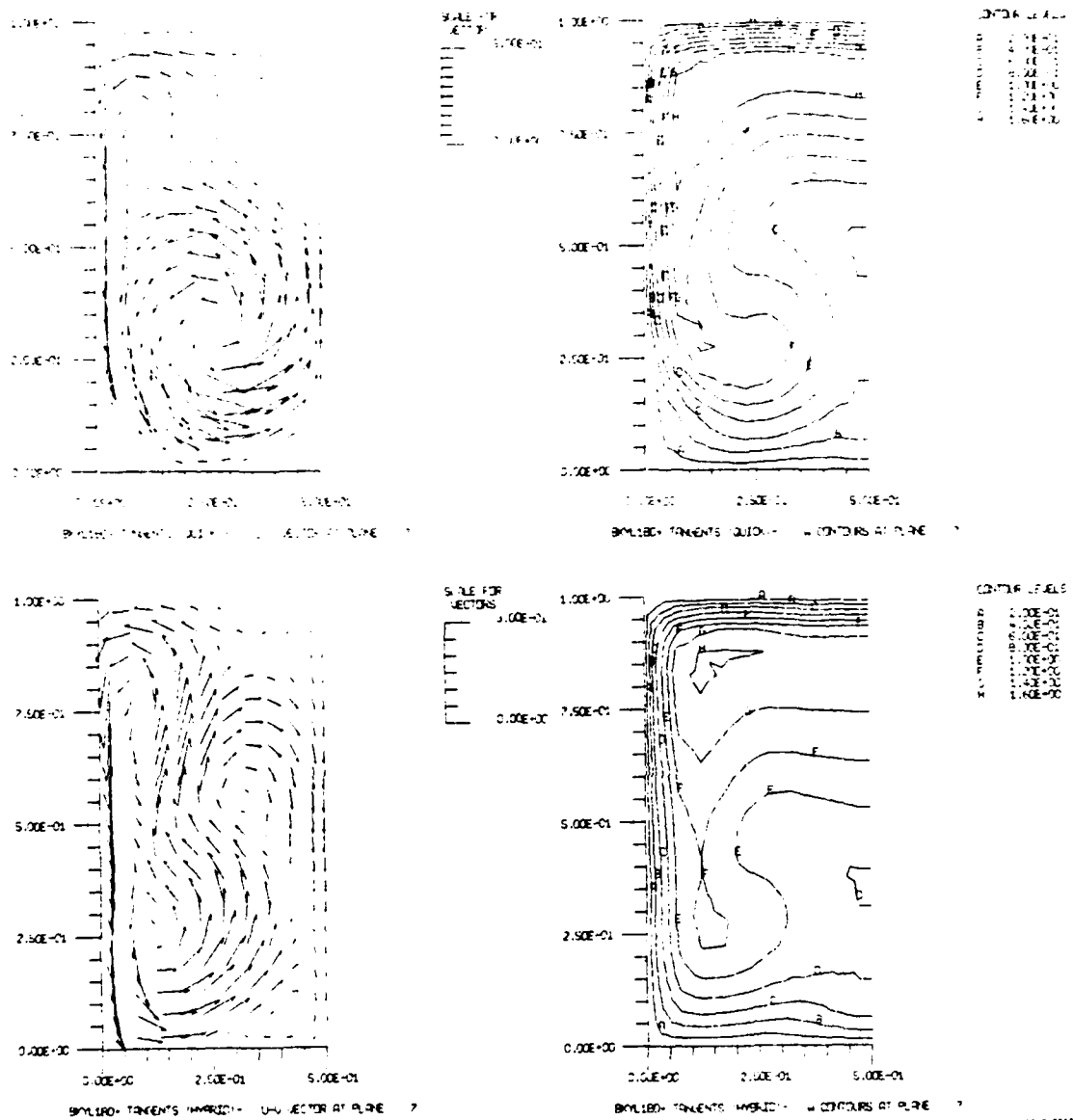


Figure 11: Calculated cross-stream and streamwise velocity components at  $\theta = 90^\circ$  in laminar regime. Parabolic flow inlet profile. Components normalized by  $U_B = 0.02$  m/s. Outer radius at top of each plot.

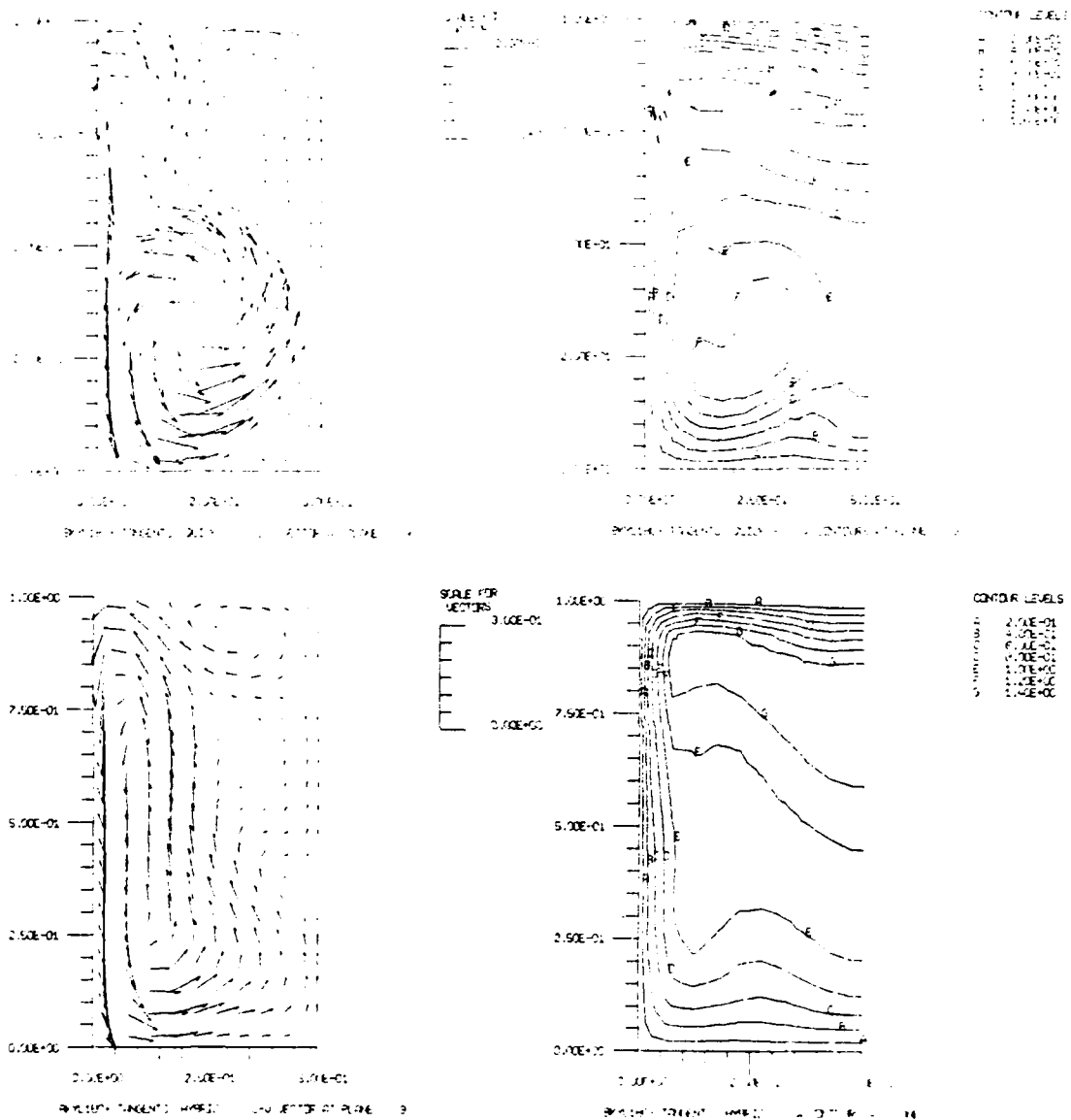


Figure 12: Calculated cross-stream and streamwise velocity components for  $\theta = 130^\circ$  in laminar regime. Parameters:  $Re = 100$ ,  $Pr = 1.0$ . Components normalized by  $U_\infty$  and  $V_\infty$  respectively of each plot.

AD-A120 613

DEVELOPING TURBULENT FLOW IN A 180 DEGREE BEND AND  
DOWNSTREAM TANGENT OF. (U) CALIFORNIA UNIV BERKELEY  
LAWRENCE BERKELEY LAB J A HUMPHREY ET AL. SEP 82  
LBL-14844NN00014-80-C-0031

2/2

UNCLASSIFIED

F/G 20/4

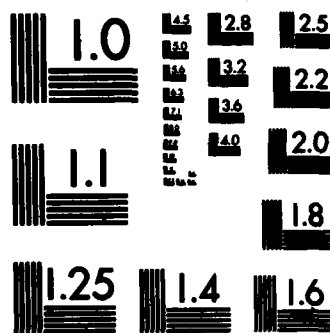
NL



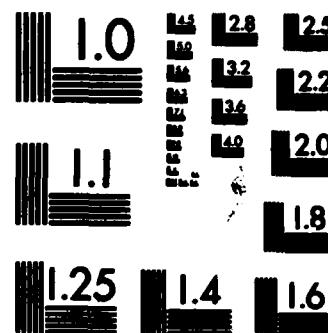
END

FILED

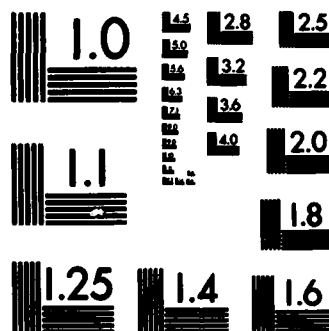
DTIC



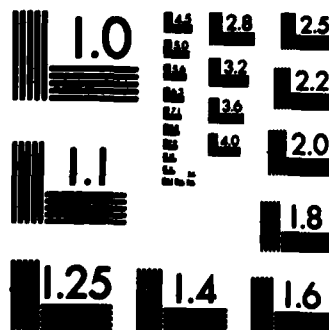
MICROCOPY RESOLUTION TEST CHART  
NATIONAL BUREAU OF STANDARDS-1963-A



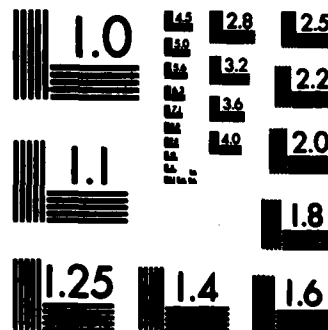
MICROCOPY RESOLUTION TEST CHART  
NATIONAL BUREAU OF STANDARDS-1963-A



MICROCOPY RESOLUTION TEST CHART  
NATIONAL BUREAU OF STANDARDS-1963-A



MICROCOPY RESOLUTION TEST CHART  
NATIONAL BUREAU OF STANDARDS-1963-A



MICROCOPY RESOLUTION TEST CHART  
NATIONAL BUREAU OF STANDARDS-1963-A

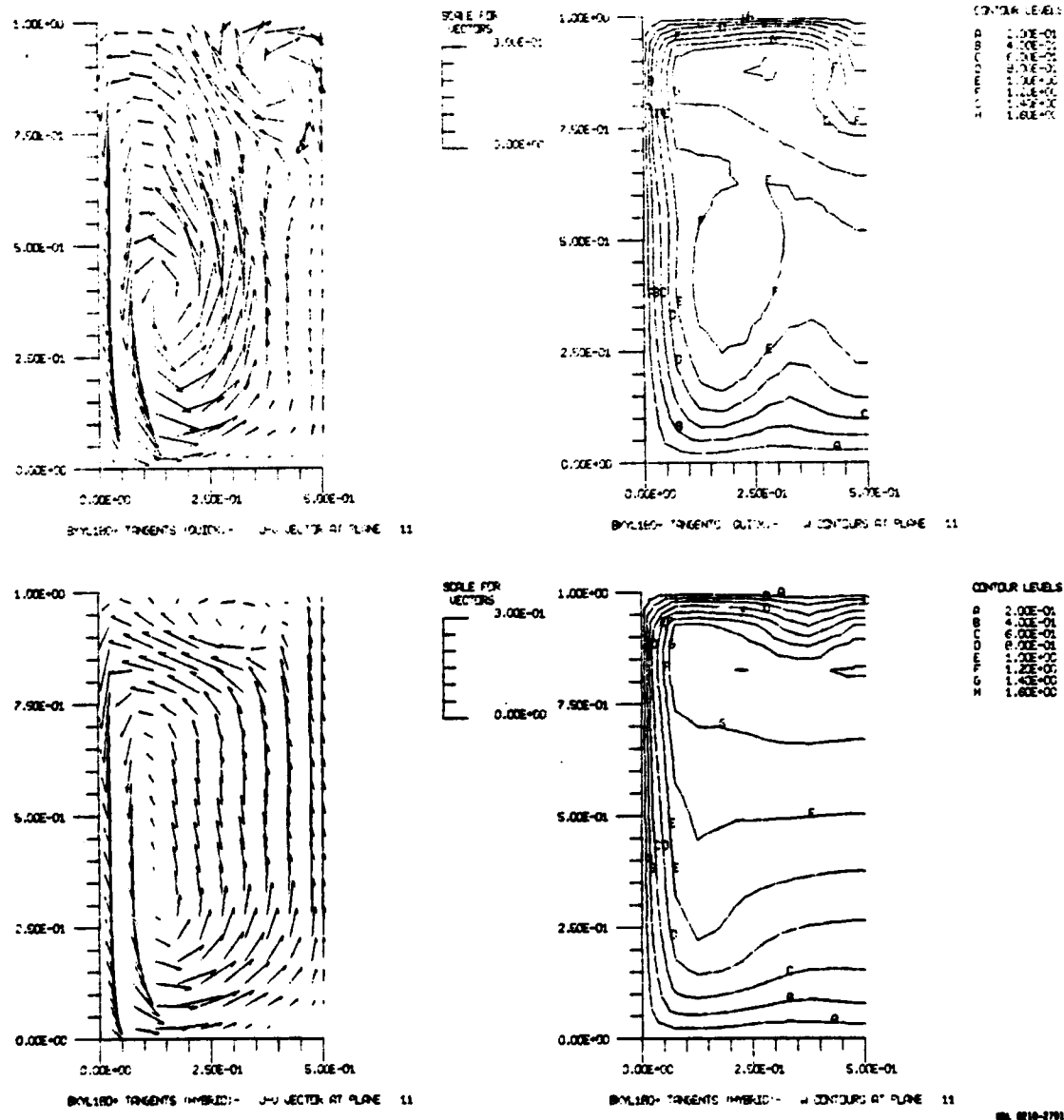


Figure 13: Calculated cross-stream and streamwise velocity components at  $\theta = 177^\circ$  in laminar regime. Parabolic flow inlet profile. Components normalized by  $U_B = 0.02$  m/s. Outer radius at top of each plot.

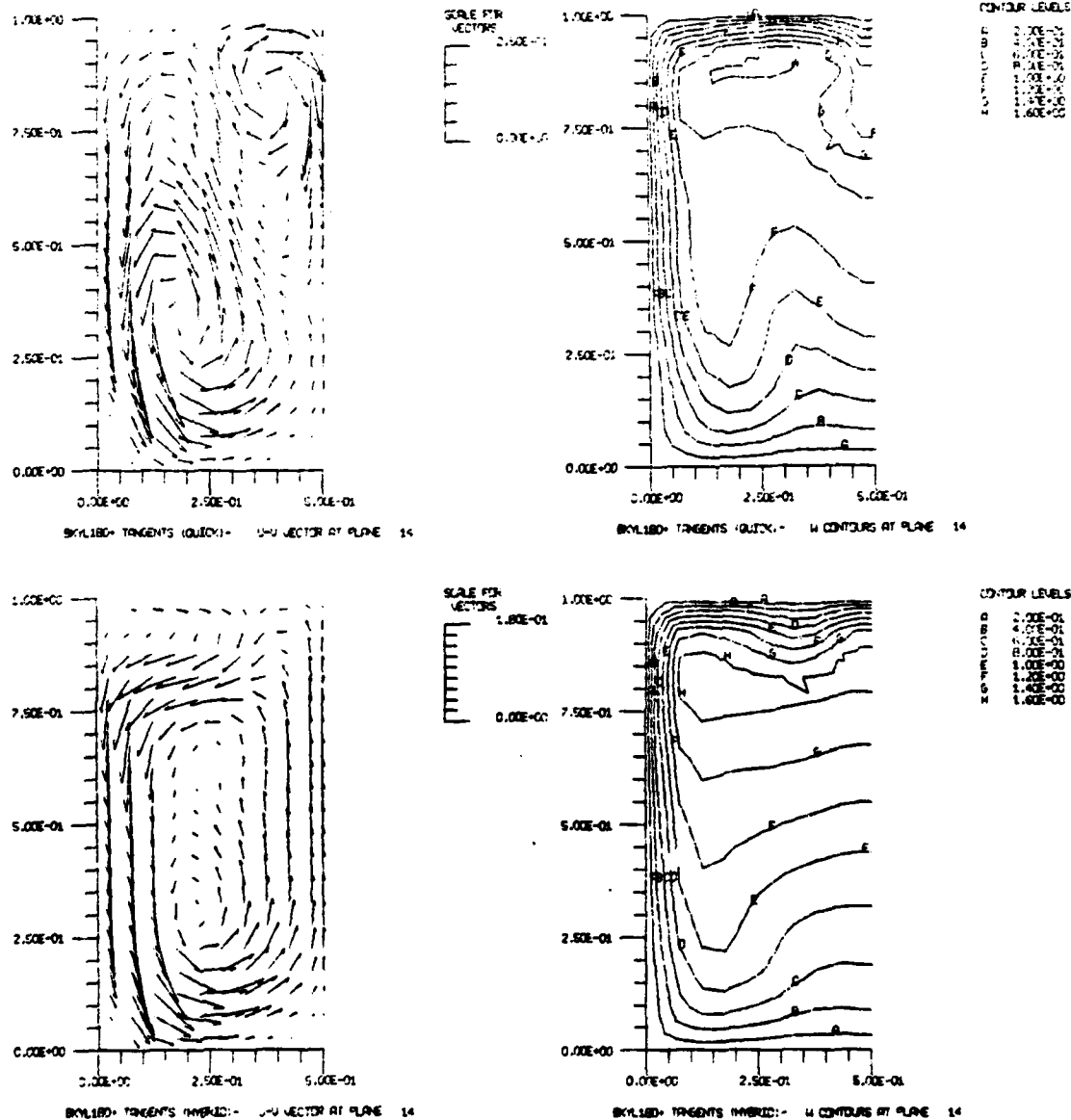


Figure 14: Calculated cross-stream and streamwise velocity components at  $X_H = 1$  in laminar regime. Parabolic flow inlet profile. Components normalized by  $U_B = 0.02$  m/s. Outer radius at top of each plot.



**Figure 15:** Calculated cross-stream and streamwise velocity components at  $X_H = 5$  in laminar regime. Parabolic flow inlet profile. Components normalized by  $U_B = 0.02$  m/s. Outer radius at top of each plot.

**END**

**FILMED**

10 00